Isomer and β-delayed gamma-ray spectroscopy for structure studies of heavy, neutron-rich nuclei

Nawras M. S. Al-Dahan

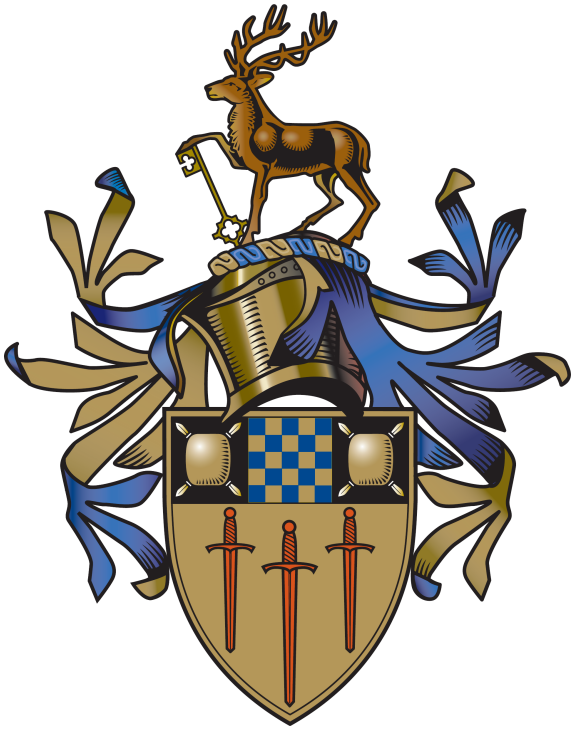

Submitted for the degree of Doctor of Philosophy

Department of Physics,
Faculty of Engineerings and Physical Sciences,
University of Surrey.

June 2010

Abstract

β decays from heavy, neutron-rich nuclei with $A \sim 190$ have been investigated following their production via the relativistic projectile fragmentation of an E/A = 1 GeV ^{208}Pb primary beam on a $\sim$2.5 g/cm^2 ^{9}Be target. The reaction products were separated and identified using the GSI FRagment Separator (FRS) and stopped in the RISING active stopper. The active stopper consisted of an array of 5 cm $\times$ 5 cm Double Sided Silicon Strip Detectors (DSSSDs), each pixellated into 16 strips in both horizontal and vertical directions to measure the position of the implanted ions and correlate these with subsequent β decays detected in the same pixels. γ decays were observed and correlated with these secondary ions on an event-by-event basis such that γ ray transitions following from both internal (isomeric) and β radioactivity decays were recorded. The particle identification procedure was confirmed by the observation of the previously reported isomers in ^{188}Ta, ^{190}W, ^{192}Re and ^{193}Re. The current data also show evidence for previously unreported isomeric states in ^{187}Hf, ^{189,190}Ta and ^{191}W. A number of discrete, β-delayed γ-ray transitions associated with β decays from ^{194}Re to excited states in ^{194}Os have been observed, including previously reported decays from the yrast $I^{\pi} = (6^+)$ state. Three previously unreported γ-ray transitions with energies 194, 349 and 554 keV are also identified; these transitions are associated with decays from higher spin states in ^{194}Os in the present work. A β-decay half-life for ^{194}Re has been determined for the first time in this work by measuring the time differences between the implanted secondary ions in the active stopper and their subsequent correlated β particles in the same pixel. The results of these investigations are compared with theoretical predictions from Nilsson Multi Quasi Particle (MQP) calculations and potential energy surface calculations. The structure of the neutron-rich $N = 128$ isotones ^{208}Hg and ^{209}Tl has also been investigated following their production via relativistic projectile fragmentation of a E/A=1 GeV ^{238}U beam. Decays from

metastable states in these nuclei have been identified and the yrast structures up to spin-parity 8^+ and $17/2^+$ respectively have been observed. The results are compared with restricted basis shell model calculations, which allow the first detailed verification of the shell-model approach in the region determined by magic numbers $Z < 82$ and $N > 126$.

"Contentment is wealth that does not diminish"

Imam Ali (a.s.)

Acknowledgments

All praise belongs to God, Lord of the Universe. First of all I would like to thank our God. Huge thanks to our God without his support and help I will have done nothing.

Very big thanks to my Mother, my Father and for all my family especially my Wife and for my Friends as well, without their support and help I am nothing.

Special thanks for my supervisors, Prof. Paddy Regan and Dr. Zsolt Podolyák both are really fantastic supervisors, they are always working as team, help and support each other, for me its fantastic opportunity to work with such team. I will never forget what they have done for me for the rest of my life. From my first meeting with Paddy, he has been a vital source of advice, knowledge, support and guidance in every aspect of this undertaking. I am very thankful to Zsolt, he has provided me with incredible attention, experiences, physics explanations and support. Both of them are wonderful. In addition to this both of them have provided me with opportunities to travel so often, attend conferences, schools, participate in many experiments and meet so many new people and I will never forget their help in finding additional financial support.

Thanks a lot to all the people in the Higher Ministry and Scientific Research for their support and help. Also thanks to the University of Kerbala - College of Science - Department of Physics, especially I would like to thanks Dr. Amir Mohammed-Ali, Dr. Adie D. Salman, Dr. Fadhil Al-Taie, Dr. Mohammed Al-kaabi and Firas Al-Asfoor. I own a huge debt to Dr. Khalid Al-Attiah (University of Babylon) for his help and support. I would like to acknowledge the help and advice given by Dr. Ahmed Abdullettif (University of Babylon) and Dr. Adnan Al-Aaraji (University of Babylon).

I am grateful from Prof. W. Gelletly for his advice and for answering my questions. A special thanks for Prof. P. Walker for the nice discussions of my data. Thanks also for Prof. R. Casten (from University of Yale, USA) for fantastic discussions about ^{194}Os data. Thanks to Prof. G. Dracoulis (from Australian National University, Australia) for his discussions and for the MQP calculations for Re.

I would like to thank all my graduate colleagues and post-doctoral fellows in the Department of Physics. They have provided me an enjoyable working atmosphere and helped me to solve hard problems. Especially, I would like to thank Dr. Nasser

Alkomashi, Dr. Gregory Farrelly, Dr. Steve Steer, Dr. Jeff Thomas, Dr. Ajay Deo, Ian Cullen and Ana Denis Bacelar (from University of Brighton). These people spent a lot of time explaining a lot things for me, details of our experiments, and solving most of the problems I had in my laptop. Without their support and help my task for the PhD would have been much harder. Thanks also for Dr. Ed Simpson, Dr. Pete Mason, Huda Al-Sulaiti, Adam Garnsworthy, Nicky Patterson, Gemma Wilson and Simon Brown for their help.

Thanks a lot for all the people at GSI especially Stephane Pietri, Magda Górska, Hubert Grave, Hugo Maier and Jürgen Gerl for their help, discussions and support.

Thanks a lot to Prof. Adel Sharif who helped me a lot when I came to UK for the first time. I very much appreciated his advice and discussions. Also thanks to the Iraqi students at the University of Surrey, Baker Joda and Ali Merdaw, they helped me a lot. Thanks also to Sami Al-Aibi and to all the Iraqi students who study in UK.

Finally, I would like to thank David Munro who fixed the Linux problems that I had in my laptop and for installing all the software that I needed to do my analysis.

Contents

List of Figures

List of Tables

Chapter 1

Introduction

An atom consists of an extremely small, positively charged nucleus surrounded by a cloud of negatively charged electrons. The diameter of the atom is around 1 Angstrom (10^{-10}m) but the nucleus, which contains almost all of the mass of the atom, is of the order of Fermi (10^{-15}m). Nuclei consist of positively charged protons and electrically neutral neutrons which move independently of each other and interact via the strong and Coulomb forces. It is the aim of nuclear physics to understand how protons and neutrons interact together and how they affect the creation of the elements in the universe.

The production and study of the most neutron-rich isotopes is one of the frontiers of current nuclear structure research [1, 2]. There are just under 300 stable nuclei that do not undergo radioactive decay from their ground states, but a total of approximately 7000 different unstable nuclei are thought to be particle bound. To date, almost 3000 of these have been created and studied in the laboratory [3]. The investigation of heavy ($A >$170) neutron-rich nuclei poses an experimentally challenging area to study due to difficulties in populating such neutron-rich nuclei.

The projectile fragmentation technique provides opportunities to observe nuclei far from stability [4]. Fragmentation has proved to be an efficient tool for producing exotic nuclear species and when combined with high sensitivity γ-ray detection arrays, structural information can be gained for otherwise inaccessible nuclei [5, 6, 7, 8]. The highest sensitivity is achieved with both isomeric and β-delayed γ-ray spectroscopy techniques. Information on the excited states populated in this way can be obtained when producing only a few hundred nuclei of interest [9, 10]. In its simplest form the

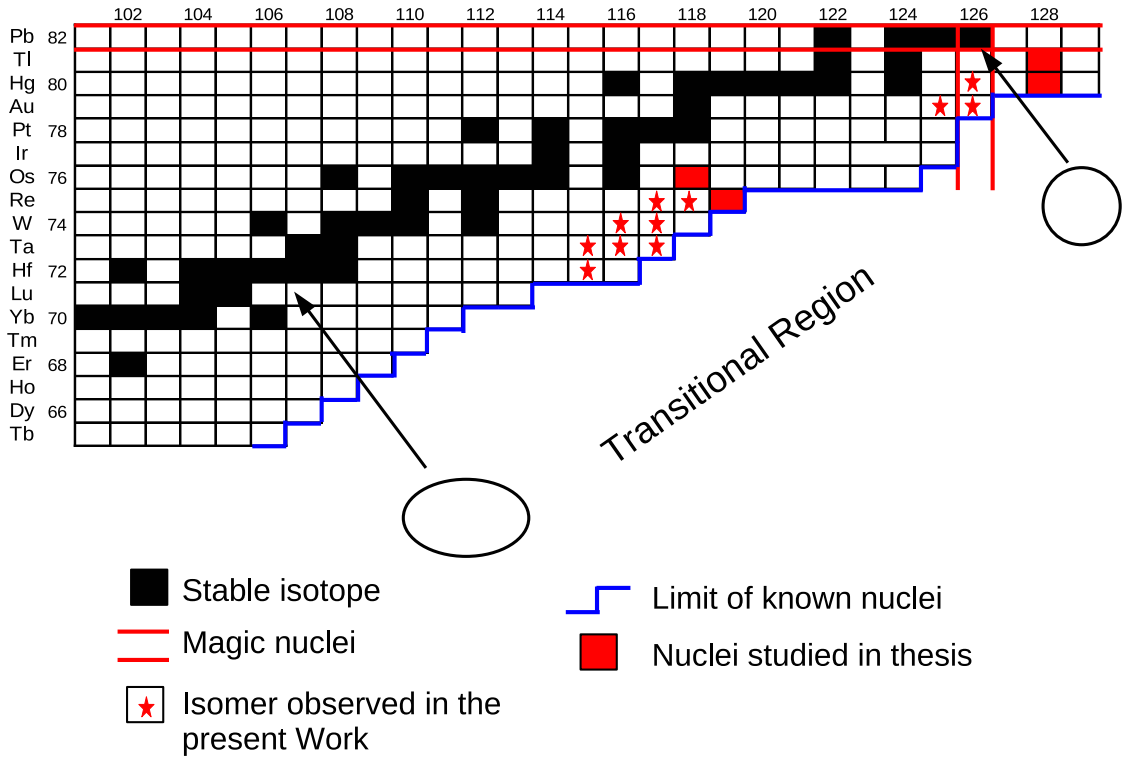

Figure 1.1: Schematic section of the nuclear chart displaying the region of interest in the current study. The red lines show the nuclei which have magic numbers of protons ($Z = 82$) or neutrons ($N = 126$). The black squares represent the stable nuclei. The red stars represent nuclei in which isomers were observed in the current work. The red nuclei were populated and studied in the current work using the Fragment Separator at GSI, Germany.

technique is sensitive to isomeric decays with lifetimes between 100 ns and 1 ms. The lower limit comes from the flight time through the fragment separator (approximately 300 ns), the upper limit is determined by the necessity of correlating the delayed γ-rays with the implanted ion.

It is well established that many nuclei with Z and N values between the closed shells are permanently deformed in their ground states. The deformation arises due to the way valence nucleons arrange themselves in an unfilled shell. The shape of the nucleus tends to drive to a non-spherical shape, becoming greatest when the shell is about half filled. The tendency to deformation is reversed and sphericity is restored

when the shell closure is complete. The nuclei at closed shells resist becoming deformed in their ground states and permanently deformed (ground state) nuclei are found only when *both* neutron and proton shells are partially filled.

Neutron-rich nuclei with $A \sim 190$ show a wide variation of nuclear structural properties and are characterized by the presence of different ground-state shapes, for example prolate, oblate, triaxial / γ-soft and spherical. The lighter isotopes of nuclei in this region are prolate deformed in their ground states and by adding more and more neutrons the shape becomes oblate [11, 12]. At the $N = 126$ closed shell, the nuclei become spherical [13, 14]. Figure 1.1 shows a schematic of the nuclear chart for $A \sim 180 - 220$.

1.0.1 $A \sim 190$ Region

The single particle motion and the residual interactions of nuclei near closed shells (i.e. only a few valence nucleons) can be used to predict the low-lying excitation energies of these nuclei. The properties of the low-lying states arise from the motion of these few valence nucleons. Such an approach is limited and has proved unsuccessful for predicting structural properties for nuclei near the mid shells and / or with a significant numbers of valence nucleons [15].

The Os-Pt region is known to be structurally very complex [16, 17, 18] with evidence of oblate, γ-soft and triaxial deformations. As such, it offers a rather sensitive testing ground for nuclear models [19, 20]. The Os isotopes exhibit a transition between deformed and spherical nuclei with increasing neutron number [21, 22]. These characteristics suggest that the study of the neutron-rich Os isotopes help to understand the interplay between complex nuclear modes [21]. The nucleus ^{194}Os has two neutrons above the heaviest stable Osmium isotope, ^{192}Os. The study of the low-lying energy spectrum of ^{194}Os helps to illuminate the approach of phase / shape transition in this region [21, 22]. The spectroscopy information from the current study therefore helps to test the theoretical predictions on this nucleus and also to confirm the limited previous structural information of this nucleus.

It is necessary to describe the properties of such "transitional" nuclei not simply in terms of the motion of a few valence nucleons, but rather by the *collective properties*, in which many nucleons contribute cooperatively. The collective model [24] considers

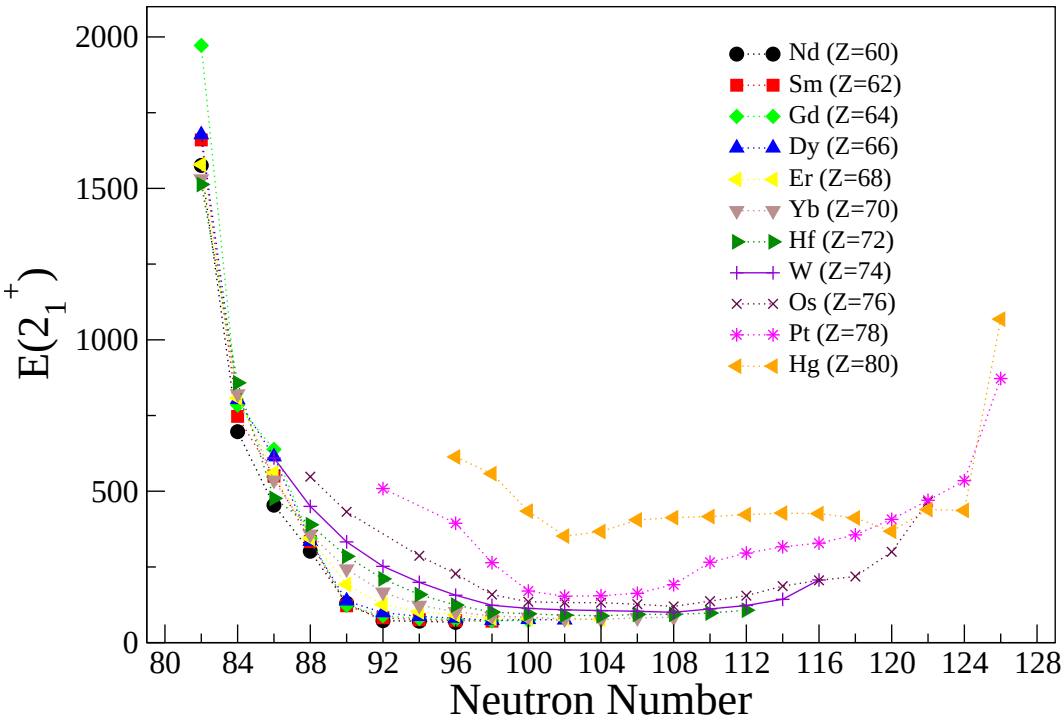

Figure 1.2: The experimental energy of the first excited state, $E(2^+)$, versus neutron number for even-even nuclei between Nd and Hg ($Z = 60 \rightarrow 80$) and for $N = 82 \rightarrow N = 126$. These data are taken from Ref. [23].

the nucleus as a single object, responsible for all the nuclear properties. The collective properties are found to vary smoothly with the valence product [25, 26].

Two key signatures of the low-lying excitations are used to investigate the collective characteristics of the nuclear structure for even-even nuclei [15, 25, 26]:
(i) The excitation energy of the first 2^+ state ($E(2^+)$) [27]: The $E(2^+)$ decreases smoothly as a function of the N and is remarkably constant for the even-even nuclei in the region from $N = 92$ to $N = 116$ and $Z = 60 \rightarrow 76$, as shown in figure 1.2, lower $E(2^+)$ generally indicates more collective nuclei; and
(ii) The ratio of the first excitation energies 4_1^+ and 2_1^+ ($R_{4/2} = E(4_1^+)/E(2_1^+)$): The $E(4_1^+)/E(2_1^+)$ ratio for even-even nuclei in the region from $N = 92$ to $N = 116$ and $Z = 60 \rightarrow 74$, as shown in figure 1.3. The ratio evolves form a value of < 2 for nuclei near the closed shells, to ~ 2 for vibrational structures [28], to ~ 3.33 for well-deformed axial rotors near the mid shell [29].

The first part of this thesis focusses on the structure study of the heavy neutron-

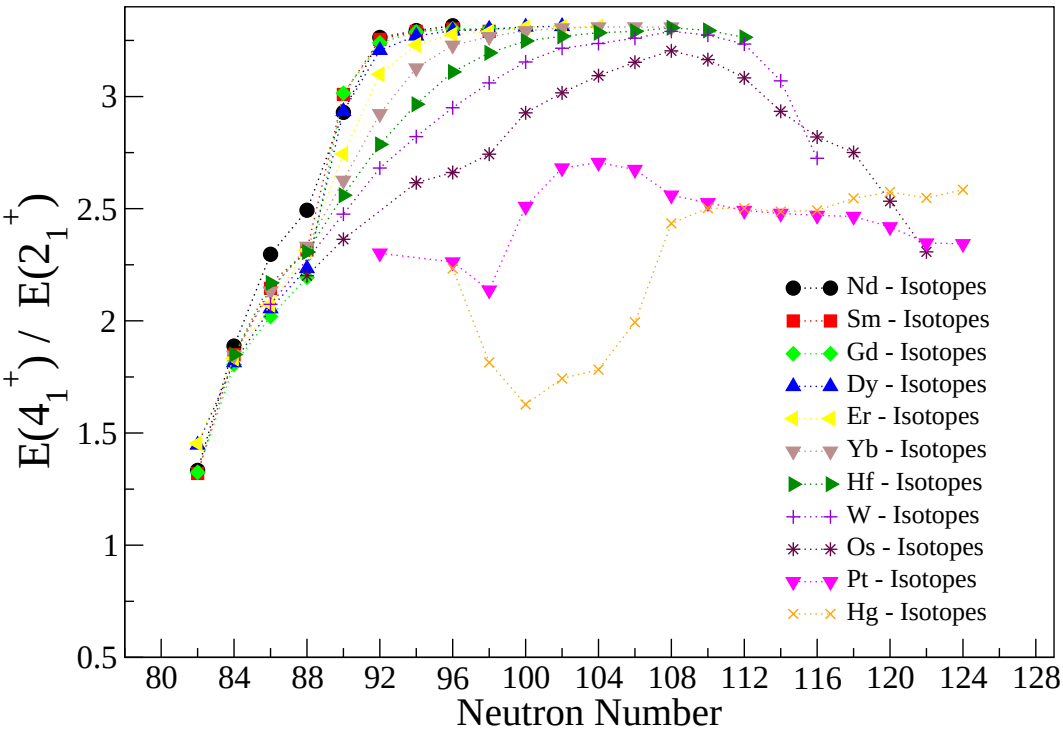

Figure 1.3: Experimental ratio of the excitation energies of the yrast $I^\pi = 4^+$ and $I^\pi = 2^+$ states ($E(4_1^+)/E(2_1^+)$) for even-even Nd-Hg ($Z = 60 \rightarrow 80$) nuclei between $N = 82$ and $N = 126$, data taken from Ref. [23].

rich Osmium isotopes, specifically $^{194}_{76}Os_{118}$.

1.0.2 $Z < 82$ $N > 126$ Studies

The understanding of how shell structure arises and develops is a major goal in nuclear physics. To this end, it is of particular importance to measure the structural properties of nuclei in the vicinity of closed shells. Information on the single-particle energies, proton-neutron interactions and two-body residual interactions can be derived from experimental observables such as binding energies, energies of the excited states and electromagnetic transition probabilities. The proton-neutron (p-n) interaction [30, 31], particularly among the valence nucleons, is an important factor in controlling the onset and development of collectivity and deformation in nuclei. It has a characteristic behaviour that can be understood in terms of the spatial overlaps of the valence nucleons, at least near closed shells. Since the residual p-n interaction is primarily short range and attractive, it should be strongest when the protons and

neutrons are in orbitals with greatest spatial overlap [32]. Valence p-n interactions can be extracted experimentally from double differences of binding energies. While many nuclei in the ^{208}Pb region have been studied, there have, until now, been no values for the p-n interaction for any even-even nucleus with $Z < 82$ and $N > 126$; nor are there any spectroscopic data for any even-even nuclei in this region. Yet, such nuclei, representing the "fourth" quadrant (the hole-particle sector) surrounding ^{208}Pb, are critical for understanding the effects of seniority, the onset of configuration mixing and collectivity, and the drivers of nuclear deformation.

The region around the doubly magic nucleus ^{208}Pb presents a unique testing ground of basic nuclear physics concepts. With the results on ^{208}Hg presented in the current work, this is the only region of the nuclear chart (above ^{48}Ca) where the information is available on excited states on all four neighboring even-even nuclei (see figure 1.4).

Recently, the mass of ^{208}Hg was measured [32]. This has been used to determine the p-n interaction strength of ^{210}Pb, the first value in the hole-particle, h-p quadrant. It also of note, that the r-process path passes through the quadrants where ^{208}Hg lies ($Z < 82$, $N > 126$) and the properties of these r-process path nuclei influence the abundances of heavy nuclei in nature. The half-lives of these nuclei, one of the main ingredients in the r-process calculations, are determined by the occupancy of these orbitals in the ground state configurations.

The second part of this thesis provides the first spectroscopic data on an even-even nucleus with $Z < 82$ and $N > 126$, namely $^{208}_{80}\mathrm{Hg}_{128}$. Knowledge of the properties of heavy neutron-rich nuclei at or near the $N = 126$ shell closure is very limited. In the case of nuclei with $N > 126$ and $Z < 82$ excited states have been reported to date only in ^{208}Tl [33] and ^{209}Tl [34, 35, 36, 37]. The lack of information on nuclei in this region is mainly due to the difficulties in creating and populating excited states in these neutron-rich nuclei. Decays from isomeric states in the $N = 128$ isotones, ^{208}Hg and ^{209}Tl have been identified for the first time in the current work.

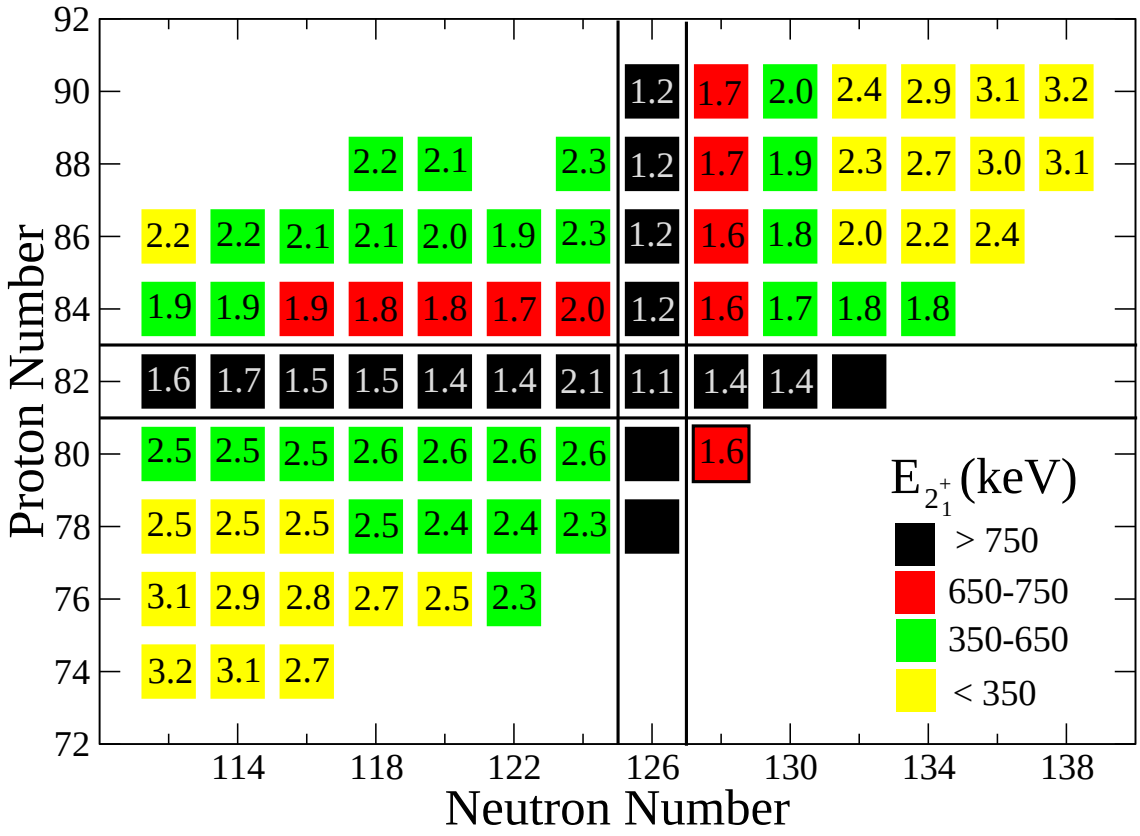

Figure 1.4: Experimental excitation energy range of $E(2_1^+)$ values and the $E(4_1^+)/E(2_1^+)$ energy ratios around $^{208}_{82}Pb_{126}$. Only even-even nuclei are considered. Four quadrants are defined by the $Z = 82$ proton and $N = 126$ neutron shell closures. The red box with black square is the first experimental results for ^{208}Hg from the current work. Other data are taken from Ref. [23].

1.1 Outline of thesis

In the two separate studies described in this thesis, projectile fragmentation reactions were used to populate the nuclei of interest which were identified using the Fragment Separator (FRS) [38] at the GSI laboratory in Darmstadt, Germany. The decays of these nuclei have been studied following both β and isomer-delayed γ-ray spectroscopy using the Rare ISotope INvestigations at GSI (RISING) γ-ray spectrometer [38]. The β-delayed studies utilized the new RISING Active Stopper [39] which enabled positional and temporal correlations to be determined between the implantation of a specific exotic isotope and its subsequent β decay.

The first specific area of research presented in this thesis is the production and

structural investigation of the most neutron-rich isotopes of the elements Rhenium (Re, $Z = 75$) and Osmium (Os, $Z = 76$) studied to date and the correlation of the decay of ^{194}Re nuclei with γ rays from transitions in their daughter ^{194}Os nuclei. Previously unreported γ-ray transitions with energies 194, 349 and 554 keV are identified, these transitions were confirmed to be associated with decays from higher spin states in ^{194}Os in the present work. This study also provides the first measurements of β-half-lives in ^{194}Re. The results on the low-lying states in ^{194}Os are compared to energy systematics in the region and with predictions of shape calculations on this nucleus. Candidates for the (three) β^--decaying states identified in ^{194}Re are also presented, based on the results of Nilsson Multi Quasi Particle (MQP) calculations for axially symmetric prolate and oblate configurations.

The second part of this work is aimed at obtaining information on the structure of heavy neutron-rich nuclei with $Z < 82$ and $N > 126$. This study provides the first spectroscopic data on an even-even nucleus in this region, namely $^{208}_{80}\mathrm{Hg}_{128}$. Isomeric states in the $N = 128$ isotones, ^{208}Hg and ^{209}Tl have been identified for the first time. The experimental results are compared with the results of restricted basis shell model calculations which suggest well-defined shell model configurations for the observed isomeric states. Some of the work presented in this thesis has been reported in conference proceedings [40, 41, 42], and published in Ref. [43].

The Chapters of the thesis are presented as follows: Chapter 2 gives an outline of the relevant nuclear structure theory; the experimental techniques used in the current work are described in Chapter 3. Chapter 4 describes the experimental details and particle identification techniques used in projectile fragmentation spectroscopy, together with the experimental results and discussion of the ^{194}Re β-decay to ^{194}Os. In Chapter 5 the experimental details, the experimental results and discussions of $N = 128$ isotones, ^{208}Hg and ^{209}Tl are presented. Finally, Chapter 6 gives a summary of this study.

Chapter 2

Theory of nuclear structure

2.1 Nuclear models

2.1.1 Nuclear shell model

The study of nuclear properties shows evidence of nuclear shells similar to those observed in atomic structure. One piece of clear evidence in the nuclear case is the sharp discontinuity in nucleon separation energies for certain numbers of Z (proton number) and N (neutron number), known as magic numbers 2, 8, 20, 28, 50, 82 and 126, where the separation energy of the last nucleon is notably larger than the corresponding value in the neighboring nuclei. Further evidence for this shell structure is the energy required to excite nuclei which contain a magic number of protons or neutrons. In the case of the electronic shells in atoms the picture is very clear, since there is a central Coulomb potential due to the charge carried by the nucleus and electrons [44]. Therefore, there are regular and smooth variations of atomic properties within a subshell, but rather sudden and dramatic changes in properties when filling one subshell and entering the next [26]. Figures 2.1 and 2.2 show the effect of the change in subshell occupancy on the ionization energy of the elements and the analogous measured separation energies (of protons and neutrons) with the nucleon number.

In the case of the nucleus there is no external potential (such as the Coulomb potential in the atomic case) but the nucleons move in the potential that itself arises from the combined effect of all the nucleons. The Spherical Shell Model was introduced to describe spherical nuclei. It utilises a Woods-Saxon [46] potential coupled with a

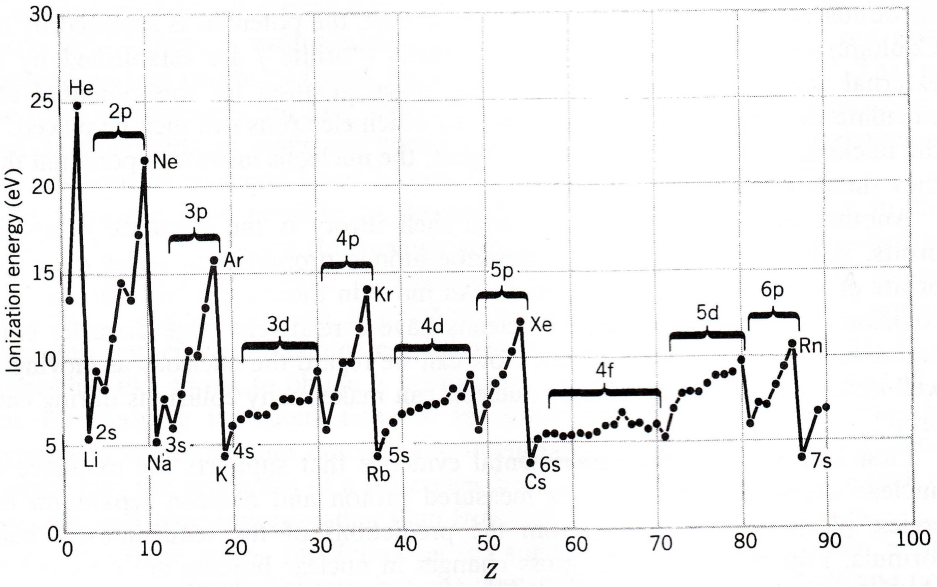

Figure 2.1: Ionization energy of the elements. The smooth variations in these properties correspond to the gradual filling of an atomic shell and the sudden jumps show transitions to the next shell, figure taken from Ref. [26].

spin-orbit interaction. The spin-orbit term arises from a coupling between orbital angular momentum l and the intrinsic angular momentum s of the individual nucleons such that $\overrightarrow{j} = \overrightarrow{l} + \overrightarrow{s}$. For each j-shell the energy levels are degenerate with $(2j+1)$, possible occupancies which are further labelled by the magnetic quantum number m_j (the projection of j). The Woods-Saxon potential can be described by [46]:

$$V(r) = \frac{-V_\circ}{1 + exp[\frac{r-R}{a}]} \tag{2.1}$$

where r is the radial distance from the centre of the potential and a is the skin thickness diffuseness parameter, R is the radius ($R = 1.25A^{1/3}$) and $V_\circ$ defines the depth of the potential. Figure 2.3 shows the single-particle energy levels of the independent particle shell model.

For high-j orbitals the spin-orbit coupling causes the $l+1/2$ partner for a given j value to be pushed down in energy relative to the $l-1/2$ spin-orbit partner. Therefore one of these "high-j intruder"orbitals appears in a major oscillator shell lower that it would have been without the spin-orbit term. This is precisely the effect required in order to reproduce the magic numbers. A real shell (bounded by the magic numbers) contains a majority of levels of one parity and one orbital of the opposite parity. It

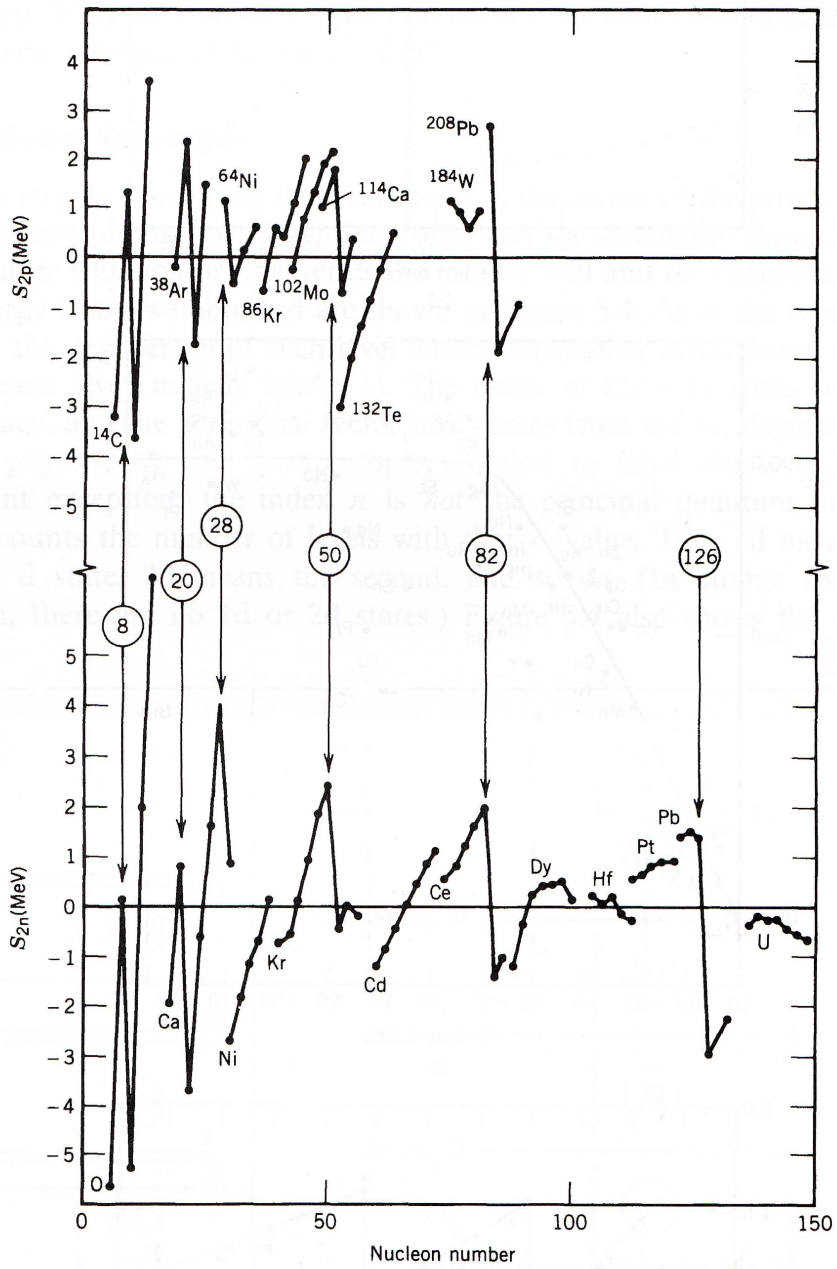

Figure 2.2: Top: Two-proton separation energies of sequences of isotones. *Bottom:* Two-neutron separations energies of sequences of isotopes. The sudden changes show the magic numbers. The data are differences between the measured values [45] and the predictions of the semi-empirical mass formula. This figure is taken from Ref. [26].

is conventional to call this orbital an "intruder" or "unique parity" orbital [47]. This model can explain many features of spherical nuclei but needs modifying to describe nuclei with many nucleons outside closed shells; the residual interactions between these many valence nucleons may be more simply described in terms of deformed potentials [25].

2.1.2 Nuclear deformation

Nuclei with proton (Z) and neutron (N) numbers far from the closed shells are not described well by using the independent particle spherical shell model. It is useful for a deformed potential to be assumed for these regions of the nuclear chart. Some experimental observations such as the presence of rotational band structures and large ground state / 1^{st} excited state quadrupole moments are able to be explained by using the assumption of a nuclear (charge) deformation away from a spherical shape. The nuclear radius of a deformed nucleus can be described [49] by the expression:

$$R(\theta,\phi) = R_{av}[1 + \sum_{\lambda=2}^{\infty}\sum_{\mu=-\lambda}^{\lambda}\alpha_{\lambda\mu}Y_{\lambda\mu}(\theta,\phi)] \tag{2.2}$$

where $\alpha_{\lambda,\mu}$ are the coefficients of the spherical harmonics $Y_{\lambda\mu}(\theta,\phi)$ and R_{av} is the average radius, $R_{av} = R_{\circ}A^{\frac{1}{3}}$. The radius of axially symmetric nuclei (independent of ϕ) can be expressed as

$$R(\theta) = R_{av}[1 + \beta_2 Y_{20}(\theta)] \tag{2.3}$$

where the deformation parameter $\beta_2 = \alpha_{20}$ is related to the axes of the spheroid by:

$$\beta_2 = \frac{4}{3}\sqrt{\frac{\pi}{5}}\frac{\triangle R}{R_{av}} \tag{2.4}$$

$\triangle R$ is the difference between the semi-major and semi-minor axes of the ellipse. If $\beta_2 > 0$ the nucleus has the elongated form of a prolate ellipsoid, if $\beta_2 < 0$ the nucleus has the flattened form of an oblate ellipsoid, and if $\beta_2 = 0$ then the nucleus is spherical. A larger value of β_2 represents a more deformed nucleus. In the case where the nucleus has axially asymmetry, a second parameter γ enters into the description of the nuclear shape. The relationship between the γ deformation and the $\alpha_{\lambda\mu}$ coefficients can be

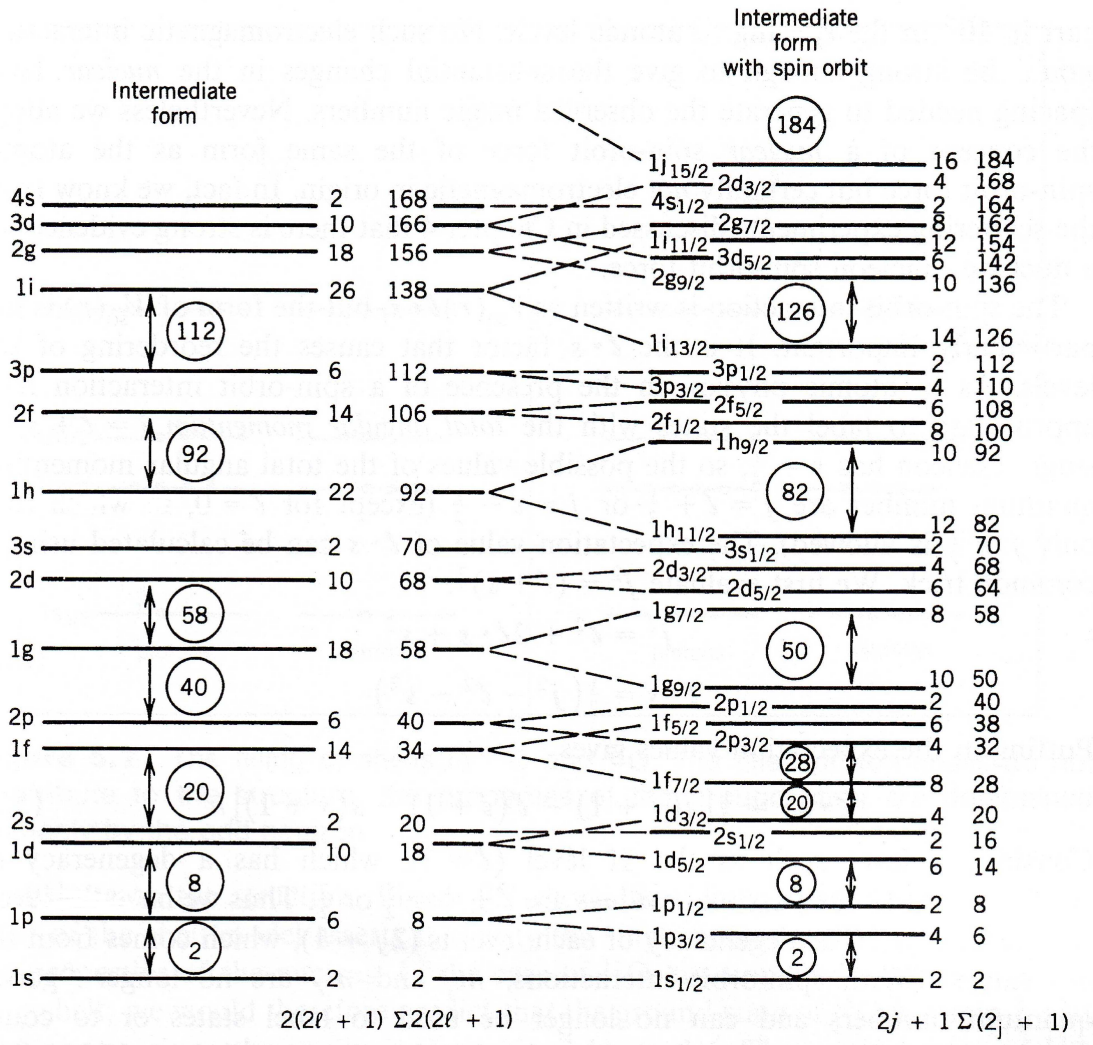

Figure 2.3: The single-particle energy levels of the independent particle shell model. *Left:* A Simple Harmonic Oscillator potential (SHO), *center:* Woods-Saxon potential and *right:* A Woods-Saxon potential coupled with a spin-orbit potential. This figure is taken from Ref. [48].

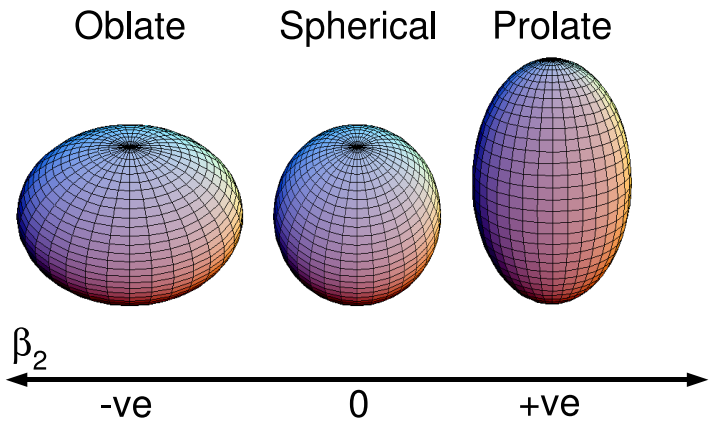

Figure 2.4: Diagram showing extreme versions of oblate, spherical and prolate shapes. This figure is modified from Ref. [25].

described as follows [50],

$$\alpha_{20} = \beta_2 cos\gamma \tag{2.5}$$

$$\alpha_{22} = \alpha_{2-2} = \frac{1}{\sqrt{2}}\beta_2 sin\gamma \tag{2.6}$$

The γ deformation is measured in degrees; $\gamma = 0°, -120°$ and $\gamma = 60°, -60°$ correspond to prolate and oblate shapes respectively. Others γ values correspond to triaxial shapes. Figure 2.4 is shown a schematic diagram for idealised oblate, spherical and prolate shapes.

2.1.3 Collective model

The nuclear shell model is based on the assumption that the neutrons and protons are arranged in stable quantum states in a potential well which is common to all of them. Many nuclei can be described as though most of the nucleons form an inert core and low-energy excited states are determined by excitations of a few nucleons "outside "the core [15]. The nuclear shell model has proved successful in reproducing the ground-state properties and low-lying excited states for many nuclei, especially near

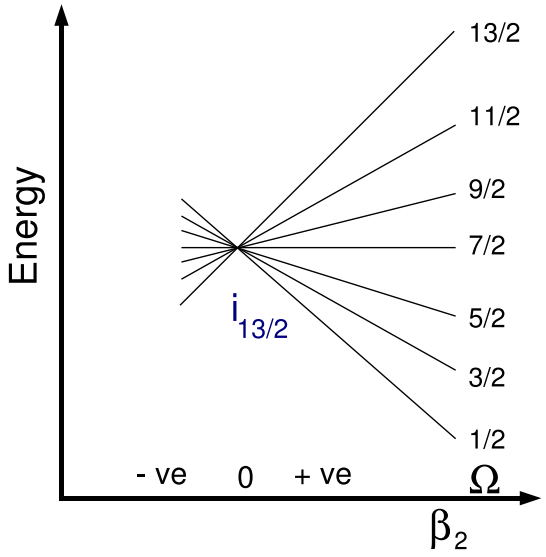

Figure 2.5: Schematic of the angular splitting of a $i_{\frac{13}{2}}$ state into its individual magnetic substates in a deformed potential taken from Ref. [25].

shell closures. However, it fails to describe the properties of the nuclei between the shell closures (i.e. nuclei with a significant number of valence neutrons and protons). Therefore, it is necessary to identify not simply the motion of a few valence nucleons, but rather the whole nucleus. These properties are known as *collective properties*, in which many nucleons participate cooperatively [26]. The two main kinds of collective motion in nuclei are rotations and vibrations:

Nuclear rotations

For nuclei with a non-spherical shape, collective rotational motion can be observed (the rotational motion can be observed only if there is a deviation from spherical symmetry). Therefore, deformed nuclei such as those with a prolate shape (see section 2.1.2) can rotate about one of its axes, but not about its third (symmetry) axis. Classically, the rotational angular momentum is given by $\mathcal{J}w$, where $\mathcal{J}$ is the moment of inertia and w is the the angular frequency of the rotation. The rotational energy for the classical relation is obtained by [15, 25]:

$$E_{rot}(I) = \frac{1}{2}\mathcal{J}w^2 \tag{2.7}$$

The moment of inertia is equal to:

$$w = \frac{I\hbar}{\mathcal{J}} \tag{2.8}$$

Combining the two equations above we obtain

$$E_{rot}(I) = \frac{1}{2}\frac{(I\hbar)^2}{\mathcal{J}} \tag{2.9}$$

Substituting the quantum mechanical results for the value of the square of rotational angular momentum, this gives

$$E_{rot}(I) = \frac{\hbar^2}{2\mathcal{J}}\left[I(I+1)\right] \tag{2.10}$$

For a perfect, idealised axially symmetric deformed even-even nucleus, the rotational levels take the following rotational energy values [26, 25]:

$$E(0^+) = 0 \tag{2.11}$$

$$E(2_1^+) = 6\frac{\hbar^2}{2\mathcal{J}} \tag{2.12}$$

$$E(4_1^+) = 20\frac{\hbar^2}{2\mathcal{J}} \tag{2.13}$$

$$E(6_1^+) = 42\frac{\hbar^2}{2\mathcal{J}} \tag{2.14}$$

Therefore, for a perfect axially symmetric rotor, the energy ratio $E(4_1^+)/E(2_1^+)$ is equal to 3.33 [25].

Nuclear vibrations

The shape of nuclei with Z and / or N numbers close to shell closures is assumed to be near-spherical. It is possible for such nuclei to vibrate about this spherical shape due to the residual interaction between the few valence nucleons. The quantum of vibrational energy is called *a phonon* which is of described by a defined multipolarity, λ. A $\lambda = 1$ deformation corresponds to a collective electric dipole excitation, which represents a shift in the centre of mass of the nucleus and which cannot occur for a

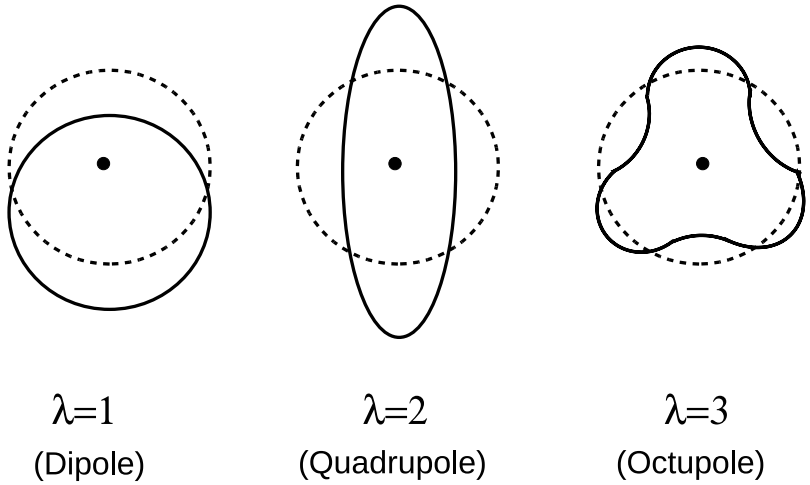

Figure 2.6: Schematic representation of the lowest three nuclear vibrational modes. This figure is taken from Ref. [26].

nucleus as a whole in the absence of external forces [15]. Figure 2.6 shows a schematic representation of the lowest three energy vibrational modes of a nucleus.

The quadrupole ($\lambda = 2$) excitation is the next lowest order vibrational mode. This requires no compression or separation of protons and neutrons. The ground states of all even-even nuclei have 0^+ [25], therefore by adding one quanta of the vibrational energy, a quadrupole phonon (two units of angular momentum), means that the first excited state has spin / parity 2^+. For two-quadrupole phonons of vibrational excitation, a triplet of states with spin of 0^+, 2^+ and 4^+ with about twice the energy of the single-phonon state are observed [25].

Octupole vibrations are associated with $\lambda = 3$, which carries three units of angular momentum and has negative parity (the parity, π, is given by (-1^λ)). The energy of the (3^-) octupole vibrational states are usually found to lie somewhat higher than the energy of 2^+ vibrational state [15, 25, 26].

2.1.4 Multi-quasiparticle excitations

The proton and neutron separation energies exhibit an odd-even effect, indicating an extra binding in the 0^+ ground states of even-even nuclei [25], this behavior is described in terms of the *pairing interaction*. The pairing interaction in nuclei is very important and is defined to be an attractive interaction acting only on two identical particles coupled to total angular momentum 0^+ states [25]. The extra binding energy provided by pairs of nucleons can be appreciated through the relative abundance of even-even (166), even-odd (110) and odd-odd (9) stable nuclear ground states across the Segré chart [51].

For deformed nuclei, the probability for the k^{th} orbital to be occupied and unoccupied by a pair of nucleons are v_k and u_k respectively, so

$$\mid v_k^2 \mid + \mid u_k^2 \mid = 1 \tag{2.15}$$

In the ground state of a nucleus, pairs of nucleons occupying orbitals near to the unoccupied level can move to the "empty "single-particle states. When a single nucleon is excited to a previously unoccupied level, the energy, ε_k, is changed due to the fact that pairs of nucleons cannot move to single occupied levels (this is called blocking). The state at the new energy is called *a single-quasiparticle* state with energy given by

$$E_k = \sqrt{(\varepsilon_k - \mu)^2 + \triangle^2} \tag{2.16}$$

where μ is the Fermi energy which lies in the region between the occupied and unoccupied orbitals and $\triangle$ is the pair gap given by

$$\triangle = G \sum_{k \neq k_j} u_k v_k \tag{2.17}$$

G is called the monopole pairing strength, and k_j indicates singly occupied levels.

2.1.5 The Nilsson model

The Nilsson model provides a microscopic basis for descriptions of rotational and vibrational collective motion that is directly linked to the spherical shell model [25]. In the Nilsson model [52], a deformed harmonic oscillator potential is used to solve the

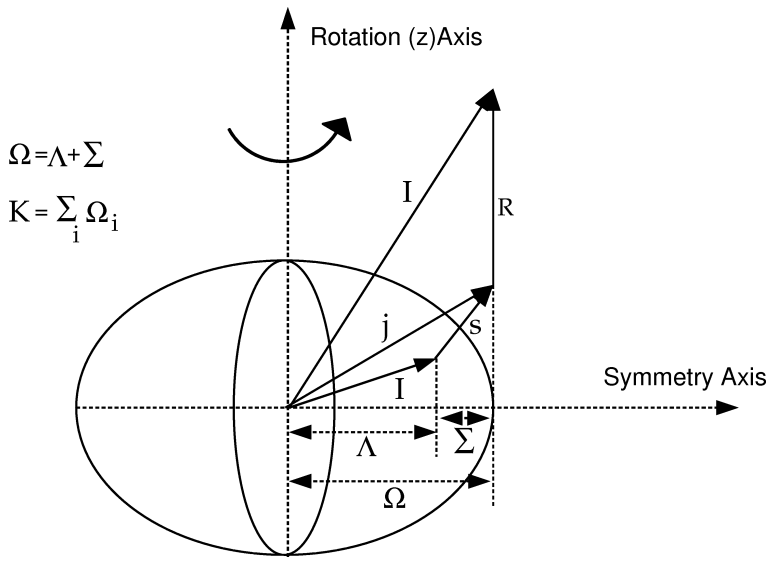

Figure 2.7: Schematic representation of the quantum numbers associated with an axially symmetric deformed nucleus, taken from Ref. [53].

Schrödinger equation. The orbital angular momentum, l, is no longer a good number and each single particle state is split into $(2j + 1)/2$ levels. The energy of the orbit depends on its orientation with respect to the nuclear symmetry axis. Each j orbital undergoes an energy splitting of its magnetic sub-states and therefore each individual sub-state has an orbital plane at a different angle to the symmetry axis (see figure 2.5). The orientation of the orbital can be specified by the magnetic sub-state of the nucleon which is the projection of the total angular momentum on the symmetry axis, Ω. For multiparticle states, K is sum of Ω for all valence nucleons, $K = \sum_i \Omega_i$ and both $K = |\Omega_1 \pm \Omega_2|$ are allowed. The energy of a nucleon depends on the angle of the orbital θ, which is approximately equal to

$$\theta = sin^{-1}(\Omega/j) \tag{2.18}$$

The low-Ω values correspond to the orbital motion near the bulk of the nuclear matter (see figure 2.6), and vice versa. Therefore the nucleon is on average further away from the rest of the bulk nuclear matter when it has a large angular momentum projection (i.e. for high Ω). Nilsson orbits are labelled as follows:

$$\Omega^{\pi}[Nn_z\Lambda] \tag{2.19}$$

where Ω is the projection of the total angular momentum on the symmetry axis, π is the parity of the orbital, N is the principal quantum number denoting the major shell, n_z is the number of nodes in the wave function in the z direction and Λ is the component of the orbital angular momentum along the z (i.e. the symmetry) axis. The value of Ω can be defined as $\Omega = \Lambda \pm \Sigma$ (where $\Sigma = \frac{1}{2}$, and is the projection of the intrinsic nucleon spin on the symmetry axis). Figure 2.8 shows the Nilsson diagram for protons $50 \geq Z \geq 82$, taken from Ref. [54].

2.2 Radioactive decay

2.2.1 Gamma decay

Many α and β decays and indeed most nuclear reactions leave the final nucleus in an excited state which decays to its ground state through the emission of one or more γ rays. The study of γ-ray emission is of particular importance in the use of the nuclear spectroscopy.

Let us consider a γ-ray transition from an initial excited state of energy E_i, angular momentum I_i and parity π_i to the final state E_f, angular momentum I_f, the parity π_f and $M_\circ$ is the rest mass of the nucleus. The energy of the γ ray can be described by [26]:

$$\triangle E = E_i - E_f = E_\gamma + \frac{E_\gamma^2}{2M_\circ c^2} \tag{2.20}$$

where $\triangle E \gg \frac{E_\gamma^2}{2M_\circ c^2}$ and the angular momentum will be within the limits [26]:

$$|I_i - I_f| \leq L \leq I_i + I_f \tag{2.21}$$

For electric (E) and magnetic (M) transitions respectively, the parity change in the transition is given by the selection rules [26]:

$$\triangle\pi(EL) = (-1)^L \tag{2.22}$$

$$\triangle\pi(ML) = (-1)^{L+1} \tag{2.23}$$

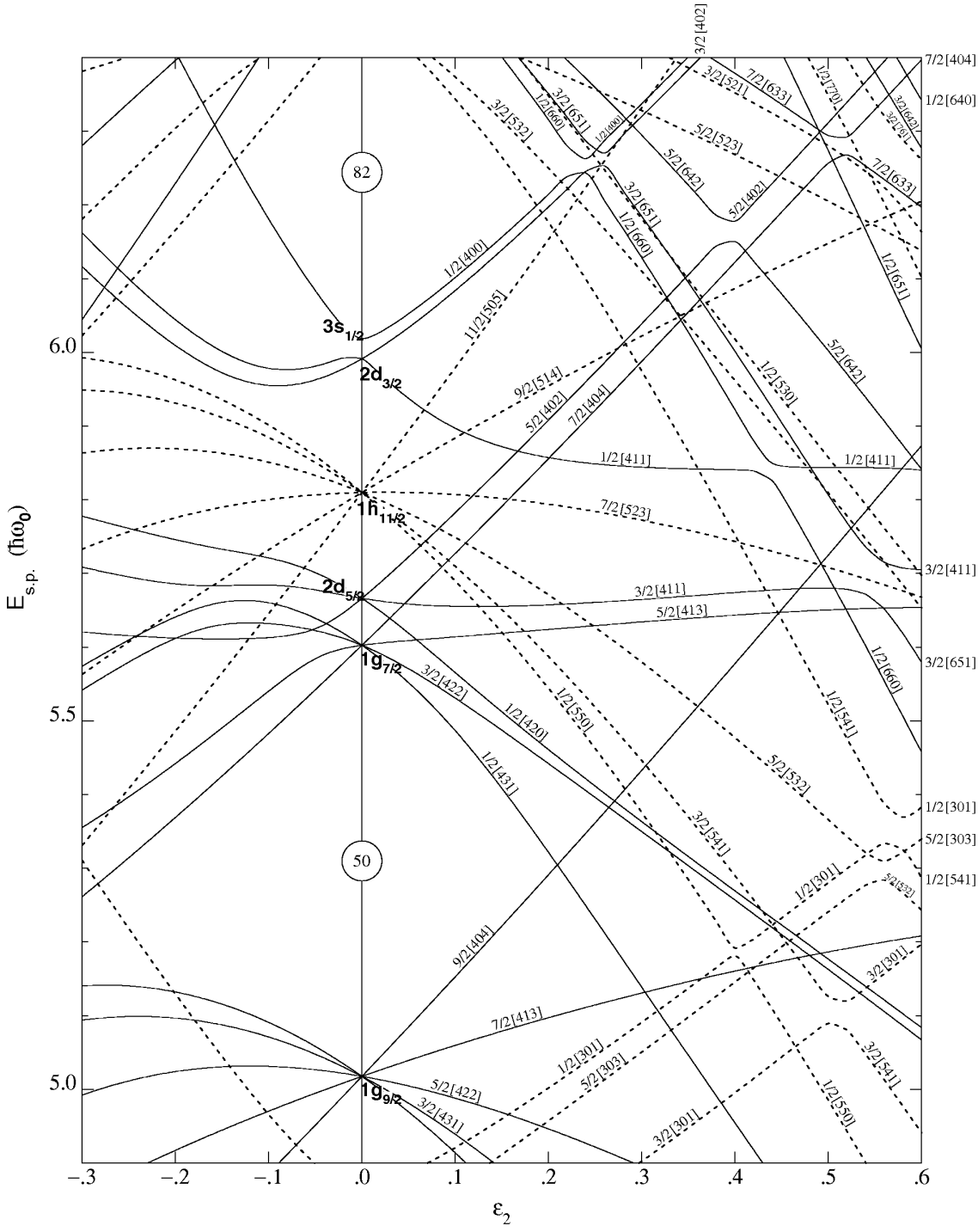

Figure 2.8: Nilsson model for protons, $50 \geq Z \geq 82(\varepsilon_4 = \varepsilon_2^2/6)$. This figure is taken from Ref. [54].

where L is the angular momentum of the transition. Note that the same order of electric and magnetic multipoles always have opposite parity. Since photons have an intrinsic spin of $1\hbar$, the transitions between two 0^+ or 0^- states, i.e. pure $\triangle L = 0$ are forbidden to proceed via γ decay. Such transitions may proceed via internal pair formation (creation of an e^+ e^- if $E_\gamma > 1.022$MeV) or internal conversion.

The total electromagnetic transition probability can be determined by [55]:

$$\lambda_{fi}(\lambda L) = \frac{8\pi(L+1)}{\hbar L((2L+1)!!)^2}\left(\frac{E_\gamma}{\hbar c}\right)^{2L+1} B(\lambda L; J_i \rightarrow J_f) \tag{2.24}$$

where $B(\lambda L)$ is the reduced transition probability for a transition of multipolarity, λ, which carries E_γ (in MeV) of energy and L units of angular momentum ($\hbar$). These reduced transition probabilities are given by the reduced matrix elements [55] for electric and magnetic transitions by the following equations:

$$B(EL; J_i \rightarrow J_f) = \frac{1}{2L_i+1}|\langle f|Q_L|i\rangle|^2 \tag{2.25}$$

$$B(ML; J_i \rightarrow J_f) = \frac{1}{2L_i+1}|\langle f|M_L|i\rangle|^2 \tag{2.26}$$

Q_L and M_L are the electric and magnetic multiple operators respectively. Transition probabilities in terms of the *Weisskopf single-particle estimates* are given by [55]:

$$\lambda(EL) = \frac{8\pi(L+1)}{L((2L+1)!!)^2}\frac{e^2}{4\pi\varepsilon_\circ\hbar c}\left(\frac{E}{\hbar c}\right)^{2L+1}\left(\frac{3}{L+3}\right)^2 cR^{2L} \tag{2.27}$$

and

$$\lambda(ML) = \frac{8\pi(L+1)}{L((2L+1)!!)^2}\left(\mu_p - \frac{1}{L+1}\right)^2\left(\frac{\hbar}{m_p c}\right)^2\left(\frac{e^2}{4\pi\varepsilon_\circ\hbar c}\right)\left(\frac{E}{\hbar c}\right)^{2L+1}\left(\frac{3}{L+3}\right)^2 cR^{2L-2} \tag{2.28}$$

where $R = R_\circ A^{1/3}$, μ_p is the magnetic moment, m_p is the mass of the proton. It is customary to replace the factor $\left(\mu_p - \frac{1}{L+1}\right)^2$ by a factor of 10, which gives the estimates for the lower multiple order [26], see Table 2.1. These represent the *Weisskopf estimates* for different multipolarity [26].

Based on these *Weisskopf single-particle estimates*, two conclusions about transition probabilities can be obtained [26]: *(i)* The lower multipolarities are dominant,

Table 2.1: Weisskopf single − particle estimates for different electromagnetic multipolarities. Values are in s^{-1} units when E in MeV and A is the atomic mass number [26].

$T(E1) = 1.0 \times 10^{14} A^{2/3} E^3$	$T(M1) = 5.6 \times 10^{13} E^3$
$T(E2) = 7.3 \times 10^{7} A^{4/3} E^5$	$T(M2) = 3.5 \times 10^{7} A^{2/3} E^5$
$T(E3) = 3.4 \times 10^{1} A^{2} E^7$	$T(M3) = 1.6 \times 10^{1} A^{4/3} E^7$
$T(E4) = 1.1 \times 10^{-5} A^{8/3} E^9$	$T(M4) = 4.5 \times 10^{-6} A^{2} E^9$

increasing the multipole order by one unit the transition probabilities reduces by a factor of 10^{-5} [26]; and *(ii)* For a given multipole order, electric radiation typically has a higher transition probability than magnetic radiation by two orders of magnitude in medium and heavy nuclei [26].

2.2.2 Internal conversion

Internal conversion is an electromagnetic process that competes with γ-ray emission [26]. In the case of internal conversion, a bound electron (usually from the inner K or L atomic shells of the atom) is emitted. In contrast to β decay, the electron is not created in the decay process but rather, previously occupied a bound state in the atomic shell [26]. The competing γ-ray transition energy for such a decay is the difference between the initial and final states, $E_t = E_i - E_f$, minus a small amount of kinetic energy for the recoiling nucleus. The electron emitted in the competing internal conversion process will have a kinetic energy such that

$$E_k \cong E_t - B_i \tag{2.29}$$

where B_i is the binding energy of the electron in the i^{th} electron shell. The emission of the electron and the resulting rearrangement of the electrons in the atomic shells will lead to the emission of characteristic X-rays or Auger electrons. The internal conversion coefficient [26] can be defined by:

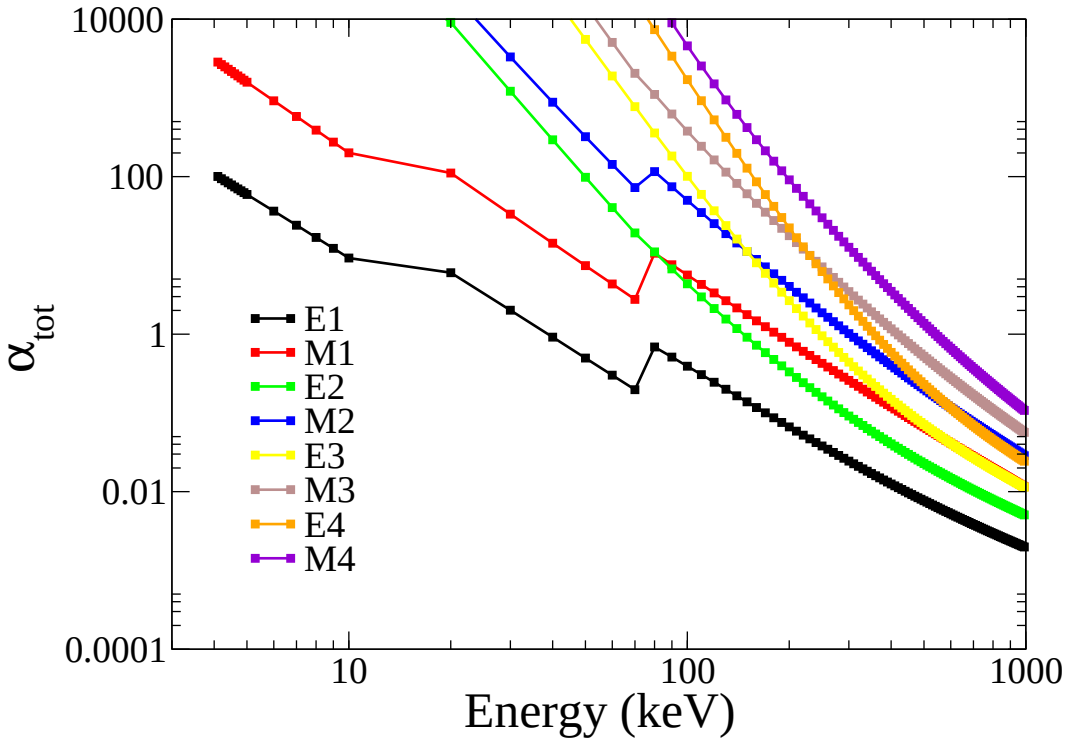

Figure 2.9: Theoretical total internal conversion coefficients for Os isotopes, taken from Ref. [56].

$$\alpha = \frac{I_e}{I_\gamma} \tag{2.30}$$

where I_e and I_γ are the decay probabilities due to electron conversion and γ-ray emission respectively. The total internal coefficient, α_T, is described by the sum of the individual coefficient for each atomic shell, such that:

$$\alpha_T = \alpha_K + \alpha_L + \alpha_M + ... \tag{2.31}$$

The total decay probability λ_T is related to the γ-ray partial decay probability by the relationship:

$$\lambda_T = \lambda_\gamma(1 + \alpha_T) \tag{2.32}$$

The internal conversion coefficients for electric and magnetic multipoles are given by the following equations [26]:

$$\alpha(EL) \approx \frac{Z^3}{n^3}\left(\frac{L}{L+1}\right)\left(\frac{e^2}{4\pi\epsilon_\circ\hbar c}\right)^4\left(\frac{2m_ec^2}{E_t}\right)^{L+\frac{5}{2}} \tag{2.33}$$

$$\alpha(ML) \approx \frac{Z^3}{n^3}\left(\frac{e^2}{4\pi\epsilon_\circ\hbar c}\right)^4\left(\frac{2m_ec^2}{E_t}\right)^{L+\frac{3}{2}} \tag{2.34}$$

where Z is the atomic number, E is the transition energy and n is the principal quantum number of the electron shell. The main features of the conversion coefficients can be given in the following (approximate) expressions [26]:

(i) The conversion coefficients increase as Z^3 and so the electron conversion process is more probable for heavy nuclei than for light nuclei.

(ii) The conversion coefficients decreases rapidly with increasing transition energy.

(iii) The conversion coefficients increase rapidly as the multipole order increases.

(iv) The conversion coefficients decrease as $1/n^3$ for higher atomic shells ($n > 1$).

(iiv) The conversion coefficients have higher probability for magnetic transitions compared to electric transitions of the same multipole order.

Figures 2.9 and 2.10 shows the theoretical total internal conversion coefficients for Osmium and Mercury isotopes respectively as a function of the transition energies [56].

2.2.3 β^- decay

An unstable nucleus on the neutron-rich side of the line of stability has a finite probability of undergoing β^- decay. When this process of decay takes place a neutron in the nucleus decays as follows:

$$n \;\rightarrow\; p \;+\; \beta^- + \overline{\nu}_e \tag{2.35}$$

where n and p are a neutron and proton respectively, β^- is a β-minus particle (an electron, created and emitted during the β^--decay process) and $\overline{\nu}_e$ is an electron antineutrino [57]. The probability of this process depends on the relation between the wave functions of the initial and final nuclear states.

In the allowed approximation, the electron and neutrino can not carry any orbital angular momentum and the only change in the angular momentum of the nucleus must result from the spins of the electron and neutrino, each of which has the value $s = \frac{1}{2}\hbar$. These two spins can be coupled parallel (total $S = 1$) or antiparallel (total $S = 0$). If the spins are antiparallel (which is known as a Fermi decay) then in the allowed approximation ($l = 0$) there can be no change in the nuclear spin [26]:

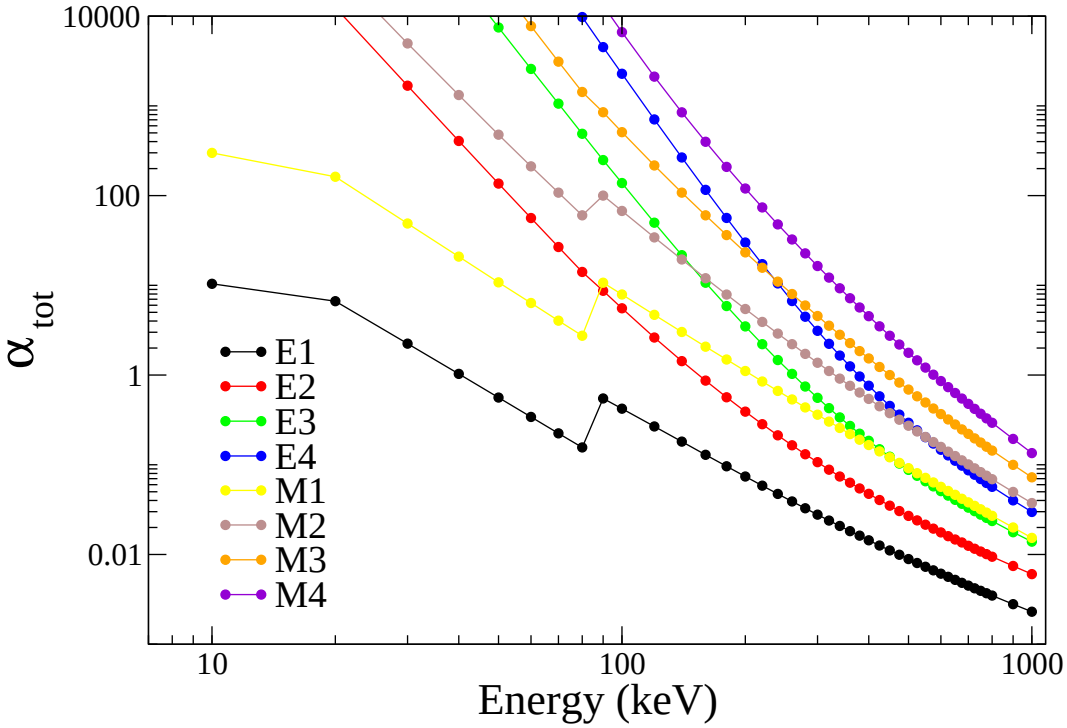

Figure 2.10: Theoretical total internal conversion coefficients for Hg isotopes, taken from Ref. [56].

$$\triangle I = |I_i - I_f| = 0 \tag{2.36}$$

If the electron and neutrino spins are parallel (which is called a Gamow-Teller decay), they carry a total angular momentum of $1\hbar$ and thus I_i and I_f must be coupled through a vector of length 1, such that:

$$\overrightarrow{I_i} = \overrightarrow{I_f} + 1 \tag{2.37}$$

This is possible only if $\triangle I = 0$ or 1. If the electron and neutrino carry no orbital angular momentum, then the parities of the initial and final states must be identical since the parity associated with orbital angular momentum l is $(-1)^l$. The selection rules for allowed β decay are thus defined as the follows [26]:

$$\triangle I = 0, 1 \qquad \triangle \pi \ (parity \ \ change) = no \tag{2.38}$$

Forbidden decays, are (usually) less probable than allowed decays, but if there is no probability for an allowed decay (from the above selection rules), then the forbidden decays are the only ones that can proceed. The most frequent occurrence of a forbidden decay is when the initial and final states have opposite parities [26]. To accomplish the change in parity, the electron and neutrino must be emitted with an odd value of the orbital angular momentum relative to the nucleus [26], and like allowed decays, they can occur with both Fermi couplings with the electron and neutrino spins opposite, ($S = 0$), and Gamow-Teller coupling with the spins parallel ($S = 1$). The coupling of $S = 0$ with $l = 1$ for the Fermi decays gives total angular momentum of one unit carried by the β-decay, so that $\triangle I = 0$ or 1. Coupling $S = 1$ with $l = 1$ for the Gamow-Teller decays give 0, 1, or 2 unit of total angular momentum, so that $\triangle I = 0, 1$, or 2. Thus the selection rules for the first-forbidden decays are [26]:

$$\triangle I = 0, 1, 2 \qquad \triangle \pi \ (parity \quad change) = yes \tag{2.39}$$

Coupling intrinsic spins of 0 or 1 to angular momentum of $l = 2$, in principle can change the nuclear spin by any integer amount from $\triangle I = 0$ to $\triangle I = 3$. The $\triangle I = 0$ and $\triangle I = 1$ cases fall within the selection rules for allowed decays, so the selection rules for the second-forbidden decays are [26]:

$$\triangle I = 2, 3 \qquad \triangle \pi \ (parity \quad change) = no \tag{2.40}$$

2.3 Projectile fragmentation reactions

Fragmentation is the reaction mechanism which occurs during the collision between two nuclei at relative energies higher than the Fermi velocity of the nucleons ($v_F \sim 10^7$ m/s), such that the target nucleons are effectively static during the fragmentation reaction. The collision of a heavy-ion projectile with a target can be described, to a first approximation, using a geometrical parameterisation. According to the size of the impact parameter, the collisions will be either central or peripheral [58]. In the first case, the collisions lead to processes such as multi-fragmentation. Peripheral collisions can result in the formation of fragments with masses close to the projectile, which can be described by a two-step abrasion-ablation model [59]. The abrasion model, relies on the concept of a clean cut of the projectile nucleus by the target (and vice versa).

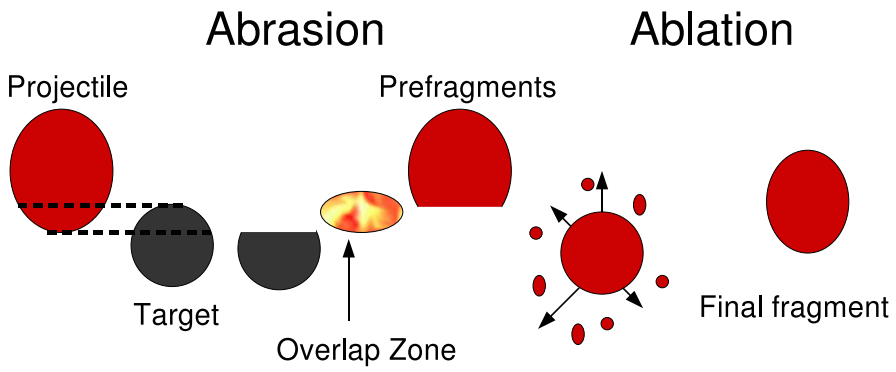

Figure 2.11: A schematic view of the projectile fragmentation reaction mechanism.

According to this model, if the relative velocity of the reaction partners is much higher than the Fermi velocity of the nucleons, the nucleon-nucleon collisions are restricted to the overlap zone. The parts of the nuclei outside the overlap zone, called spectators or pre-fragments, are not affected by the initial collision. The impact parameter determines the number of nucleons removed from the projectile and the target. In the second, ablation stage, the hot prefragment either fissions or boils off/evaporates nucleons until the final fragment is formed with an excitation energy below the particle emission threshold. In the fragmentation process it is possible to populate many different nuclear species. This geometrical description is shown schematically in figure 2.11 and discussed in further detail in the Refs. [60, 61].

2.4 Isomeric states

Isomeric states are metastable states which correspond to excited states [62] of a nucleus with a lifetime longer than expected for a typical intrinsic state. A nuclear isomer occupies a higher excitation energy state than the ground state. The nuclear isomer will eventually release its excitation energy and decay towards the ground state. There is no strict formal limit on the half-life for an excited state to be considered as isomeric. The lifetimes of collective nuclear excited states are typically approximately 10^{-12} s. By contrast the isomeric state in ^{180}Ta has a half-life greater that 10^{15} years

[63]. A challenge for scientific discovery lies in the understanding of the formation of nuclear isomers (through a better comprehension of nuclear structure) and the ability to excite and de-excite isomers at will for a broad range of nuclear applications, including the exploration of nuclei with isomeric states in nuclear astrophysics to determine how they affect the creation of the elements in the universe. There are four main types of nuclear isomer: seniority, spin-trap, K and shape isomers.

2.4.1 Seniority

Seniority refers to the number of unpaired nucleons (ν) in a state of angular momentum J in the configuration j^n (i.e. the number of nucleons which do not couple to J=0). In the nuclear chart, seniority behavior (i.e. where seniority can be considered as a "good"quantum number) is most likely to be found near magic numbers where the collectivity inducing valence $p-n$ interactions are likely to be weak [25]. For example in $^{210}_{82}\mathrm{Po}_{128}$ [64], a $J^\pi = 8^+$ state is formed by the coupling of two protons in $h_{9/2}$ orbital and this state has seniority of two ($\nu = 2$). The ground state has $\nu = 0$ as all the nucleons are paired to $J^\pi = 0^+$. Therefore, to form state of higher spin it is necessary to break a pair of nucleons. Transitions from the $6^+ \rightarrow 4^+ \rightarrow 2^+$ states all have $\nu = 2$ and thus $\Delta\nu = 0$ while the transition from 2^+ to the ground state 0^+ which has $\nu = 0$ is therefore $\Delta\nu = 2$.

2.4.2 Spin traps

The existence of spin traps depends on the difficulty in meeting spin (and parity) selection rules, which are required to conserve angular momentum in electromagnetic decay. A decay from an excited state which requires a large change in the nuclear spin means that the electromagnetic radiation emission must proceed via a high multipolarity, (λ) transition to match the change of the spin. From the electromagnetic selection rules, selection a decay with larger change in angular momentum is related with smaller probability and longer half-life associated with that transition.

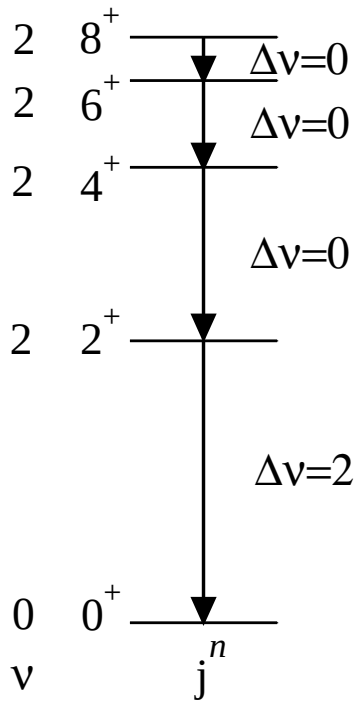

Figure 2.12: A schematic representation of seniority quantum numbers, this figure is taken from Ref. [65].

2.4.3 K isomers

This kind of isomer arises only in axially symmetric deformed nuclei which are found away from the closed shells. Most K-isomers have been found in $A \approx$180 nuclei region. K represents the projection of the total nuclear spin along the symmetry axis of the nucleus and is a quantum number in axially symetric nuclei [62]. The selection rule for an allowed electromagnetic decay with multipolarity λ, between initial and final states of K_i and K_i respectively given by

$$|K_i - K_f| = \triangle K \leq \lambda \tag{2.41}$$

Transitions with $\triangle K > \lambda$ violate this selection rule and are hindered. The degree of K-forbiddenness for a transition, ν, is defined as follows

$$\nu = \triangle K - \lambda \tag{2.42}$$

The extent of the hindrance to the transition probability is related to the degree of forbiddenness and the K-mixing which violates the K-quantum number [51]. The

hindrance per degree of K forbiddenness (or the *reduced hindrance*) is given by

$$f_\nu = \left[\frac{t^\gamma_{1/2}}{t^W_{1/2}}\right]^{1/\nu} \tag{2.43}$$

where $t^\gamma_{1/2}$ is the partial γ-ray half-life and $t^W_{1/2}$ is the corresponding Weisskopf single-particle estimate.

2.4.4 Shape isomers

Shape isomers occur when there is a secondary energy minimum at large elongation of the nucleus, the primary energy minimum correspond to the ground state [62]. Decay to the ground state by γ-ray emission in very heavy nuclei can compete with fission into two lighter nuclei for so called "fission"isomers [66].

Chapter 3

Experimental technique: Preparing the nuclei of interest

The experimental technique used for the production of heavy neutron-rich nuclei in the current work is the fragmentation of relativistic heavy projectiles. The experiments discussed required the use of a heavy-ion accelerator to provide the relativistic primary beams together with a high-resolution magnetic spectrometer with different detectors for identifying and separating the projectile residues produced in these reactions. The SIS/FRS facility of the Gesellschaft für Schwerionenforschung (GSI) is one of the best suited for these kinds of experiments. In this chapter the experimental equipment which was used for the beam delivery and for the production of the heavy neutron-rich nuclei is described.

3.1 The GSI accelerator system

The GSI accelerator complex facility located in Darmstadt, Germany, is one of the leading facilities for relativistic heavy-ion nuclear research. The accelerator system at GSI comprises of a two step accelerating process. Ions are first accelerated to energies of around 11.5 MeV per nucleon by UNIversal Linear ACcelerator (UNILAC). The ions are then injected into the SchwerIonen Synchrotron 18 (SIS-18) for full acceleration. Thin carbon foils at the front of SIS were used to increase the charge state of the ions of interest, which is needed to be able to reach the desired final energy [58]. The maximum energies achieved by SIS are determined by its maximum magnetic bending

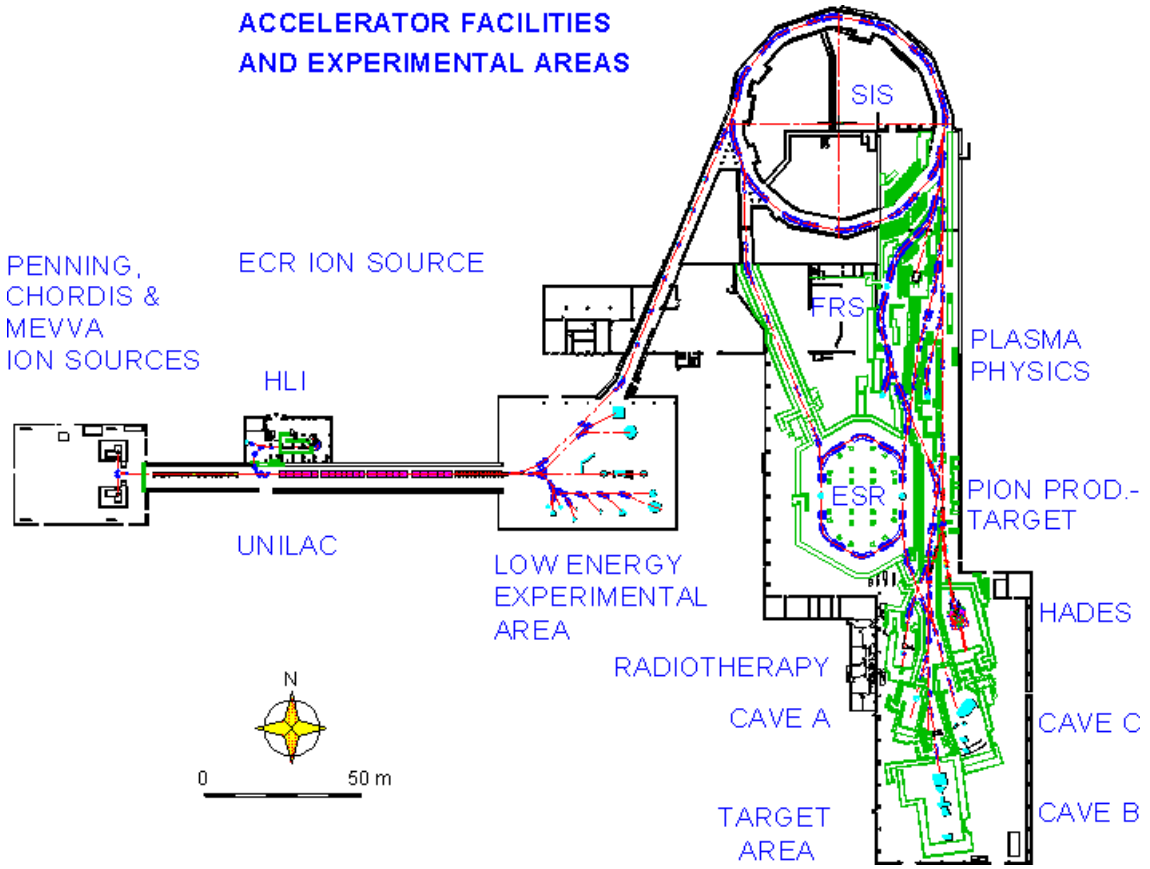

Figure 3.1: Schematic view of the GSI accelerator facilities and experimental areas taken from Ref. [67].

power of 18 Tm. The accelerating system at GSI has been able to provide heavy stable ion beams from hydrogen to uranium at maximum energies varying from 1 to 4.5 GeV per nucleon [38]. Figure 3.1 shows a schematic view of the GSI accelerator facilities and experimental areas [67].

3.2 Fragmenting the primary beam

The GSI FRagment Separator (FRS) is a high resolution magnetic spectrometer designed for research studies using relativistic heavy ions [38]. Heavy-ion beams with magnetic rigidities ranging from 5 to 18 Tm can be analysed using this spectrometer. The FRS has four stages, each one consisting of a 30° dipole magnet and a set of quadrupole and sextupole magnets for focusing (see figure 3.2). There are quadrupole doublets at the entrance and exit to each dipole magnet volume. Quadrupole triplet

magnets provide the correction optics for the focal planes. Sextupole magnets were positioned to enable fine adjustments to the optics. The total orbital length of the FRS is approximately 70 m. The FRS, being a magnetic spectrometer, separates the fragments according to the ratio of mass number over the ionic charge, and velocity according to the magnetic rigidity, where

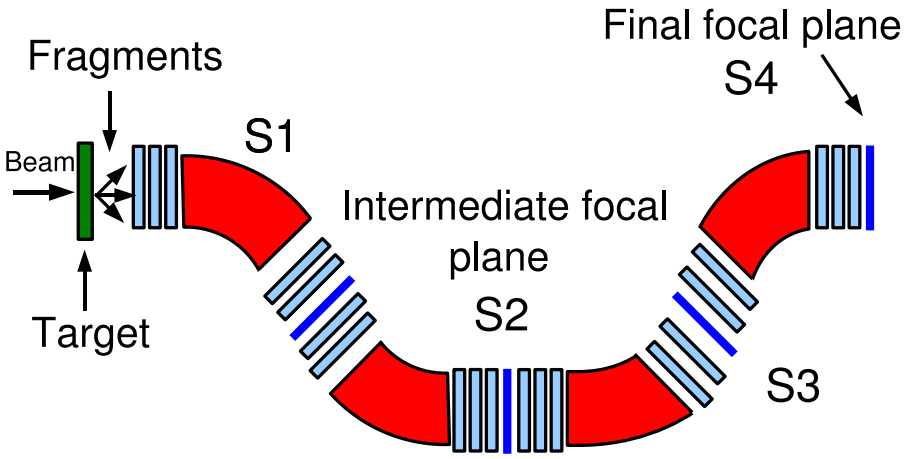

Figure 3.2: Schematic outline of the FRS at GSI adapted from Ref. [38]. Highlighted in red are the dipole magnets, the quadrupole magnets are blue. Localities along the separator are labelled by S1, S2, S3 and S4; the number index increases after each dipole magnet.

$$B\rho = \frac{p}{qe} = \gamma\beta c\,\frac{m}{qe} = \frac{A}{q}\beta\gamma\frac{uc}{e} \tag{3.1}$$

B is the magnetic field of the dipole magnets, ρ is the bending radius, p is the linear momentum from the relativistic parameters with ($\beta = v/c$, where v is the velocity of the ion and c is the speed of light), u is the atomic mass unit, q is the ionic charge state of the fragment and e is the electron charge (1.6 x 10^{-19}C). The fragmented nuclei leaving the target pass through a thin Nb foil which causes the majority of the fragments to be fully ionized. The main reason for this extra ionization of the secondary beam is for the benefit of particle identification and selection. The particle

separation process is highly dependent on the ionic charge state (q). A second benefit of electron stripping is the inhibition of internal conversion decay in flight. The time of flight for typical fragments through the FRS is ∼300 ns. During this time, the highly ionized nature of the transmitted ions results in a prohibiting of internal conversion and some highly converted isomeric half-lives can be effectively extended in-flight, allowing for measurements of some (short-lived) isomers which would have otherwise decayed in-flight [7].

3.3 Components of the FRagment Separator

All of the multiple species of reaction products from fragmentation can in principle be transmitted to the final focal plane of the FRS. Therefore it is necessary to achieve unambiguous particle identification of the ions. In the RISING set-up [38] used in the present work, this was achieved using measurements from three three kinds of beam line detector: *(i)* plastic scintillators for the time of flight determination (TOF) [68]; *(ii)* transmission ionization chambers for the atomic number measurements △E (∼Z) [69]; and *(iii)* multiwire proportional chambers for position measurements [70]. By combining the data collected from these beam line detectors and the deduced magnetic rigidity ($B\rho$) of the dipole magnets, quantities such as the mass to charge ratio (A/Q) and the atomic number (Z) can be evaluated and used to identify unambiguously which nuclear species have arrived at the final focal plane. Figure 3.3 shows a schematic view of the detector configuration at the final focus of the GSI Fragment Separator for the first experimental campaign of the Stopped RISING Active Stopper [71].

3.3.1 Dipole magnets

Dipole magnets are used for their ability of bend charged particles. The dipole magnets in the FRS have fixed bending radii and the magnetic field can be operated up to 1.6 T. The magnets are set up such that particle dispersion is across the horizontal plane, commonly referred to as the x dimension. The maximum acceptance width for particles is 100 mm either side of the beam centre. The nominal curvature radius of 11.25 m of the 30° dipoles constrains the maximum magnetic rigidity accepted by the FRS to 18 Tm.

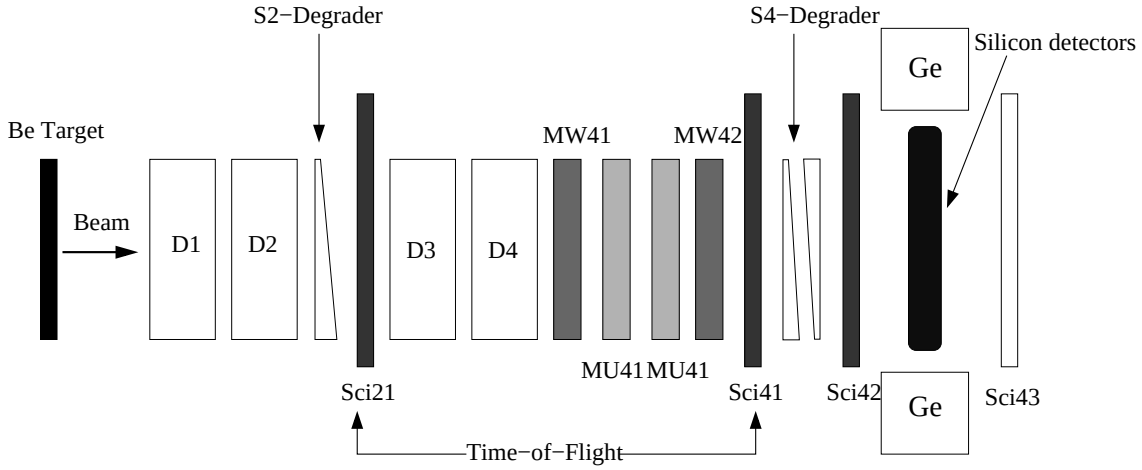

Figure 3.3: Schematic of the detector configuration of the GSI Fragment Separator. D=the dipole magnets; MW= MultiWire detectors; Sci=plastic scintillation detectors; MU=MUlti Sampling Ionising Chamber detectors. The number 2 and 4 corresponds to the detectors being placed at the intermediate and final focal plane of the GSI Fragment Separator respectively.

3.3.2 Quadrupole magnets

Quadrupole magnets are placed throughout the FRS. Quadrupoles are positioned before and after the dipole magnets. The geometric separation of these magnets combines with the magnetic field strengths for an optimum optical focus of the beam. They correct dispersions due to in-beam matter interactions prior to the dipole magnet and variances in the dipole magnet bending effects. Sextupole magnets are also placed before and after the dipole magnets to make second order corrections to the beam focusing.

3.3.3 Scintillator detectors

The scintillation detectors of the FRS are used for both time of flight measurements and for determining the horizontal position of the ions as they pass through the separator. Two plastic scintillation detectors were used at the intermediate (Sci21) and final focal planes (Sci41) of the FRS. The scintillators are made of Bicron BC420 [58], a plastic characterised by a high efficiency in the production of light, which has a fast time response of ≈ 5 ns.

The signals coming from the photo-multipliers were used as the start and stop of a Time to Amplitude Converter (TAC). The analog output of the TAC was then read by an Analog to Digital Converter (ADC). Figure 3.4 shows a simple diagram of the operation of a scintillator detector. The ions pass through Sci21 at time T_2 and through Sci41 at time T_4. However, before the signals arrive at the TAC, the output of the photomultipliers at Sci21 have to travel through a longer cable and therefore the arrival times of all signals at the TAC are rather close in real time. A time delay, T_0, is chosen in such a way that $T_2+T_0 > T_4$.

The measured Time of Flight, TOF^*, is the average of the right and left hand signals so that,

$$TOF^* = \frac{TOF_L^* \,.\, \alpha_L + TOF_R^* \,.\, \alpha_R}{2} = T_2 + T_\circ - T_4 \tag{3.2}$$

where α_L and α_R are the calibration factors used to convert the left and right TOF_L^* and TOF_R^* respectively into nanoseconds. The true TOF is then equal to

$$TOF = \frac{d_\circ}{v} = T4 - T2 \tag{3.3}$$

where $d_\circ$ is the flight path and v is the velocity of the ion.

3.3.4 Slits

Several pairs of slits are placed in the beam line. These slits are pairs of thick blocks of copper and are thick enough to stop any fragment incident on them, thereby allowing only particles between the two blocks to continue along the FRS. The copper blocks are adjustable across the x-plane of the beam and can be used asymmetrically. They are used to remove unwanted nuclei from the secondary beam by effectively reducing the maximum 200 mm width of the beam.

3.3.5 MultiWire proportional counters

A schematic drawing of the multi-wire (MW) counters [72] which were used in the current work for measuring the position of the particles in the x and y planes is shown in figure 3.5. These detectors consist of a gas filled chamber with four sets of wires in parallel planes, each holding a different potential. The MW counters have 100μm

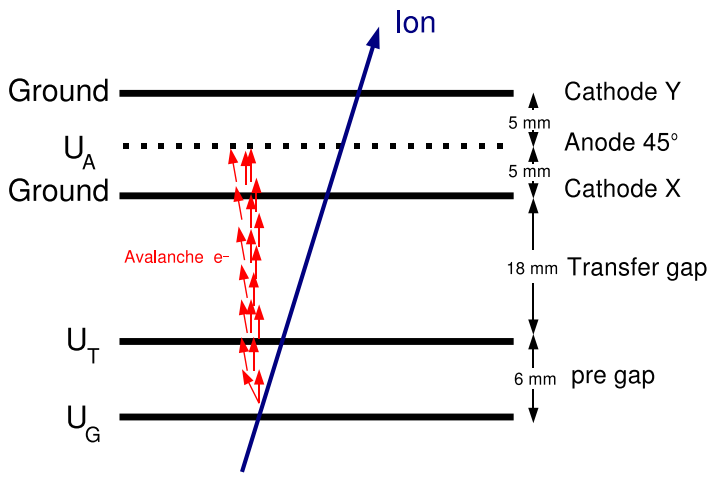

Figure 3.4: Schematic outline of a Multi-wire (MW) counter taken from Ref. [72].

Ti or 25μm krypton windows and are filled with a mixture of Ar, CO_2 and alcohol at atmospheric pressure. The output signal of the MW was achieved by a delay line. Each wire corresponds to a different delay time which is converted to a digital signal using Time to Digital Converters (TDCs). The MW detectors have the disadvantage that their wire structure introduces inhomogeneities in the projectile fragment beam. For this reason the MW were used for the calibration measurements only and then they were taken out of the beam line during the actual experiments.

3.3.6 Degraders

There are two degraders in the FRS, both of which are made from Aluminum. One is placed at the final focal plane of the FRS (S4) and is used to reduce the velocity of secondary beam particles. The other degrader is at the intermediate focal plane of the FRS (S2) and is angular (wedge shaped). The latter is used to separate the beam particles and provide a degree of channel selection in the transmitted secondary fragments. The angle of this wedge results in a varying thickness of the Aluminum across the horizontal plane of the beam line. Thus particles passing through the degrader at different positions pass through different thicknesses of material. There are two different modes which can be operated using this degarder, namely the achromatic and monochromatic modes:

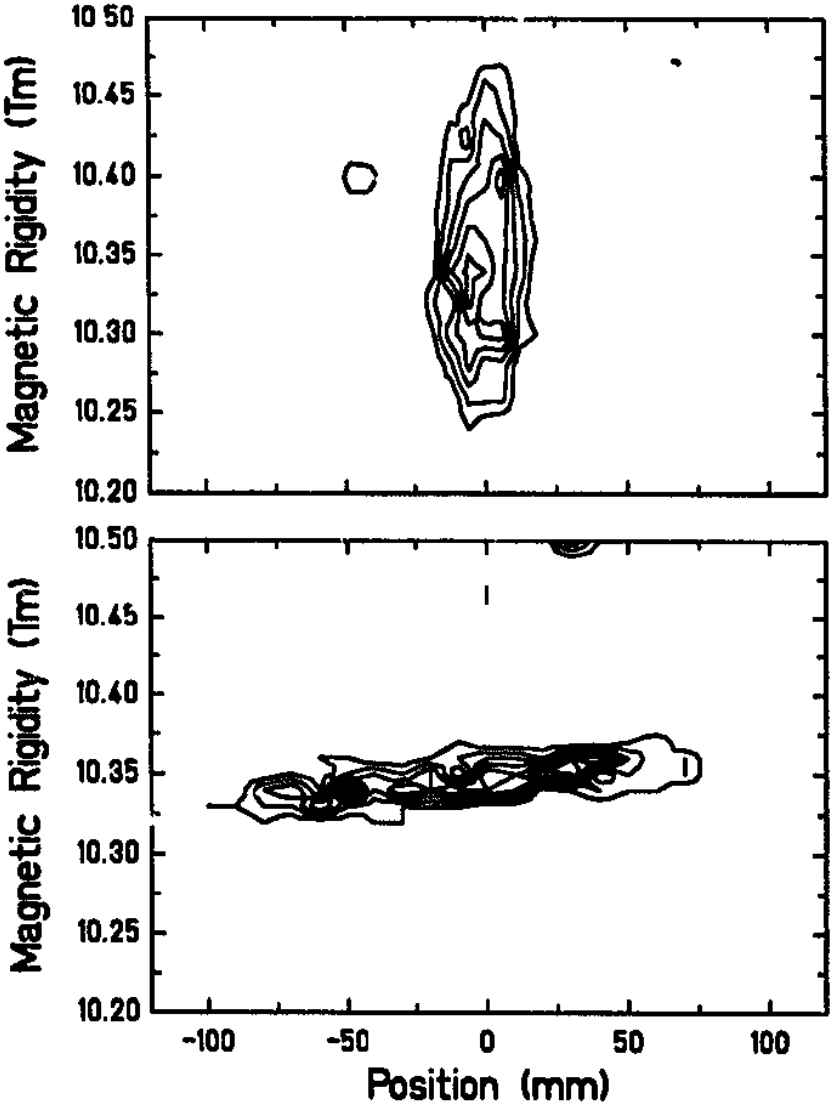

Figure 3.5: Contour plot of the ions distributions at the final focal plane of the FRS for the achromatic (upper panel) and monochromatic modes (lower panel) of the degrader. This figure is taken from Ref. [73].

Achromatic mode

The achromatic mode allows a relatively wide horizontal separation of isotopes at the final focal plane. The first stage of the separator selects in A/Z (assuming that all the ions passing the separator are fully stripped). It selects a band of isotopes along the line $A/Z = constant$, the width of which is determined by the velocity spread of the fragments [73]. The energy loss in the degrader is analyzed in the second part of the separator in terms of momentum change, which imposes a second cut in the (A, Z) plane. Therefore, in this way a single isotope species can be selected [73]. In the April 2008 experiment, the achromatic mode was used (see section 5.2).

Monochromatic mode

The monochromatic or "mono-energetic"mode is used to give a good separation of isotopes by range for experiments in which it is essential that the ions of interest are implanted precisely in the Silicon detector (at the final focal plane of the FRS) as a function of well defined depth. The energy loss of the fragment after traversing an intermediate monochromatic degarder does not depend on its position at the intermediate focal plane. In the March 2007 experiment (see section 4.2) the monochromatic mode was used for two specific reasons: *(i)* the implanted ions were implanted in the active stopper with similar energies for a given species. This improved the identification of the implanted ions and the correlations of their subsequent beta decays; and *(ii)* The mode minimized the probability of having several implanted ions in the same pixel within a typical correlation time (i.e. the use of monochromatic mode allowed the distribution of the implanted ions across as wide an area as possible in the active stopper). Figure 3.5 shows a schematic contour plots of the ion distributions at the final focal plane of the FRS for the achromatic (upper panel) and monochromatic modes (lower panel) of the degrader [73].

3.3.7 MUlti-Sampling Ionisation Chambers

At the final focal plane of the FRS two Multi Sampling Ionisation Chambers (MUSICs) were installed. There were used to determine the atomic number (Z) of the fragments passing through them. Figure 3.7 shows a schematic view of a MUSIC

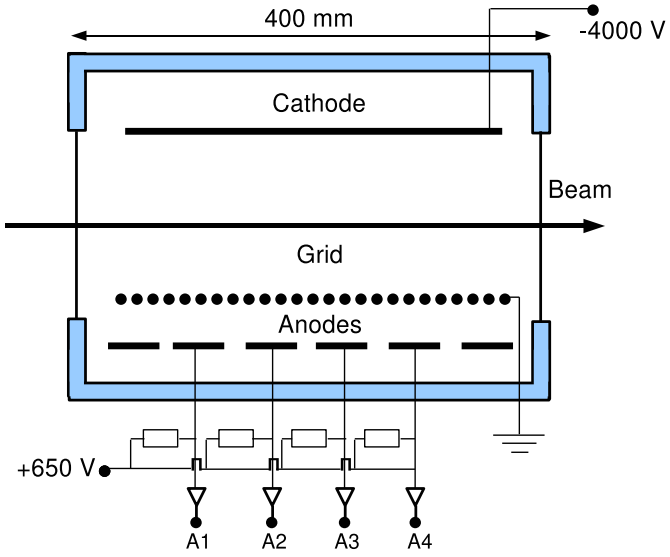

Figure 3.6: Schematic drawing of a MUSIC detector adapted from Ref. [69].

detector. The MUSIC chamber is a gas-filled container with an anode and cathode that are kept at a given working voltage. A fragment passes through the active region of dimension (276 x 150) mm^2. This generates a cloud of gas ions and free electrons, the amplitude of which depends on the speed of the incoming particle and is proportional to the square of its charge (i.e. $\triangle E \propto Z^2$). In the current work, the MUSIC chamber was 600 mm long and had exit windows made of thin krypton ($C_{22}H_{10}O_5N_2$) foils each of 25 μm thickness (to minimise the secondary interactions of the fragments). The chamber was filled with P10 gas (90% Ar and 10% CH_4) under atmospheric pressure at room temperature. Inside the chamber there were six anodes, but only the middle four were used for actual measurements (each one is 100 mm long), with the outer two used to assure the homogeneity of the electric field.

3.3.8 High-Purity Germanium Detectors

High-Purity Germanium (HPGe) detectors must be used at low temperature because of the effect of noise associated with thermal excitations; therefore the HPGe detectors were cooled during the experiments by using liquid nitrogen (T=77 K). A range of different possible interaction mechanisms for γ rays with matter are known but the most important these are described individually below, these being *(i)* the photoelectric effect, *(ii)* Compton scattering and *(iii)* pair production.

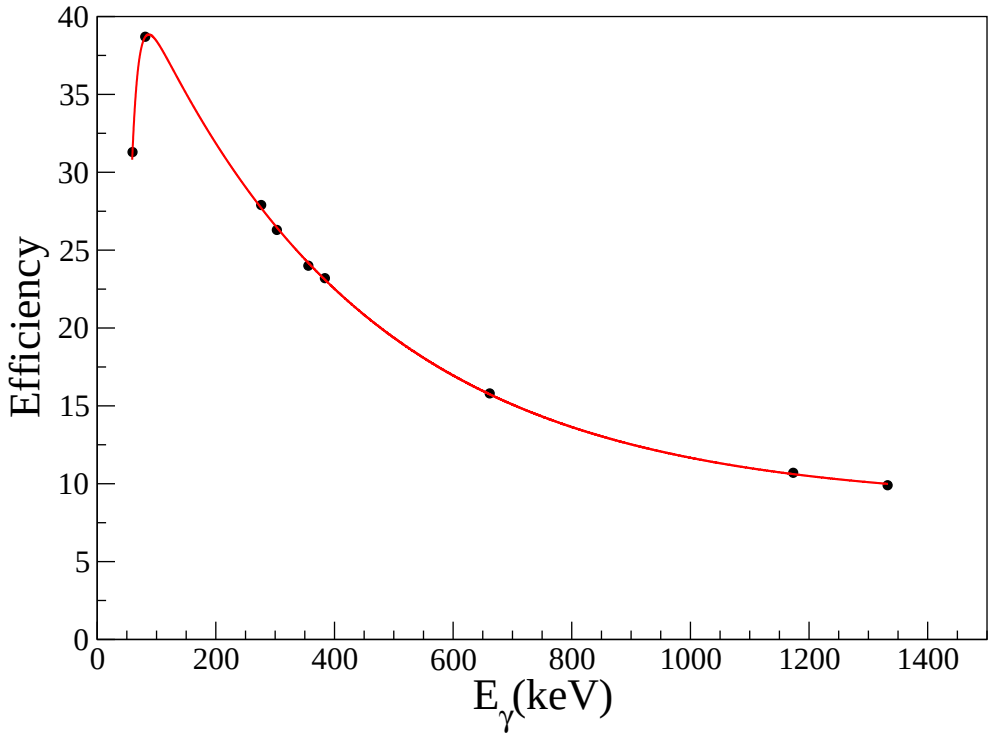

Figure 3.7: γ-ray photopeak efficiency response of the RISING array. This efficiency was measured using: ^{241}Am, ^{133}Ba, ^{137}Cs and ^{60}Co sources.

Photoelectric effect

The incident photon interacts with a bound atomic electron from the inner shells, usually the K and M. This results in the total absorption of the photon energy. The electron will be released from the atom with a kinetic energy (E_e) given by:

$$E_e = h\nu - E_b \tag{3.4}$$

where h is the Plank constant, ν is the photon electromagnetic wave frequency and E_b is the binding energy of the electron in its atom. After the emission of the electron, a vacancy in one of the bound shells is created. This vacancy is directly filled through the capture of a free electron or via rearrangement of the electrons from other shells of the atom. Therefore, a characteristic X-ray or Auger electron will be generated. The photoelectric effect is the dominant type of interaction for γ rays of relatively low energy. The probability of the photoelectric absorption per atom is given by [74]:

$$\tau \cong constant \times \frac{Z^n}{E_\gamma^{3.5}} \tag{3.5}$$

where Z is the atomic number and n varies between 4 and 5 depending on energy region of interest and E_γ is the photon energy.

Compton scattering

In Compton scattering process, the incident photon interacts with a quasi-free or weakly bound atomic electron. The photon transfers a portion of its energy to that electron and scatters the rest of the energy through continuous possible range of in various angles. The energy of the scattered photon ($E_{\gamma}{}'$) depends on the scattering angle and its given by the following equation [74]:

$$E_{\gamma}{}' = \frac{E_\gamma}{1 + \frac{E_\gamma}{m_\circ c^2}\,(1 - cos\theta)} \tag{3.6}$$

where E_γ is the energy of the incident photon, $m_\circ c^2$ is the rest mass energy of the electron and θ is the scatter angle of the γ ray. The probability of Compton scattering increases linearly with the atomic number (Z).

Pair production

If the energy of incident photon is greater than twice the rest mass energy of an electron (1.02 MeV), the pair production process is energetically possible. The probability of this process remains very low until the energy of the γ ray approaches several MeV, however this process is dominant for high energy γ rays ($E_\gamma > 5$ MeV). This interaction takes place between the incident photon and the coulomb field of a nucleus. The photon disappears and is replaced by an electron-positron pair [74]. The positron will subsequently annihilate after the slowing down in the absorbing material. Therefore two annihilation photons are normally produced with energy 511 keV as secondary product of this interaction.

3.4 The RISING Ge array

The aim of the RISING (Rare ISotope INvestigations at GSI) collaboration [75] is to use GeV range beams from the GSI/SIS synchrotron to study exotic nuclei produced through heavy-ion projectile fragmentation. This production technique coupled to a powerful germanium array using detectors from the decommissioned Euroball IV setup [76], with the use of the GSI fragment separator for the selection and identification of the produced ions, makes RISING a very powerful tool for the study of the internal structure of exotic nuclei [77]. In the configuration used in the current work, 15 germanium cluster detectors each with seven large volume crystals were placed in a high-efficiency arrangement. The detectors were positioned in three angular rings at angles of 51°, 90° and 129° to the primary beam axis, each containing seven cluster detectors (see figure 3.8). The measured photopeak γ-ray efficiency for the array in this geometry for sources placed in the centre of the focal plane was approximately 15% at 661 keV [78]. The energy signal was processed by full digital electronics using DGF-4C modules from the XIA company [78]. These modules have an internal clock with a 25 ns step which was used for the γ-ray timing signal from the germanium detectors. Two additional analogue timing signals were also produced by short-range (SR) and long-range (LR) TDCs. Figure 3.7 shows the measured γ-ray photopeak efficiency curve of the RISING array for DGF models. This efficiency was measured using: ^{241}Am, ^{133}Ba, ^{137}Cs and ^{60}Co point sources.

3.4.1 Active stopper

In the first phase of the RISING Stopped Beam experimental campaign a passive stopper was used for experiments [80]. In the experiments described in this thesis, the active stopper [39] was used for the first time in conjunction with the RISING γ-ray array. The ions of interest were implanted in the active stopper detector set-up. This consisted of a highly-pixelated Silicon detector stack which allows for correlation in time and space of the signal from the implanted ion and subsequent signals produced by β decays. The position of the implanted ion was correlated with its subsequent β decay (detected in the same pixel) and both implants and beta-decay events were measured using the active stopper.

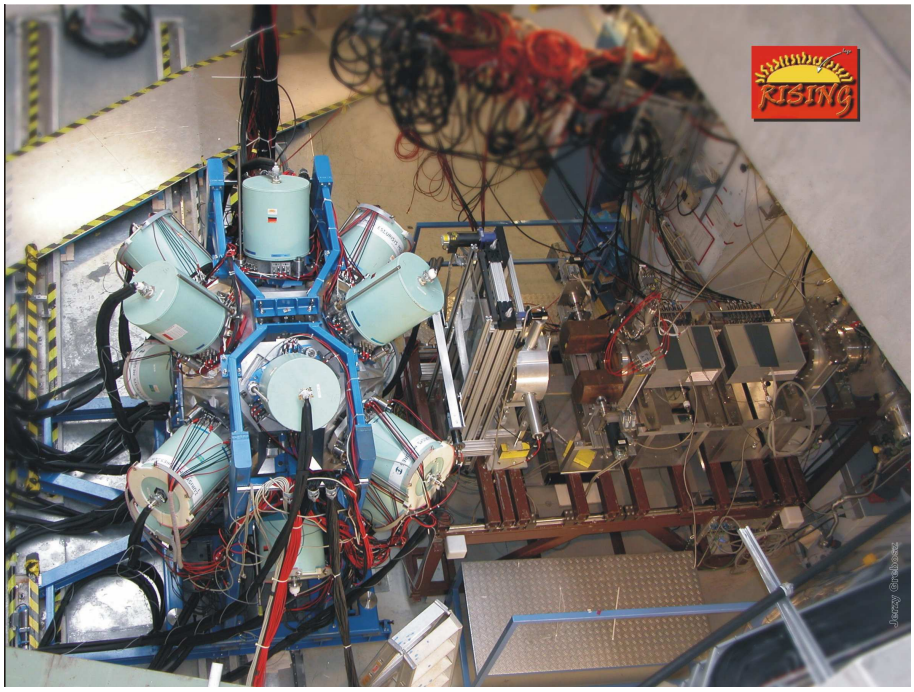

Figure 3.8: Photograph of the Stopped RISING array coupled to the RISING beam line at the focal plane of the FRS [79].

The RISING active stopper consists of up to 9 (Double Sided Silicon Strip Detectors) DSSSDs, each with 16 horizontal and vertical strips respectively, giving 256 pixels per DSSSD. Three DSSSDs were used in March 2007 experiment and six for the April 2008 one. Each DSSSD is 5 cm by 5 cm in overall dimension and 1 mm thick. These silicon detectors are *pn* junction diodes, operated with reverse bias voltage to form a sensitive region where free charge carriers can be generated by implanted radiation.

The motion of a carrier (either an electron or a hole), produced by ionization inside a silicon detector, can be described by [58]:

$$\nu = \mu(E).E \tag{3.7}$$

where ν is the carrier velocity, E is the electric field and μ is the charge mobility, which depends on the electric field. To add position sensitivity, these detectors are highly segmented into individual horizontal and vertical strips. The DSSSDs were used to determine the energy and position for both *(i)* the implanted secondary fragment of interest produced directly from the projectile fragmentation reactions and *(ii)* β-particles following the subsequent radioactive decay of the (often highly exotic) nucleus

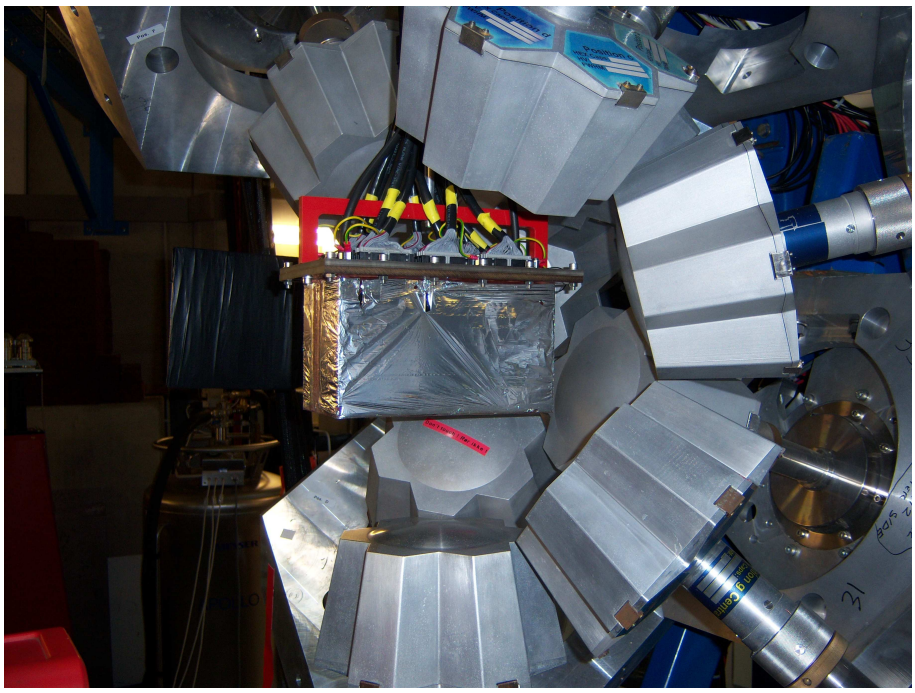

Figure 3.9: Photograph of the DSSSDs at the centre of the RISING array in its stopped beam configuration. The active stopper is housed in the light tight box in the middle of the opened RISING γ-ray array.

of interest and subsequent daughter decays.

The ultimate aim of the device is to correlate β-decay events with specific exotic radioactive mother nuclei on an event-by-event basis. Figures 3.9 and 3.10 show photographs of the bare DSSSDs and their position within a light-tight box placed in the middle of the RISING gamma-ray array. One of the challenges in designing the electronics for implantation and β-decay correlation experiments is the large difference between the two main types of events. A fragment implantation may deposit between 3 and 5 GeV of energy into the DSSSDs, while a β particle (typically a few 100 keV in a strip/pixel) deposits less that 4 MeV [58].

This issue was solved by using a preamplifier for the DSSSD energy signals, which was linear in the low-energy response range followed by a logarithmic response at higher gains. Semi-logarithmic preamplifiers were used which provided a linear amplification up to 10 MeV and logarithmic amplification for the 10 MeV$\rightarrow$3 GeV range [39]. The linear part allowed for both measurements of β^- and internal conversion electrons [81] and in principle, also spectroscopy of delayed charged particle decays.

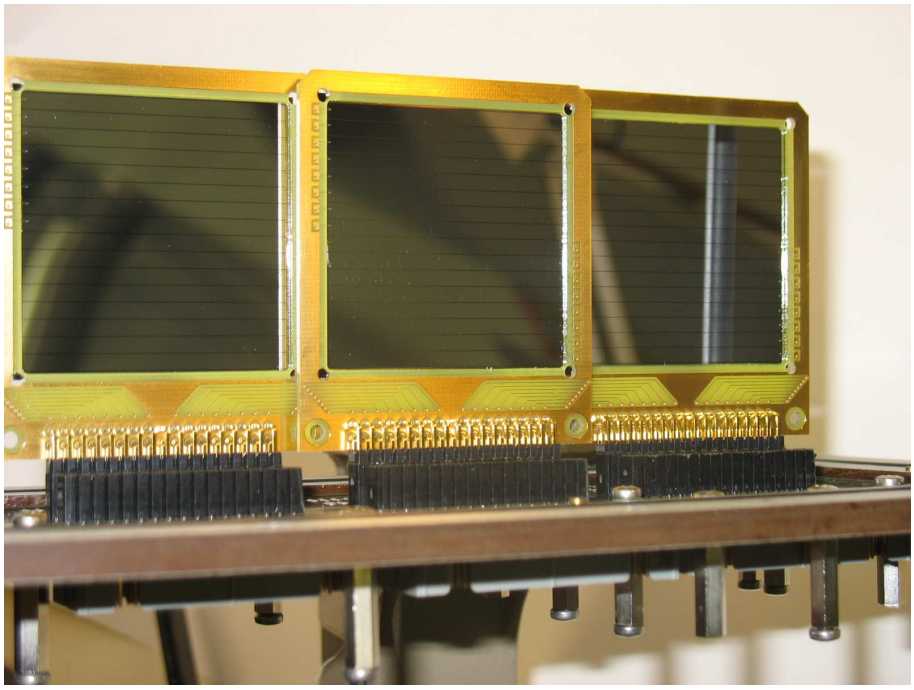

Figure 3.10: Photograph of the bare DSSSDs used in the RISING active stopper in their holder with the light-tight outer box removed. (Note this was not the final geometry used for the three DSSSDs in the current work).

This range was calibrated using an open, internal conversion electron ^{207}Bi source, yielding an energy resolution of FWHM=20 keV and a minimum detection threshold of approximately 150 keV [39]. The logarithmic part of the DSSSD output range allowed for the determination of the implantation position in an individual pixel (i.e. the pixel with maximum energy output compared to its neighbours) and was calibrated for energy response using a pulser [39]. Scintillation detectors were placed both in front of and behind the DSSSDs, allowing off-line suppression of most of those fragments which were destroyed in the slowing down process. Further details on the response of the semi-logarithmic pre-amplifier can be found in Ref. [71].

Chapter 4

β^--decay of ^{194}Re $\longrightarrow$ ^{194}Os

4.1 Introduction

In this chapter, the production and structural investigation of neutron-rich isotopes of the elements Rhenium (Re, Z=75) and Osmium (Os, Z=76) is presented. These nuclei were produced in highly energetic projectile fragmentation reactions and identified using the FRS at the GSI laboratory in Darmstadt, Germany. This experiment was performed in March 2007. The decays of these nuclei have been studied following both beta and isomer-delayed γ-ray spectroscopy using the RISING γ-ray spectrometer. The β-delayed studies utilised the RISING active stopper which enabled positional and temporal correlations to be determined between the implantation of a specific exotic isotope and its subsequent β decay. The β^--decay lifetimes of three low-lying states in ^{194}Re isotope are measured. Decays from states populated in the daughter nucleus, ^{194}Os, following β-decay are also identified.

4.2 Experimental details

The nuclei of interest were produced following the interaction of a ^{208}Pb primary beam at 1 GeV per nucleon from the SIS-18 synchrotron at GSI, with a ^{9}Be target of thickness 2.54 g/cm^2 located at the entrance of the FRS. The typical time length per ion spill was about 1 second. The FRS was operated in monochromatic mode using an aluminum wedge-shaped degrader [38] at the intermediate focal plane (S2). In this experiment the active stopper consisted of three 5 cm $\times$ 5 cm DSSSDs, each

Table 4.1: Experimental parameters details for the FRS setting, centred on the transmissions of ^{190}Ta, ^{192}Ta and ^{194}Re respectively.

Setting	Bρ_1 (Tm)	Bρ_2 (Tm)	S2 degrader Thickness (mg/cm^2)	S4 degrader Thickness (mg/cm^2)	Beam Intensity (ion/spill)	Spill Repetition (s)	Total Time of Collection
^{190}Ta	13.08	9.59	5050	3320	10^8	20	62 hours
^{192}Ta	13.23	9.75	5050	3450	10^9	15	66 hours
^{194}Re	13.05	9.45	5050	3040	4×10^8	7	6 hours

with 16 individual strips on the front and back faces, with each strip separation of 1 mm. This was used to measure the position of the implanted ions and correlate it with its subsequent β decay detected in the same or neighbouring pixels of the DSSSDs. Figure 4.1 shows a schematic of the detector configuration at the final focal plane of the FRS at GSI which is used in this work. In the active stopper configuration the right hand side DSSSD was placed behind the central DSSSD and used as a veto detector to identify those ions not stopped in the first DSSSD. Following the initial calibration setup for the experiment it was noticed that most of the ions were implanted in the central and left DSSSDs and almost nothing was implanted on the right hand side DSSSD position.

To maximise the number of fully stripped ($q = Z$) nuclei passing through the FRS, niobium foils of 223 mg/cm^2 and 108 mg/cm^2 thicknesses respectively were placed both after the target and the degrader at S2. Three FRS settings are discussed in the current work, namely those centred on the transmission of fully stripped ^{190}Ta, ^{192}Ta and ^{194}Re. Table 4.1 gives a summary of the experimental details of these settings. Note, that unless stated otherwise, the results shown this chapter are from the summed data of the three settings outlined in Table 4.1.

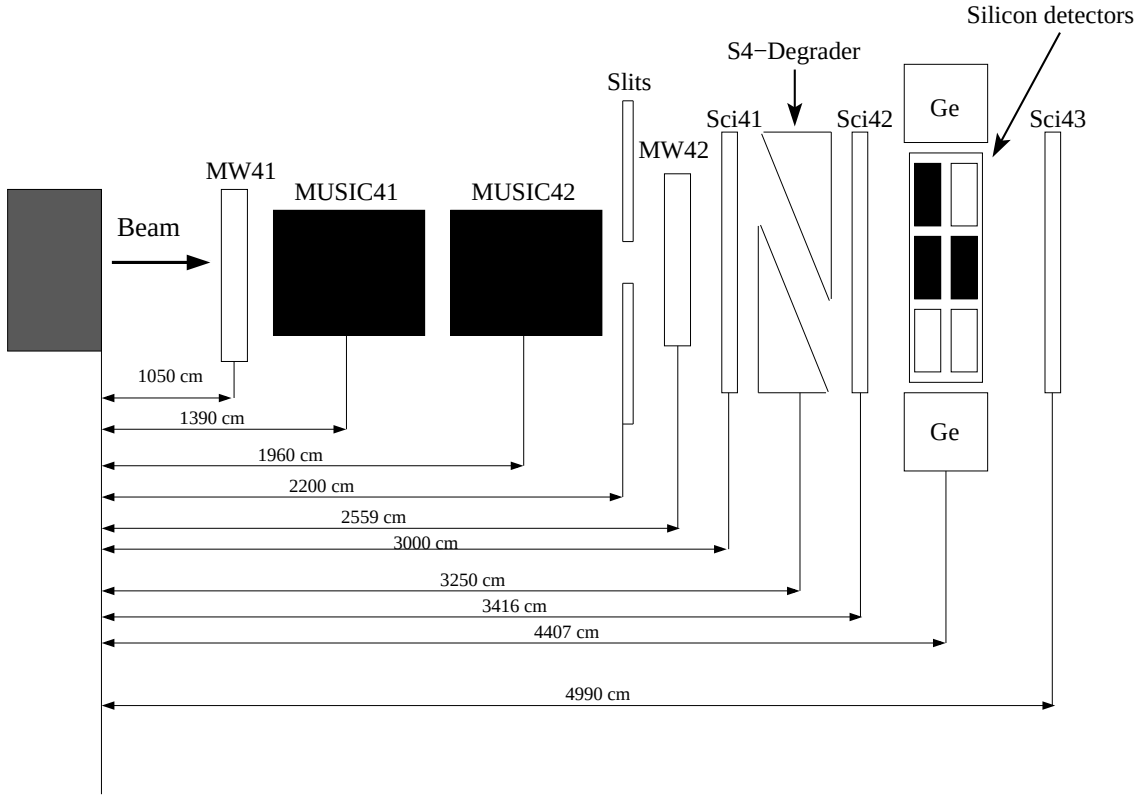

Figure 4.1: Schematic of the detector configuration at the final focal plane of the FRS used in the present work, for the March 2007 experiment. Three of the possible six positions (black boxes) in the active stopper were occupied by DSSSDs in this particular experiment. MW= MultiWire detectors; Sci= Scintillator detectors; MUSIC= MUlti Sampling Ionising Chamber detectors. The secondary ions were transmitted from left to right on this schematic. The label "4"indicates that the detectors are placed at the final focal plane of the FRS.

4.3 Identification of the reaction products

4.3.1 Selection of projectile fragments

A cocktail of the secondary beams was created following the interaction of the ^{208}Pb beam with the ^{9}Be target at the entrance of the FRS. The products from this reaction can be classified as either fission fragments or projectile fragments. Those fragments which were transmitted to the final focal plane are shown in figure 4.2 using the energy loss in the MUSIC 42 detectors. The main aim of the present work was to study the projectile fragmentation reaction products, therefore the fission fragments

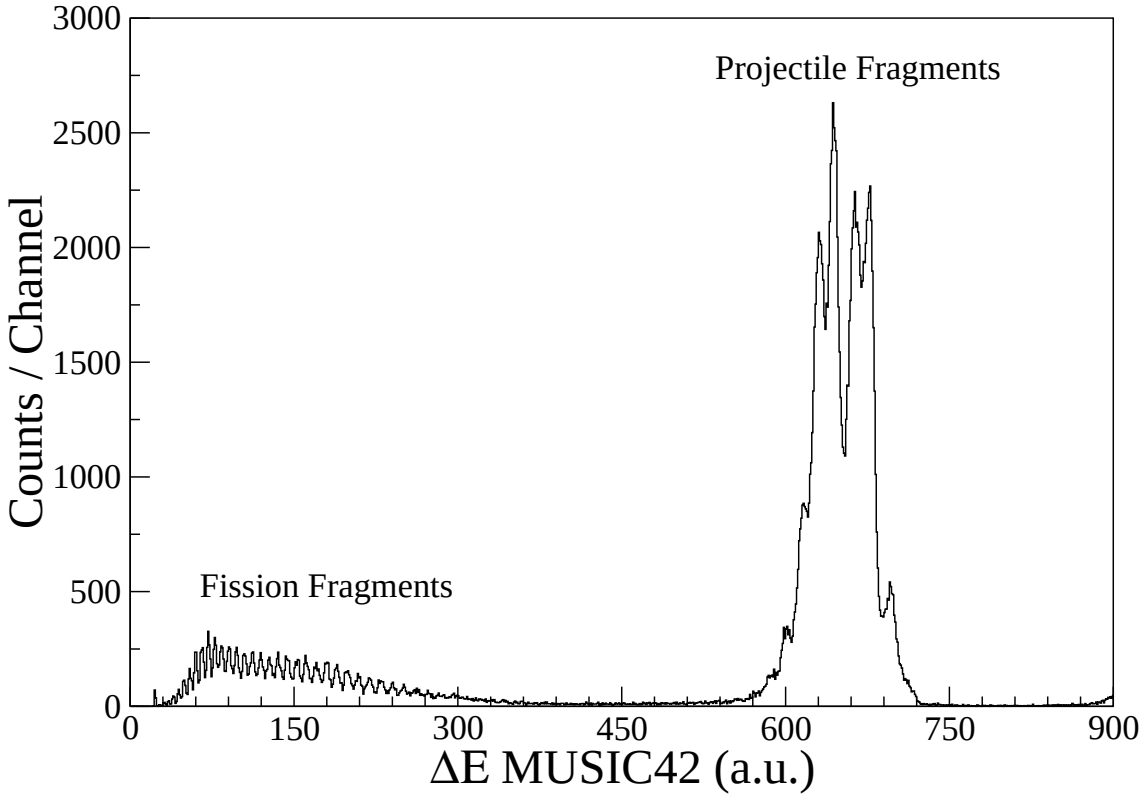

Figure 4.2: Energy loss measurements in the MUSIC 42 detector which shows the fission and projectile fragments for ^{194}Re centred setting.

were excluded from the off-line analysis. For the final particle identification procedure, offline software conditions were applied to both MW41 and MW42 detectors to ensure proper corrections and selection of projectile fragments.

4.3.2 Reactions in scintillation detector Sci42

The charge state of the ions can change through the exchange of either one or more electrons when the ions pass through material, such as the degrader at the S4. By measuring the energy of the ions before and after the degrader at the S4 it is possible to observe whether these interactions of the ions take place at this degrader. Therefore, the Scintillator detector (Sci42) was used to measure the ions after the S4 degrader (i.e. to check that there were no nuclear reactions of the ions in the S4 degrader and in the Sci42), as well as to slow down the ions before reaching the active stopper. Figure 4.3 shows the spectrum of the energy loss in MUSIC41 detector versus the energy loss in the Sci42 detector for the ^{190}Ta, ^{192}Ta and ^{194}Re centred settings. In this figure,

the red line surrounds those events which have no nuclear reaction in the S4 degrader. These events were used in the full analysis, with the other events removed from the off-line analysis.

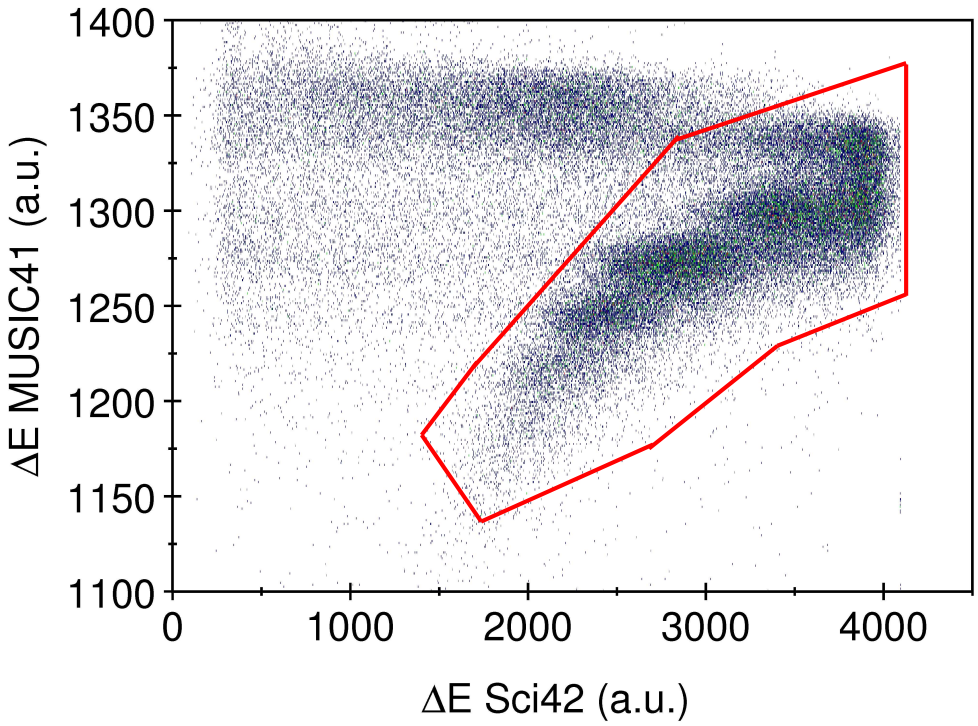

Figure 4.3: Energy loss in the MUSIC41 detector versus the energy loss in the Sci42 detector for the summed data. The red line surrounds those projectile fragmentation ions associated with "no nuclear reaction"in the S4 degrader.

4.3.3 The Veto: Scintillation detector Sci43

The final stage for removing the unwanted events from the off-line analysis was performed by using the Scintillation detector (Sci43), which is also called the *veto* detector. If the fragment does not stop in the active stopper, it should appear in the *veto* detector. This allowed the removal of these fragments from the off-line analysis. The energy loss of the *veto* detector for summed data from the ^{190}Ta, ^{192}Ta and ^{194}Re centred settings is shown in figure 4.4. The events after the red line were removed from the final off-line analysed data. The spike at the beginning of the spectrum arises from

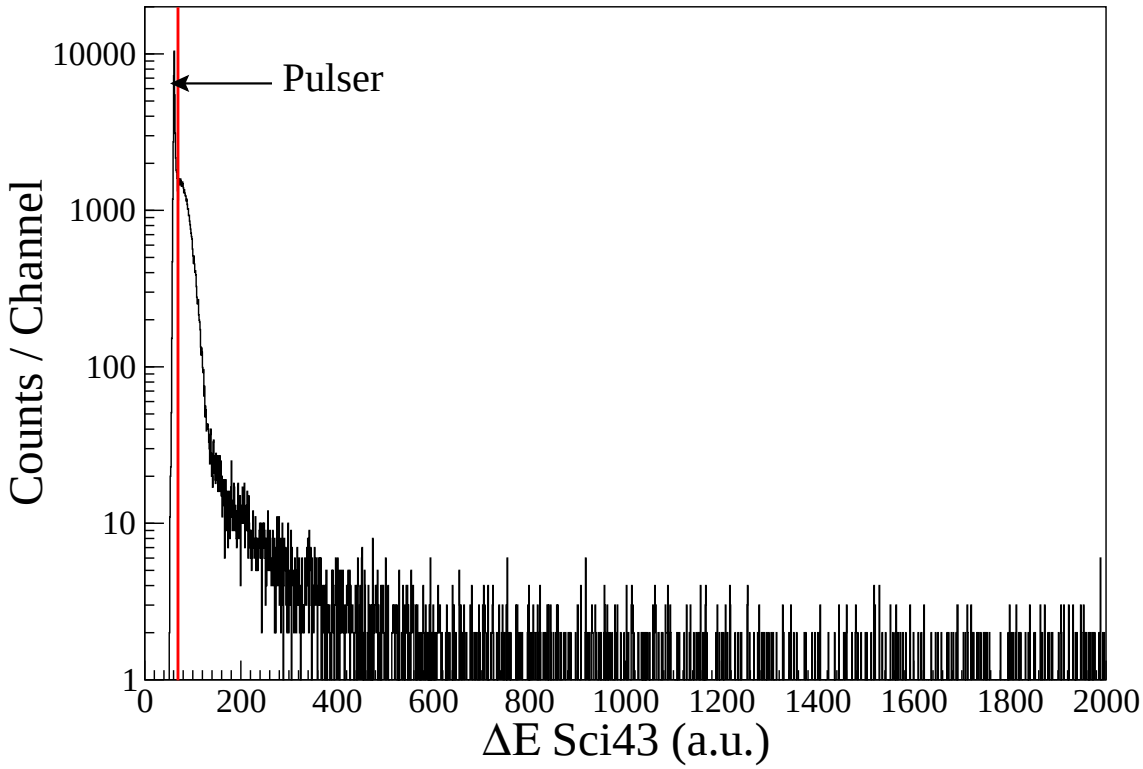

Figure 4.4: Energy loss in the *veto* Scintillator Sci43 for the ^{190}Ta, ^{192}Ta and ^{194}Re centred settings. Those events after the red line were removed from the subsequent off-line analysis.

a pulser which is connected to the detector.

4.4 Particle identification

4.4.1 Charge state identification

The particle identifications in the current work were made on event-by-event basis. There are two stages for the particle identification of the heavy ions in this type of study. The first step is a selection on in-flight changes in charge state. The FRS selection is dependent on the charge-changing properties of each ion as it passes through the detector and degrader materials of the FRS. "Fully stripped" ions correspond to no charge state change between the first and second sections of the FRS ($\triangle q = 0$), while "hydrogen-like" ions correspond to the pick-up of one electron at the intermediate focal plane ($\triangle q = -1$), and "helium-like" ions correspond to the pick-up of two electrons

Table 4.2: The total numbers of the fully stripped nuclei transmitted from the summed data for the ^{190}Ta, ^{192}Ta and ^{194}Re centred settings.

Number	Nucleus	Number of Nuclei
1	$^{186}_{72}$Hf	1307
2	$^{187}_{72}$Hf	2249
3	$^{188}_{72}$Hf	2088
4	$^{189}_{72}$Hf	927
5	$^{188}_{73}$Ta	2413
6	$^{189}_{73}$Ta	5741
7	$^{190}_{73}$Ta	3537
8	$^{191}_{73}$Ta	1836
9	$^{190}_{74}$W	2568
10	$^{191}_{74}$W	11098
11	$^{192}_{74}$W	10647
12	$^{193}_{74}$W	6515
13	$^{192}_{75}$Re	1280
14	$^{193}_{75}$Re	13013
15	$^{194}_{75}$Re	10353
16	$^{195}_{75}$Re	10238
17	$^{196}_{75}$Re	3122
18	$^{195}_{75}$Os	1451
19	$^{196}_{75}$Os	5059
20	$^{197}_{75}$Os	6404
21	$^{198}_{75}$Os	5798

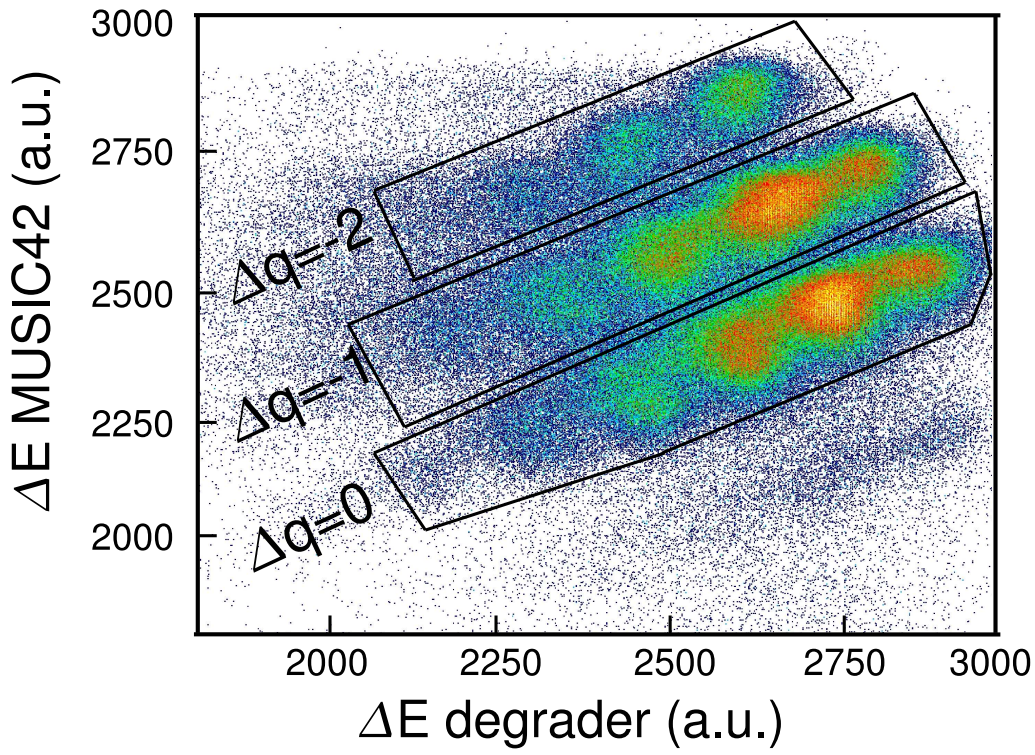

Figure 4.5: Charge state selection plot of nuclei centred on the transmission of fully stripped ions from summed data, using monochromatic mode (see text for details).

($\triangle q = -2$). Charge state selection was achieved by the using the position of plastic scintillators at the intermediate and final focal plane of the FRS to define the velocities and magnetic rigidities of the secondary ions. The difference in magnetic rigidity between the first and second stage of the fragment separator can be used to estimate the energy loss of the ion through the degrader. This information together with the energy loss of the ions as measured at the final focus plane using the MUSIC detectors allows a degree of charge state discrimination. This technique is of particular use in the case of heavy neutron-rich nuclei (see Ref. [82] for more details). For the separation of different charge states, it is necessary to derive the dependency of A/q and $B\rho$ on each other. The magnetic force on a particle with charge q moving with velocity v is given in equation 4.1, where B is the field strength.

$$\overrightarrow{F} = q(\overrightarrow{v} \times \overrightarrow{B}) \tag{4.1}$$

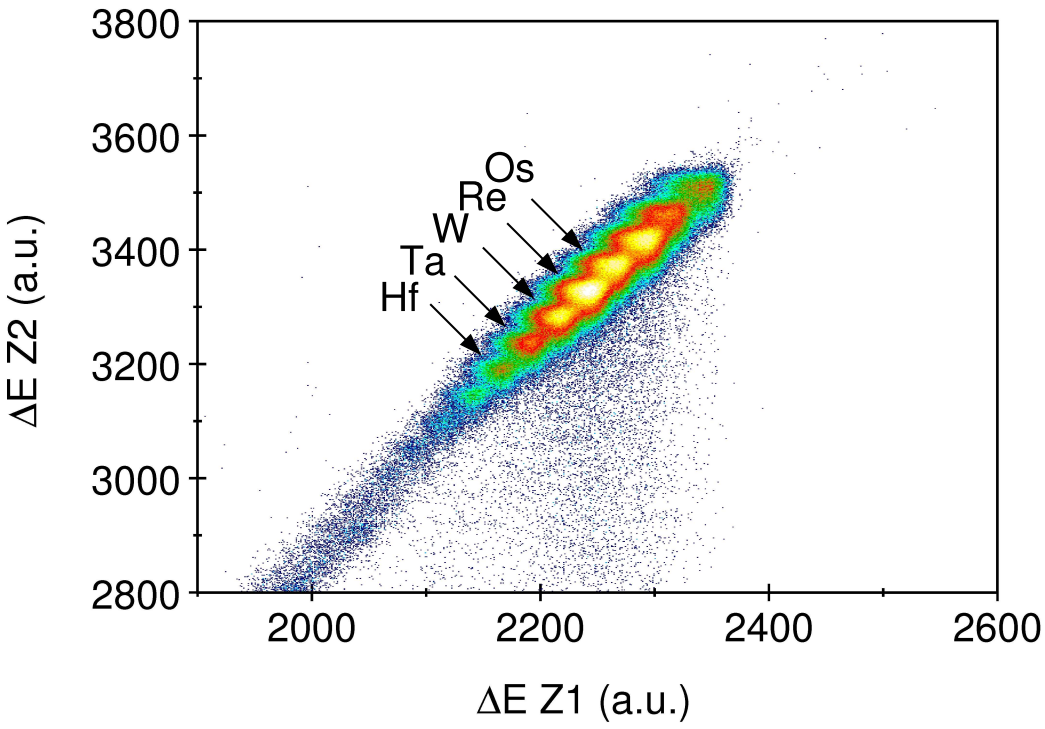

Figure 4.6: Energy loss in MUSIC 42 versus the energy loss in MUSIC 41 plot for the summed data.

The magnitude of the centripetal force on a particle in a circular motion is given by equation 4.2,

$$F = \frac{mv^2}{r} \tag{4.2}$$

where $r = \rho$ is the magnetic bending radius (which can be measured directly); v is the velocity, $v = c\beta$; γ is equal to $\sqrt{1/(1-\beta^2)}$; p is the linear momentum (which can be written in terms of the fragment mass (m) and the velocity).

The mass is rewritten in terms of the atomic number A [83], then [1]

$$B\rho = \frac{A}{Q}\beta\gamma\frac{uc}{e} \tag{4.3}$$

According to the charge state calculations using the GLOBAL code [84], 95.4% of

[1] see Appendix A for derivation

the ^{194}Re ions were fully stripped exiting the target and 83.6% after the intermediate focal plane. The number of the implanted nuclei of the combinations of ^{190}Ta, ^{192}Ta and ^{194}Re centred setting for the fully stripped ($\triangle q = 0$) ions is given in Table 4.2. For the FRS setting centred on the transmission of ^{190}Ta, ^{192}Ta and ^{194}Re, the identification of the three charge state groups is show in figure 4.5.

4.4.2 Identification of atomic number (Z)

The ions lose energy as they pass through various detectors, which can be used to infer the atomic number (Z) of the ions. The energy loss in the MUSIC detectors were used to measure the electronic number of the ions. The Bethe-Block formula [74] can be used to estimate the energy loss of the ions in a given absorber, using the following equation:

$$\frac{-dE}{dx} = \frac{4\pi e^4 z^2}{m_\circ v^2} NB \tag{4.4}$$

where

$$B = Z\left[ln\frac{2m_\circ v^2}{I} - ln\left(1 - \frac{v^2}{c^2}\right) - \frac{v^2}{c^2}\right] \tag{4.5}$$

where v and z are the velocity and the charge of the primary particle, N and Z are the number density and atomic number of the absorber atoms, $m_\circ$ is the electron rest mass and e is the electronic charge. The parameter I represents the average excitation and ionization potential of the absorber. For a beam of charged particles with the same velocity interacting with a specific target, the only factor that may change the loss of energy in Eq. (4.4) is z^2 [74]. Therefore, the particles with the greatest charge will have the largest specific energy loss [74]. The energy loss in the MUSIC42 detector versus the energy loss in the MUSIC41 detector for the ^{190}Ta, ^{192}Ta and ^{194}Re centred settings is show in figure 4.6.

4.4.3 Particle identification plot

One is now able to analyse each group of charge states differences separately. The mass-to-charge ratio of the ions, (A/q), was determined from their Time Of Flight (TOF) and magnetic rigidity measurements in the second part of the FRS. The TOF in the second stage of FRS was determined by measuring the time difference of the ions

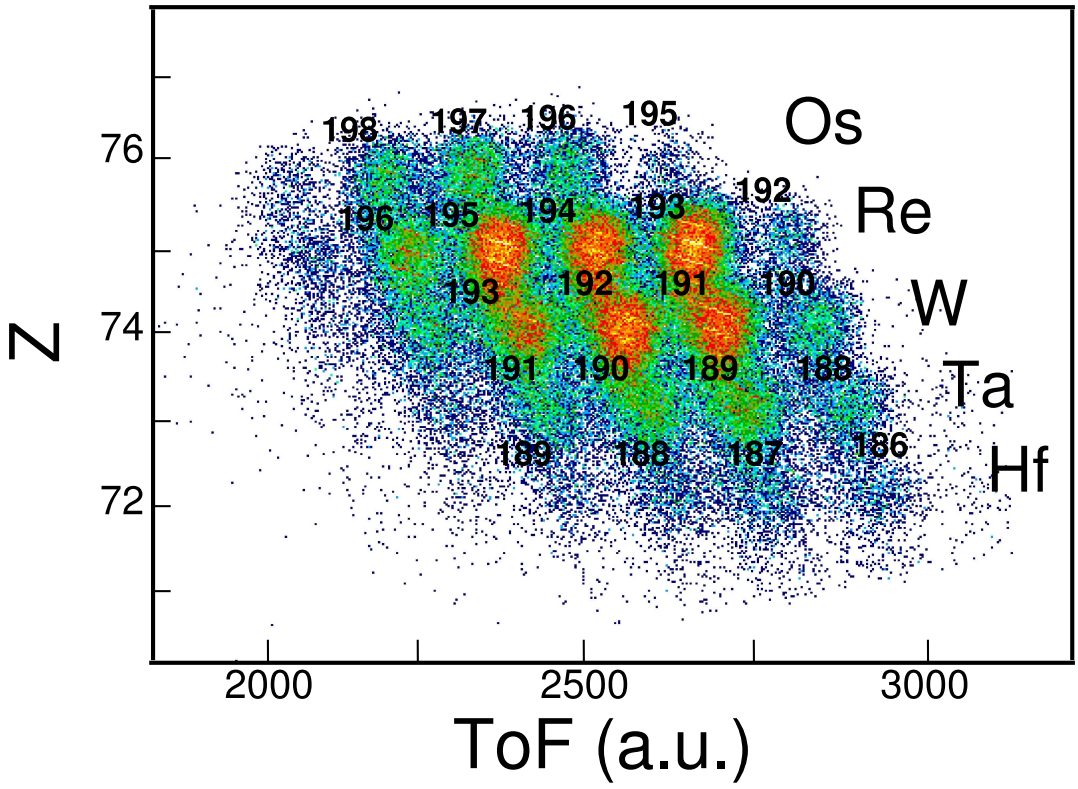

Figure 4.7: Particle identification plot for the summed data from the ^{190}Ta, ^{192}Ta and ^{194}Re centred settings for fully stripped ions ($\triangle q = 0$).

as they passed between two plastic scintillators which were placed *(i)* before the S2 degrader and *(ii)* at the final focal plane of the FRS. The change of the magnetic rigidity of ions was measured before and after they passed through the degrader at S2 which was used to obtain information on any change in charge state. The energy deposition of the identified fragments, which gives information on the atomic number (Z), was measured as they passed through two MUlti Sampling Ionization Chambers (MUSIC). By determining A/q, the charge state, the position at the final focal plane and Z, an unambiguous event-by-event identification can be obtained. Further details of the particle identification technique are given in Ref. [14, 80, 81, 85]. The transmitted ions were slowed down in a variable thickness aluminum degrader at S4 and finally implanted into the active stopper. Figure 4.7 represent the particle identification plot for the summed data assuming fully stripped ions ($\triangle q = 0$). In this figure, the atomic number, Z which is calculated from the energy loss of the ions in the MUSIC detector,

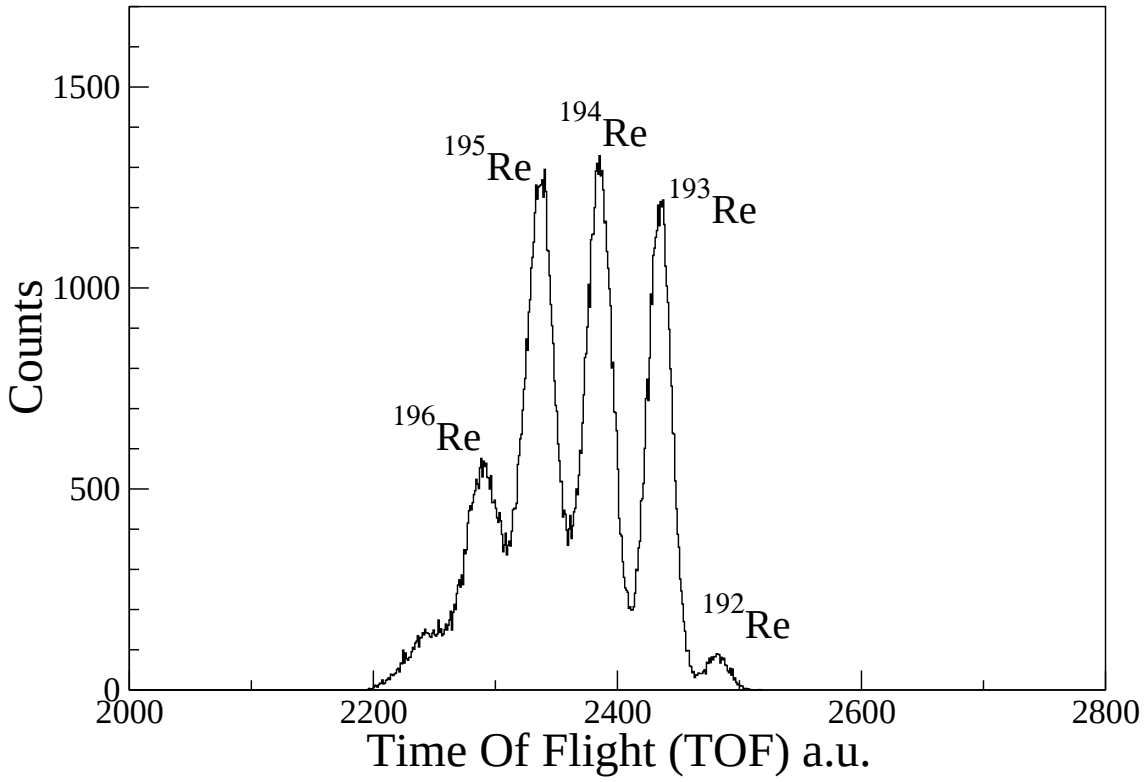

Figure 4.8: Time Of Flight (TOF) projection for the Re isotopes identified from the summed data from the three settings, assuming fully stripped ions ($\triangle q = 0$).

is plotted versus the measured time of flight TOF in the second half of the FRS, which is related via the magnetic rigidity to the mass-over-charge ratio of the transmitted ions. Figure 4.8 shows a projection of the particle identification plot onto the *x-axis* (TOF) for the Re isotopes.

4.5 Particle implantations and beta decays

The March 2007 experiment was the first time the RISING active stopper [39] was used in conjunction with RISING γ-ray array [77, 78]. γ-ray decays were observed and correlated with the implanted ions on an event by event basis such that transitions from both internal (isomeric states) decays and also the subsequent β decay of the implanted ions could be measured. The isomeric states were produced by the fragmentation interaction of the initial beam with the target. Ideally, isomeric products should have a lifetime similar to or longer than the time required to traverse the length of the

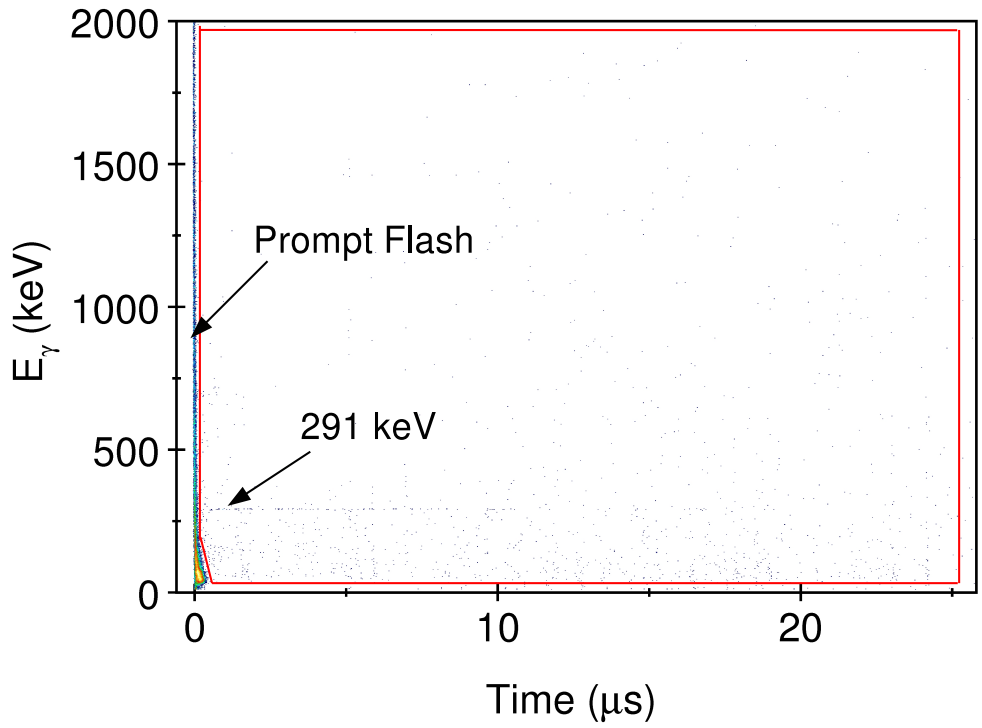

Figure 4.9: 2-D matrix γ-ray energy versus detection time after implantation of fully stripped ^{188}Ta ions. Note the presence of the line associated with the previously identified isomeric decay in this nucleus [7].

FRS to reach the active stopper. Shorter lifetimes of isomeric decay products have been measured due to suppression of the electron conversion decay branch for highly stripped ions (i.e. the in-flight ionic half life is substantially longer than the neutral atom half life) [7]. The implanted mother nuclei decay to the daughter nuclei via β-particle emission which can be followed by γ-ray (or internal conversion) decay if the β decay populates excited states in the daughter nucleus [86]. Two triggers were used to detect the γ ray in the RISING array, namely the implantation and decay triggers.

A signal is given to the logical electronics of the RISING Ge array to be opened for up to 400 μs if the selected ions passes through the Scintillator detector, (Sci41), to allow for the measurement of γ rays decaying from isomeric states in the mother nuclei. Then, the RISING Ge array data acquisition was closed until receiving either *(i)* another signal from the Sci41 trigger or *(ii)* a signal from the decay trigger of the

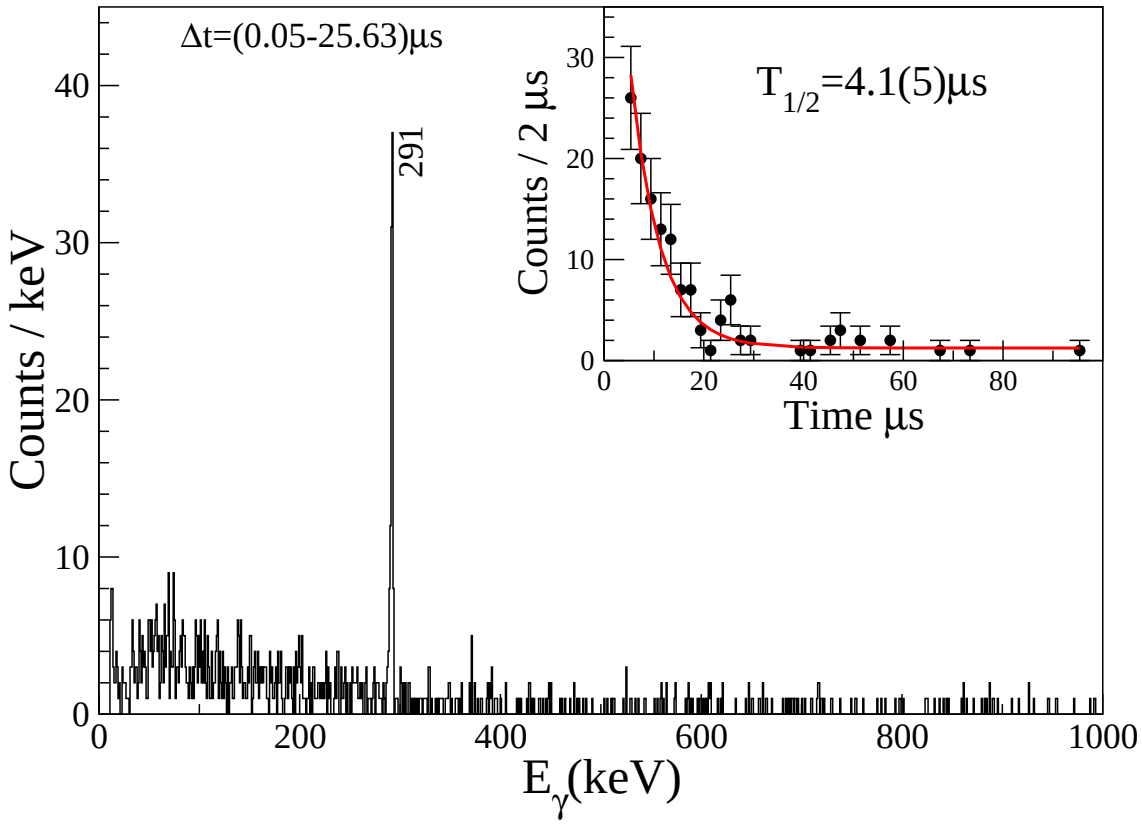

Figure 4.10: The projection of γ-ray energies of the ^{188}Ta nuclei for a time range $\Delta t = (0.05 - 25.63)\mu$s following the implantation in the active stopper. The inset figure is the decay time curve associated with the isomeric decay in ^{188}Ta [7].

active stopper. The decay trigger provided a signal to the RISING Ge array to be opened only if there were no ions crossing the Sci41 detector, and the energy of the signal should be above a defined lower threshold. In this case, the RISING Ge array was again opened for up to 400 μs to detect the γ rays of the populated isomeric states following β^--decay in the daughter nucleus.

4.5.1 Identification of decays from isomeric states

The secondary ions were separated, selected and identified preliminarily according to their A/q values. The ions were implanted in the three DSSSDs. The identification plot was confirmed by correlating ions with decays from previously reported isomers [7, 87, 88, 89]. This was achieved by making two-dimensional matrices of the detected γ-ray energies versus the measurement of their decay time relative to the ion implantation.

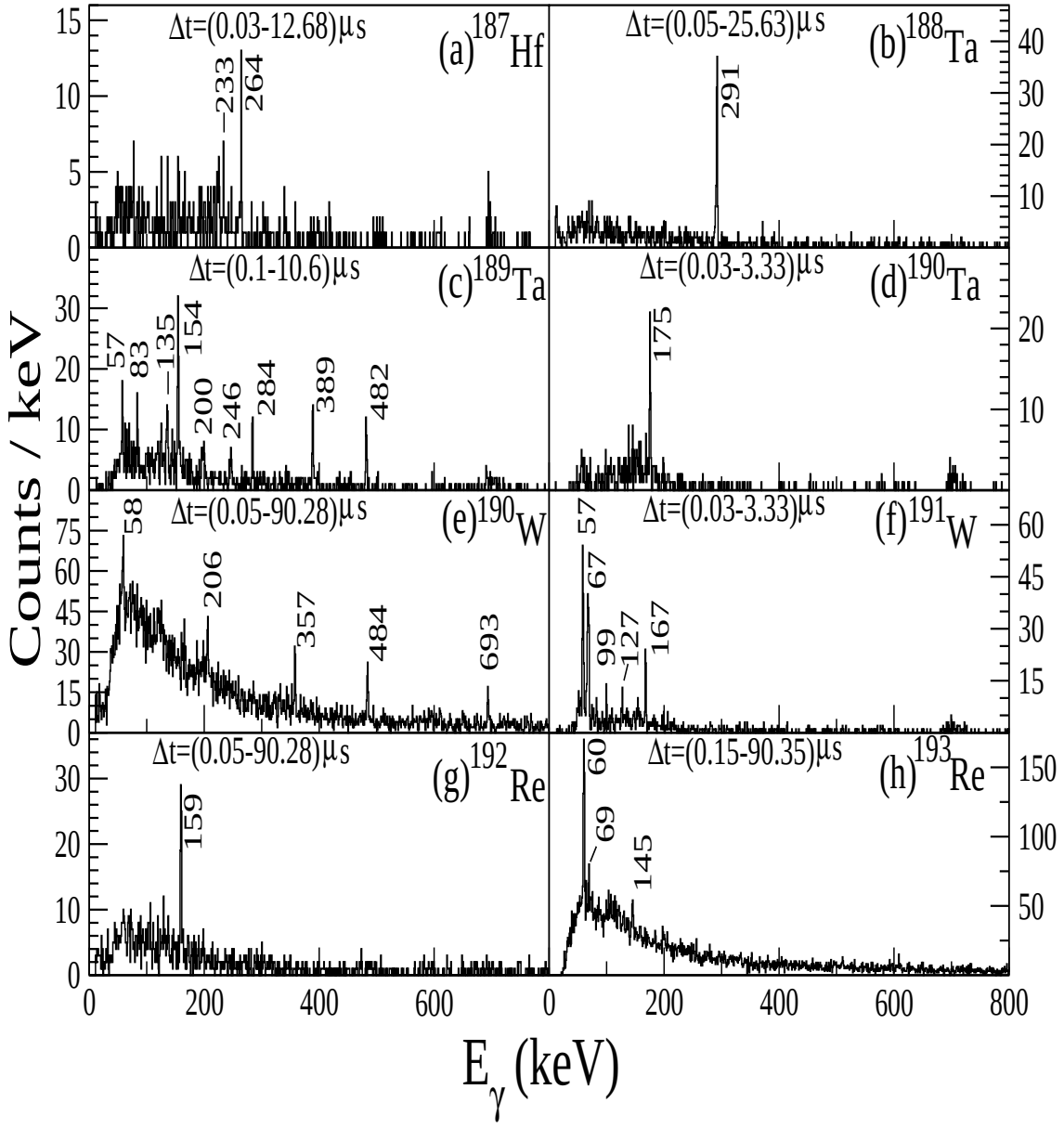

Figure 4.11: γ-ray spectra from isomeric decays in **(a)** ^{187}Hf for a time range $\Delta t = (0.03-12.68)\mu$s, **(b)** ^{188}Ta for a time range $\Delta t = (0.05-25.63)\mu$s, **(c)** ^{189}Ta for a time range $\Delta t = (0.1-10.6)\mu$s, **(d)** ^{190}Ta for a time range $\Delta t = (0.03-3.33)\mu$s, **(e)** ^{190}W for a time range $\Delta t = (0.05-90.28)\mu$s, **(f)** ^{191}W for a time range $\Delta t = (0.03-3.33)\mu$s, **(g)** ^{192}Re for a time range $\Delta t = (0.05-90.28)\mu$s and **(h)** ^{192}Re for a time range $\Delta t = (0.15-90.35)\mu$s, from the present work [7, 87].

Figure 4.9 shows this matrix for isomeric decays associated with fully stripped ^{188}Ta ions. The isomeric decay was previously reported in Ref. [7] and reported subsequently in Ref. [87]. The prompt flash is the first observable feature in this matrix and is mainly associated with *Bremsstrahlung radiation* which is produced by the slowing down of the implanted ions in the active stopper at the final focal plane of the FRS. The isomeric, discrete γ-ray transitions can be identified as horizontal lines extending (in time) to the right as demonstrated in figure 4.9. The delayed γ rays are of specific interest and therefore a condition gate was applied to this matrix (shown by the red polygon in figure 4.9), in order to identify delayed γ rays following the prompt flash. The prompt flash reduces the effective efficiency of detecting the γ rays for a period of time depending on the γ-ray multiplicity of the flash [90]. Figure 4.10 shows the energy projection of ^{188}Ta in which the 291 keV γ ray transition from the previously reported isomeric decay in the this nucleus is clearly identified [7].

4.5.2 Confirming the identification

The particle identification procedure was confirmed by observation of decay transitions from previously reported isomers [7] in ^{188}Ta, ^{190}W, ^{192}Re and ^{193}Re. The current work also shows evidence for the isomeric decays in ^{187}Hf, ^{189,190}Ta and ^{191}W which have beeb reported in Ref. [87]. The particle identification procedure provided an independent validation for the γ-ray energy and timing setups. Figure 4.11 shows the final γ-ray energy spectra corresponding to decays from isomeric states which are identified in the summed data from the ^{190}Ta, ^{192}Ta and ^{194}Re centred setting, for fully stripped ions. Details of the specific decays are presented in the section below [2]:

^{187}Hf

The delayed γ-ray spectrum associated with ^{187}Hf nuclei from the present work is displayed in figure 4.11 *(a)* showing delayed γ-ray energies of 233 and 264 keV. Table 4.3 listed the measured γ-ray energies and relative γ-ray intensities of ^{187}Hf nuclei for fully stripped ions from the current work.

[2] These data (although analysed separately) are reported in Ref. [87]

Table 4.3: The measured γ-ray energies and relative intensities of nuclei from the summed data from the ^{190}Ta, ^{192}Ta and ^{194}Re centred settings.

Nucleus	γ-ray energy (keV)	Counts	ε_γ^{ABS}	N_γ	$\triangle$t
^{187}Hf	233.0(4)	7(3)	0.25	27(12)	(0.03-12.68)μs
	263.9(2)	17(4)	0.23	73(17)	
^{188}Ta	291.2(1)	95(10)	0.23	405(59)	(0.05-25.63)μs
^{189}Ta	57.2(2)	28(7)	0.24	117(31)	(0.1-10.6)μs
	83.2(2)	21(6)	0.30	69(21)	
	135.1(3)	29(7)	0.30	95(25)	
	154.2(2)	72(9)	0.29	243(39)	
	200.0(2)	30(5)	0.27	110(21)	
	245.8(6)	17(5)	0.25	68(21)	
	283.5(2)	22(5)	0.23	93(23)	
	388.5(2)	35(6)	0.20	175(35)	
	481.5(2)	28(6)	0.17	160(38)	
^{190}Ta	175.1(2)	45(7)	0.28	158(29)	(0.03-3.33)μs
^{190}W	58.4(6)	59(20)	0.24	246(87)	(0.05-90.28)μs
	205.4(3)	62(12)	0.27	230(50)	
	357.4(2)	56(9)	0.21	265(50)	
	483.7(2)	59(9)	0.17	337(62)	
	693.2(3)	37(7)	0.13	274(59)	
^{191}W	58.3(1)	135(13)	0.24	563(78)	(0.03-3.33)μs
	67.2(2)	150(13)	0.27	545(72)	
	82.0(3)	11(4)	0.30	36(14)	
	99.7(7)	17(9)	0.31	54(29)	
	126.7(1)	12(5)	0.30	39(17)	
	167.4(1)	49(7)	0.29	169(30)	
^{192}Re	159.1(1)	76(9)	0.29	259(40)	(0.05-90.28)μs
^{193}Re	60.0(8)	375(24)	0.25	1488(177)	(0.15-90.35)μs
	68.7(2)	58(13)	0.28	207(51)	
	144.7(3)	122(17)	0.30	405(70)	

^{188}Ta

The delayed γ ray spectrum associated with ^{188}Ta nuclei is shown in figure 4.11 *(b)*. The observed delayed γ-ray energy with 291 keV is in agreement with previously reported work on this nucleus by Caamaño *et al*. [7]. The measured half-life is $T_{1/2}$=4.1(5) μs, see the inset to figure 4.10. Table 4.3 shows the energies and relative intensities of ^{188}Ta nuclei for fully stripped ions of the summed data.

^{189}Ta

Figure 4.11 *(c)* shows the delayed γ-ray spectrum associated with ^{189}Ta nuclei for fully stripped ions from the summed data. Nine γ-ray transitions with energies 57, 83, 135, 154, 200, 246, 284, 389 and 482 keV together with the characteristic Ta K_α X ray (with energy 57 keV) are clearly identified. Only transitions with energies 154, 284, 389 and 482 keV are in agreement with previously reported work on this nucleus by Steer *et al*. [88]. The experimental energies and relative intensities of ^{188}Ta nuclei for fully stripped ions from the summed data is listed in Table 4.3.

^{190}Ta

A single γ-ray transition of energy 175 keV is identified in figure 4.11 *(d)* which shows the delayed γ-ray spectrum associated with ^{190}Ta nuclei for fully stripped ions from the summed data. Table 4.3 shows the energy and relative intensity of ^{190}Ta nuclei for fully stripped ions for the combination of ^{190}Ta, ^{192}Ta and ^{194}Re centred settings.

^{190}W

Figure 4.11 *(e)* shows the delayed γ-ray spectrum associated with ^{190}W nuclei for fully stripped ions for the summed data. Four γ-ray transitions with energies 206, 357, 484 and 693 keV together with the characteristic W K_α X ray (with energy 58 keV) are clearly identified. These transitions are in agreement with previously reported work on this nucleus by Podolyák *et al*. [89] and Farrelly *et al*. [91]. The energies and relative intensities of ^{190}W nuclei for fully stripped ions from summed data is presented in Table 4.3.

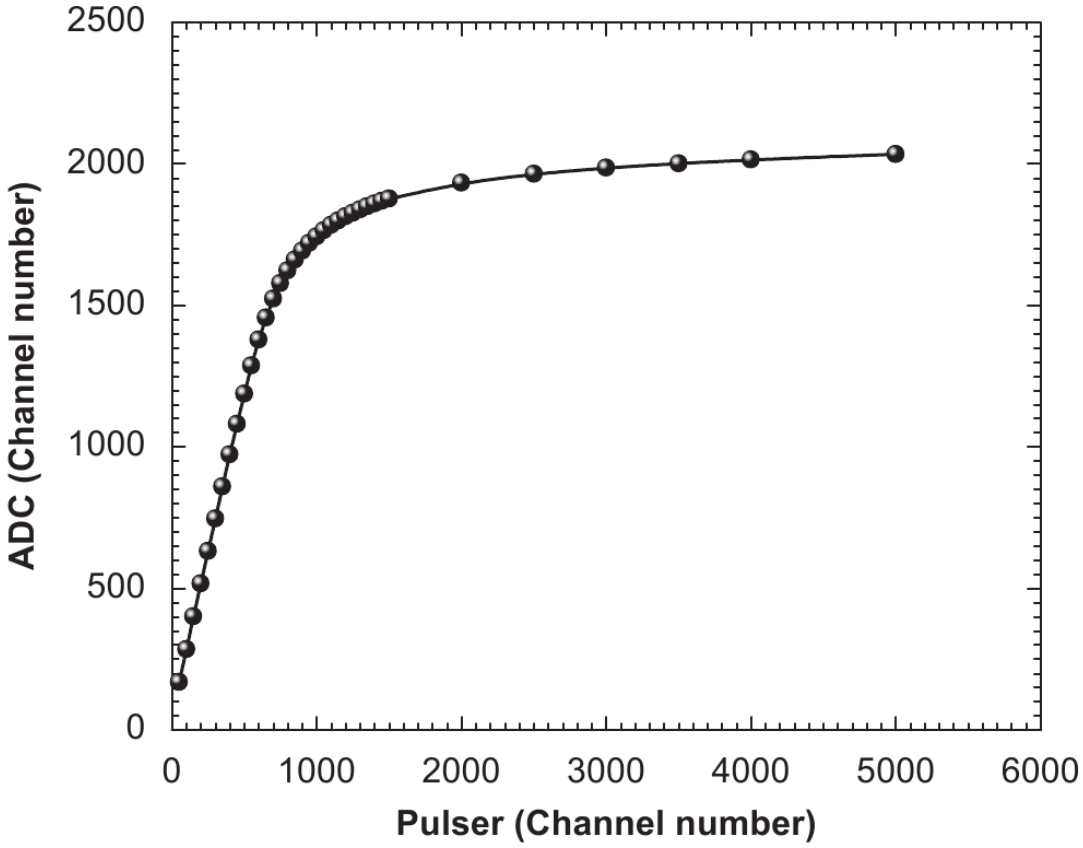

Figure 4.12: The characteristic energy response of the logarithmic MPR-32 preamplifier used with the DSSSDs, taken from Ref. [39].

^{191}W

The delayed γ-ray spectrum associated with ^{191}W nuclei from the present work is displayed in figure 4.11 *(f)*. A γ-ray transition with energy 167 keV together with the characteristic W K_α and K_β X ray with energies 58 and 67 respectively is clearly identified. These transitions are in agreement with previously reported work on this nucleus by Steer *et al*. [88]. Two γ-ray transitions with energies 99 and 127 keV are also identified in the current data. Table 4.3 shows the energy and relative intensity of ^{191}W nuclei for fully stripped ions from the summed data.

^{192}Re

A single γ-ray transition with energy 159 keV is clearly identified in figure 4.11 *(g)* which shows the delayed γ-ray spectrum associated with fully stripped ^{192}Re nuclei

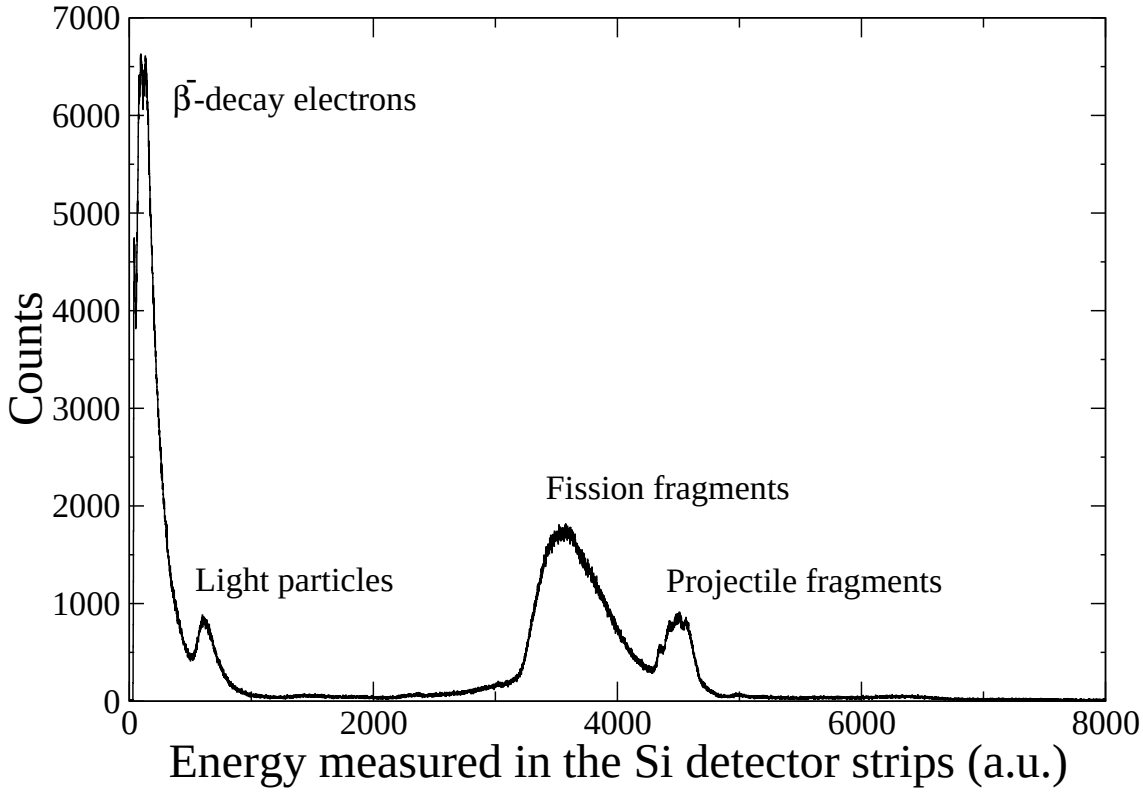

Figure 4.13: Total deposited energy in DSSSDs for the summed for the ^{190}Ta, ^{192}Ta and ^{194}Re centred settings. The double peaks at the centre of this plot represent the deposited from the implantation (right) and fission fragments (left) respectively.

from the current work for the summed data. This transition is in agreement with previously reported work on this nucleus by Caamaño *et al.* [7] and Steer *et al.* [88]. Table 4.3 shows the energy and relative intensity of ^{192}Re nuclei for fully stripped ions from the summed data.

^{193}Re

Figure 4.11 *(h)* shows the delayed γ-ray spectrum associated with ^{193}Re nuclei for fully stripped ions from the summed data. The γ-ray transition with energy 145 keV together with the characteristic Re K_α and K$_\beta$ X rays with energies 60 and 69 respectively are clearly identified. These transitions are in agreement with previously reported work on this nucleus by Caamaño *et al.* [7] and Steer *et al.* [88]. The energy and relative intensity of ^{192}Re nuclei for fully stripped ions from the summed data is shown in Table 4.3.

4.6 Active stopper and β^--decay measurements

4.6.1 Measurements with the mesytec logarithmic preamplifier

One of the challenges in designing the electronics of the detection system for such experiments was the range of the charged particle energies that must be measured [39]. The implanted ions deposit more than 1 GeV total energy when stopped in the DSSSDs, while their subsequent β decays typically deposit less than 1 MeV [39]. This issue was solved by utilizing a new counting system designed to measure both the implanted ions and their β decays in the same, or neighbouring pixels in the DSSSDs. The Mesytec MPR-32 preamplifier was used for the 16 front and 16 back strips of a single DSSSD [39]. The Mesytec MPR-32 preamplifier provided combined linear and logarithmic response modes [39]. The linear preamplifier with a range up to 10 MeV was used to measure the beta particles while the logarithmic part measured the implanted ions with energies up to 3 GeV. Figure 4.12 shows the response characteristics of the logarithmic MPR-32 (this figure taken from Ref. [39]). The linear part of the preamplifier was calibrated using a ^{207}Bi source which emits monoenergetic conversion electrons [39], (see Appendix B2). The energy resolution of the 976 keV electron line was measured to be approximately $\sim$ 15-20 keV (FWHM) [39]. The logarithmic part was calibrated by using simulated high energy signals from a pulser. The detection limit for the electron measurements using this counting system was approximately 150 keV at room temperature [39].

The total energy spectrum of the implanted ions and β^- particles in DSSSDs 1 and 2 for the summed data from the ^{190}Ta, ^{192}Ta and ^{194}Re centred settings are shown in figure 4.13. The left-hand peak in figure 4.13 correspond to the β^- particles emitted after the implantation. Light particles which pass through the Sci detectors at the final focal plane of the FRS are also visible in figure 4.13. The two peaks in the centre part of figure 4.13 represent the implantation in DSSSDs 1 and 2. The left-hand peak corresponds to transmitted fission fragments while the right-hand peak are the transmitted, heavy projectile fragments (which are the events of interest in the present work). A software condition was applied in the off-line analysis to the total deposited

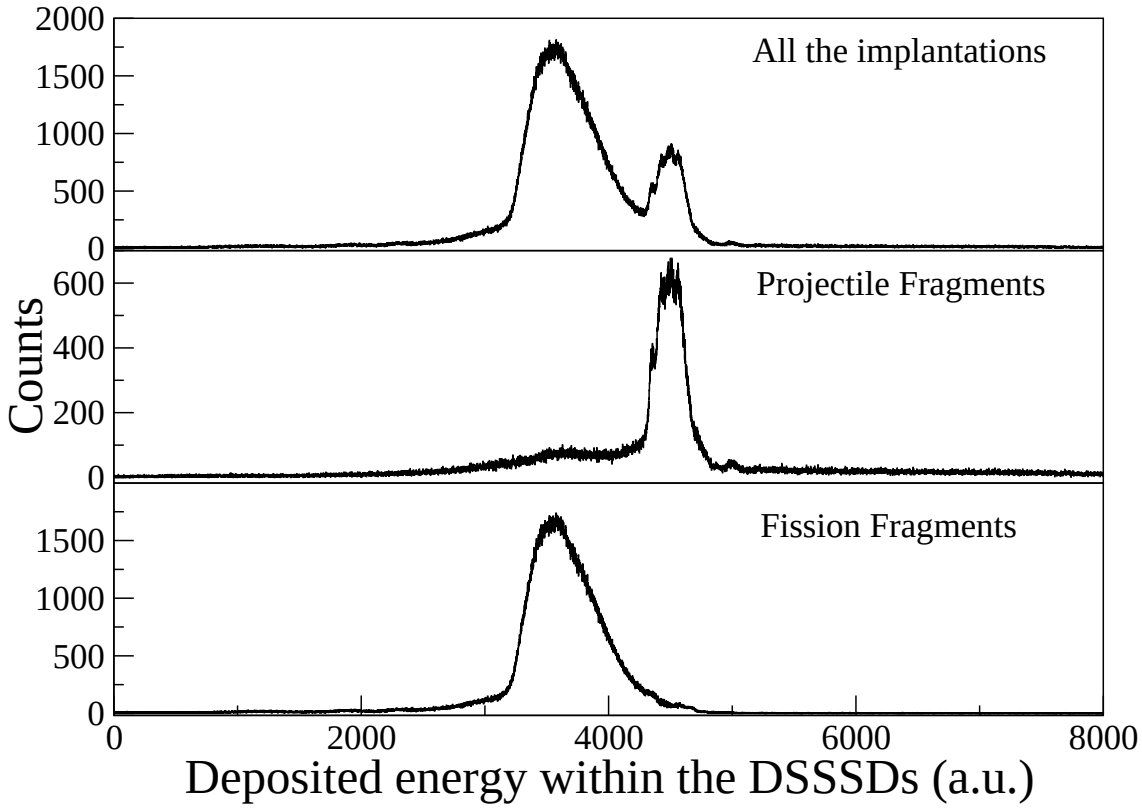

Figure 4.14: (Upper) Total energy spectra in the silicon active stopper detector ; *(Middle)* the energy deposited associated with heavy, *A∼190* projectile fragments; *(Lower)* the energy deposited transmitted projectile the fission fragments. These are for the summed data for the settings centred on the transmission of the ^{190}Ta, ^{192}Ta and ^{194}Re for fully stripped ions.

energy spectrum of the DSSSDs (see figure 4.14) to select the projectile fragments ions.

4.6.2 Implant-decay correlation technique

The technique of correlating the implanted ions with their subsequent β decay is based on the measurement of two main parameters: *(i)* the identification of the implantation position in the DSSSDs detector and *(ii)* the correlation time between the implanted ions and subsequent β particle in the same or 8 neighbouring pixels. In the current experiment, the FRS was operated in a monochromatic mode [73], which had the effect of distributing the implanted ions across a relatively wide area on the DSSSDs. This approach was required because of two advantages; first to minimize the probability of having multiple implantations in the same pixel during a typical

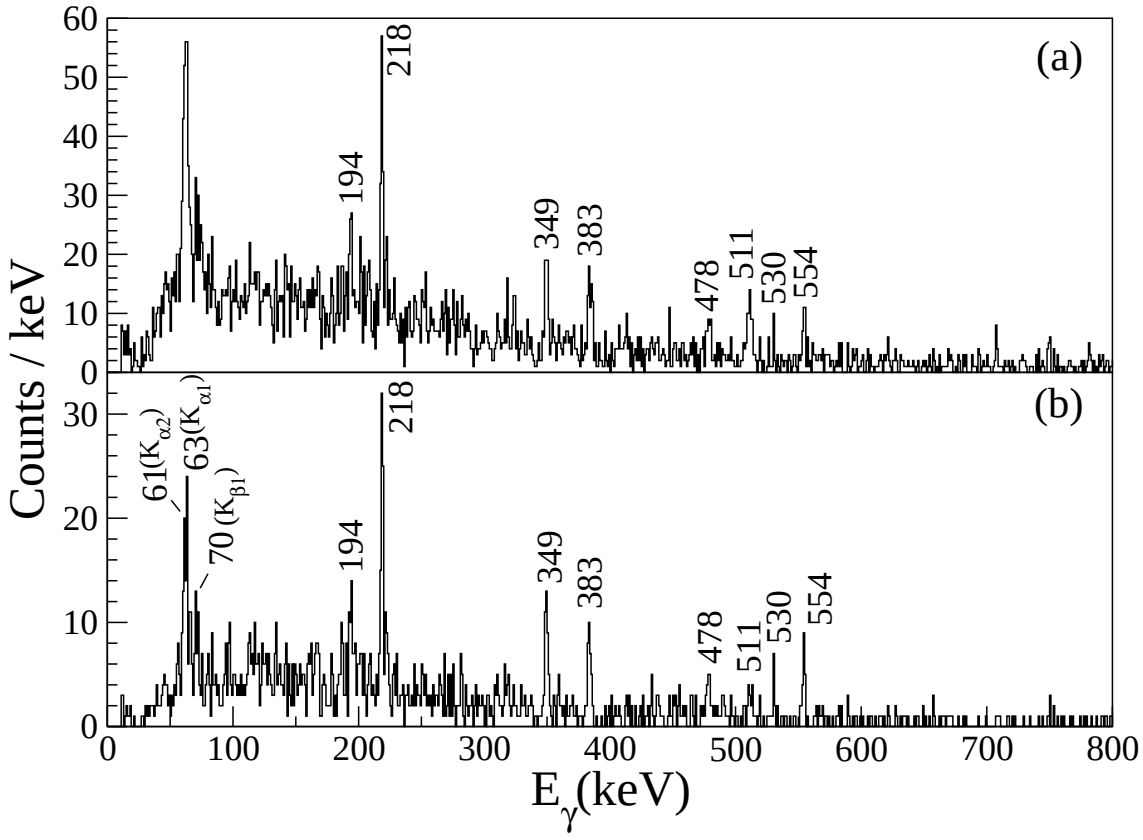

Figure 4.15: β-delayed γ-ray spectrum showing decays from excited states in ^{194}Os. The correlation time range was $\Delta t = (0 - 50)$ s show these data the difference of applying only the correlation between the implantations and decays in the same pixel (lower panel *(a)*) and implantations and decays in the same pixel plus decays in the 8 neighbouring pixel upper panel.

correlation time; and second to minimize the distribution range of the ions of a given species within the active stopper, (therefore, selected isotopes were stopped in a single layer in the active stopper silicon detectors). The ions were implanted in the active stopper and their positions determined by measuring the implantation strip positions as a coordinate of (x, y). The absolute measurement of the implantation time was made with a digital, (absolute) time stamp. Valid implanted events were identified by the production of a high-energy signal in the active stopper detector (> 10 MeV) measured using the logarithmic part of the pre-amplifier response. For the isomer measurements, the implant-γ-ray correlation time for the γ-ray electronics DGF modules were fixed to be between $0 \rightarrow 400$ μs. After this time the γ-ray DGF electronics were closed for that event. If a subsequent decay signal was detected in the DSSSD, the decay trigger

logic gave a logic signal for the γ-ray electronics to be opened again. For such events, the DGF electronics were opened for a further 400 μs period following the β trigger. To measure the decay signal, the linear region of the DSSSD pre-amplifiers were used. For each implanted pixel and for a specific period of time after the implantation, energy deposited above the threshold (150 keV [39]) was considered to arise from the emission of a β particle from the last radioactive ion implanted in the same pixel. Due to the finite β-range in the DSSSDs and to increase the efficiency of measuring ion-correlated β particle decay events in the off-line software analysis, a matching program was developed to record the decays in the directly neighbouring pixels to that of the original ion implant. Therefore, the correlation algorithm considered implantations and decays in the same pixel and decays in 8 neighbouring pixels (i.e. the β particles were not always measured in the same pixel to that which their radioactive mother ion was implanted).

In this chapter, the β-delayed γ-ray spectroscopy of the ^{194}Re $\rightarrow$ ^{194}Os decay is discussed. The difference between applying the ion-β correlation only between *(i)* the implantations and decays in the same pixel and *(ii)* decays in the same pixel plus in the 8 neighbouring pixels for the β-delayed γ-ray spectrum for the ^{194}Re decay is shown in figure 4.15. The lower panel of the figure 4.15 has fewer statistics but a better signal-to-noise ratio than the spectrum in the upper panel. For this reason, the correlation algorithm applied to these data was only between the implantations and decays in the same pixel in the DSSSDs. This approach was applied for all β-delayed γ-ray spectra of the nuclei in the particle identification plot (see figure 4.7). To confirm this approach, good agreement was obtained from the comparison between the β-delayed γ-ray spectrum for excited states in ^{190}W from the current work with the previous reported results of this nucleus from isomer spectroscopy [89, 91]. Figure 4.16 shows the β-delayed γ-ray spectrum for excited states in ^{190}W from the decay of ^{190}Ta. This decay has been reported separately in Ref. [87].

4.6.3 β-decay half-life measurements

β-decay half-lives were measured in the current work. The decay half-lives of the mother nuclei were deduced from the time correlation between the implantation time of the identified fragments in the DSSSD detector and the subsequent β-decay in the

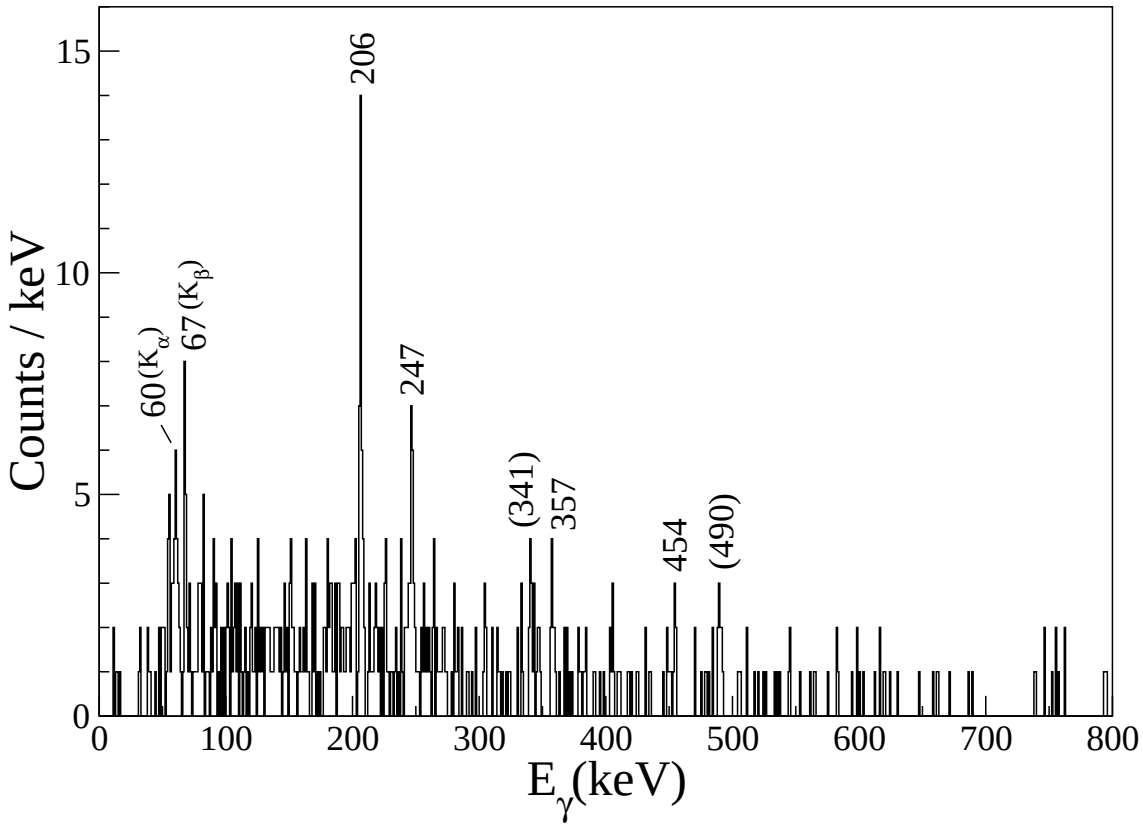

Figure 4.16: β-delayed γ-ray spectrum for excited states in ^{190}W, the ion-β correlation time range was $\Delta t = (0 - 60)$ s. These data are discussed in detail in Ref. [87].

same pixel. The time correlation was determined using the same DGF time stamping system used in the isomer decay analysis, providing a resolution of 25 ns [39]. The time differences were histogrammed and used to generate a β-decay curve for the identified fragments. These data could then also be further gated by the condition that specific discrete γ rays associated with decay in the daughter nuclei were also observed. The decay curves were fitted to single-component exponential decay using a least square fitting minimization method and assuming a constant background level. Using the β^--correlation only approach, the half-life measurement for the ^{192}Re measured here of 16(2)s is consistent with the literature value for this decay of 16(1) s [23, 92]. The decay time curves for both ^{190}Ta and ^{192}Re from the current work for ion-β-correlations are shown in figures 4.17 and 4.18 respectively for the summed data from the ^{190}Ta, ^{192}Ta and ^{194}Re centred settings.

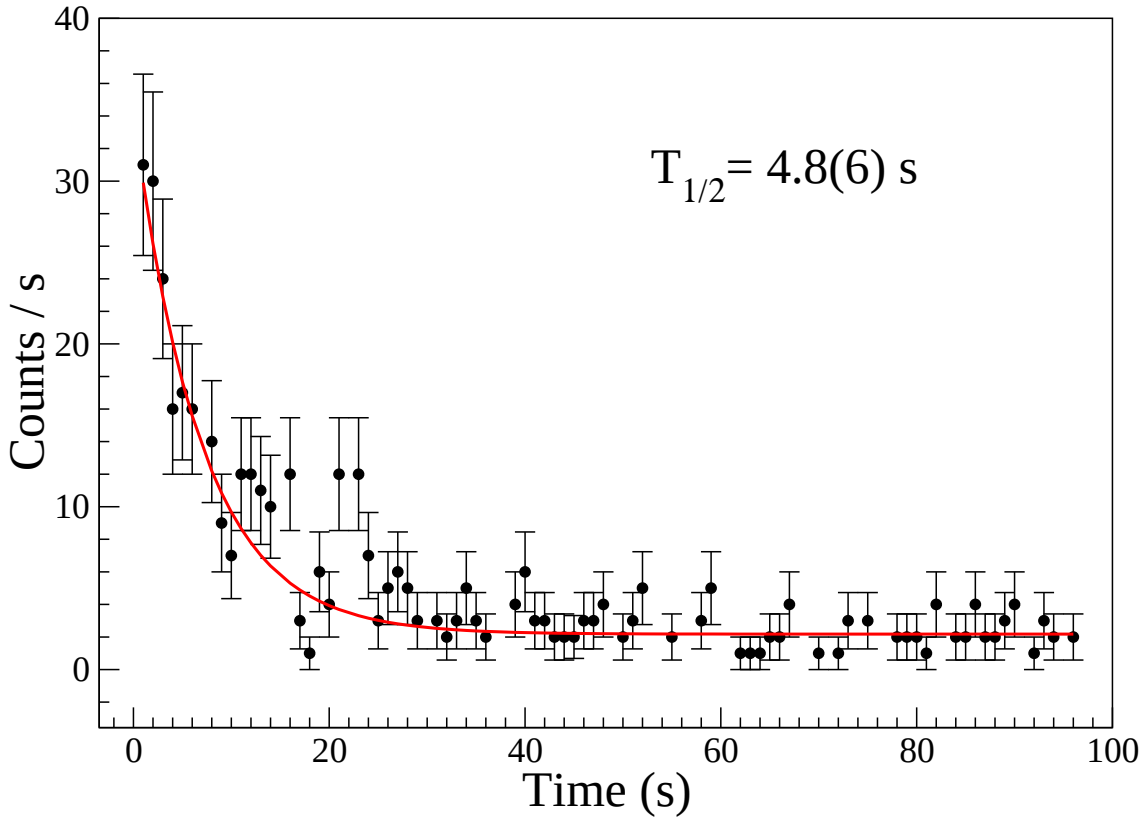

Figure 4.17: Decay time curve for β-decay of ^{190}Ta $\rightarrow$ ^{190}W from ion-β time correlations in the current work. By using a least squared fit the data were fitted to a single exponential decay function plus a constant background level.

4.7 Results

4.7.1 β^--delayed γ-ray spectroscopy of the ^{194}Re $\rightarrow$ ^{194}Os decay

γ rays emitted following the β^--decay of ^{194}Re ($Z = 75$) to populate excited states in the daughter nucleus ^{194}Os ($Z = 76$) were measured. The β-delayed γ-ray spectrum of ^{194}Os for ion-β correlation times (in the same pixel) of Δt ($implant - \beta$) $= 0 - 50$ s is shown in figure 4.19. The previously reported decays from the yrast 2^+, 4^+ and 6^+ states in ^{194}Os with energies 218 [21, 93, 94], 383 [21, 94] and 530 [94] keV together with the characteristic Osmium $K_{\alpha1}$, $K_{\alpha2}$ and $K_{\beta1}$ X rays with energies 63, 61 and 70 keV respectively are clearly identified in this spectrum. A discrete γ-ray transition with energy 478 keV is also clearly observed, consistent with the previously reported decay [21, 93] from the $I^\pi = 0_2^+$ state in the ^{194}Os. Three previously unreported transitions in ^{194}Os with energies 194, 349 and 554 keV are also observed. To verify that these

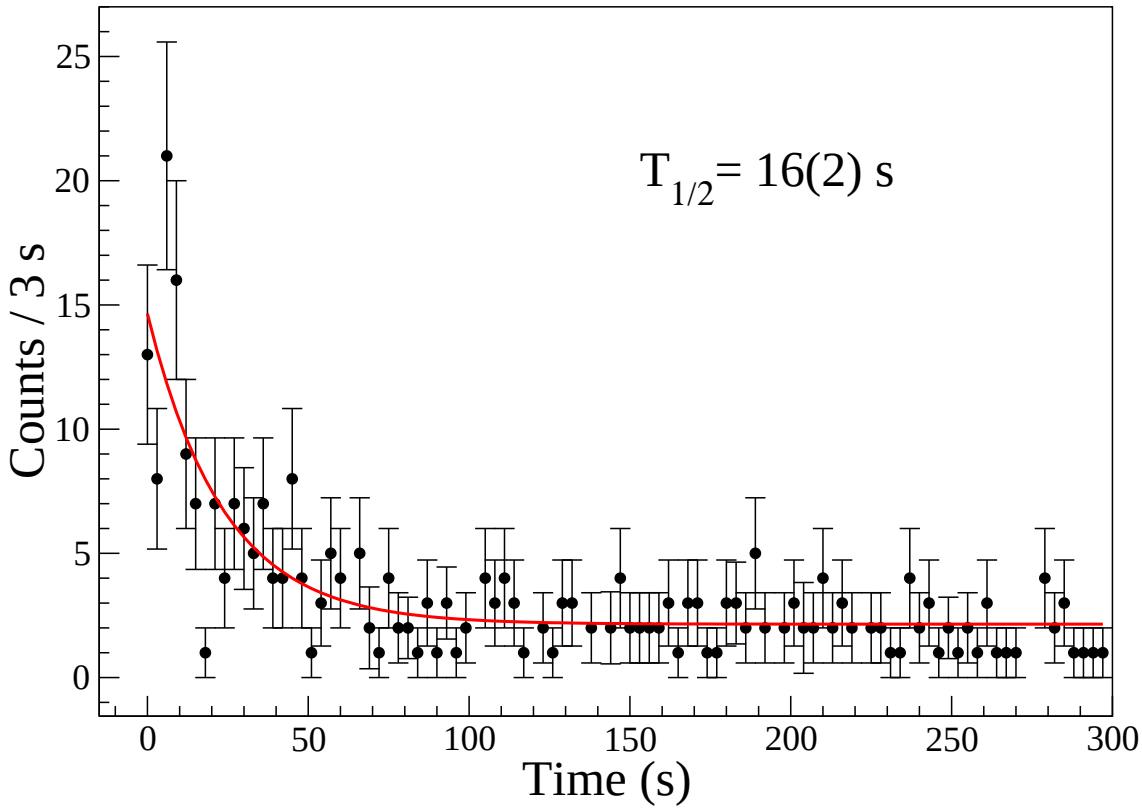

Figure 4.18: Decay time curve for β-decay of ^{192}Re $\rightarrow$ ^{192}Os from the ion-β-time correlations in current work. The published half life value for ^{192}Re of 16(1) s [23, 92] is consistent with the value deduced from the current work of 16(2) s.

three transitions are associated with decays in the ^{194}Os daughter nucleus, β^{-}-delayed γ-ray spectra for all the nuclei in the particle identification plot of fully stripped ions from the summed data were examined for short ($\Delta t(implant - \beta) = 30$ s) and long correlation ($\Delta t(implant - \beta) = 120$ s) times, see figures 4.20, 4.21, 4.22 and 4.23. The γ-ray transitions with energies 194, 349 and 554 keV are only associated with the decay of ^{194}Re into ^{194}Os. Table 4.4 shows the experimental energies and relative intensities for the γ-ray transitions associated with ^{194}Os in the current work for ion-β-correlation times.

^{194}Re is the heaviest isotope of this element studied to date. A β-decay half-life for ^{194}Re of $T_{1/2}$=7(1) s is obtained by measuring the time differences between the implanted ions in the active stopper and their subsequent correlated β particles in the same pixels, (see figure 4.24). Note that this represents the pure β-ion correlations times. By investigating the different of ion-β decay profiles gated on specific γ-ray

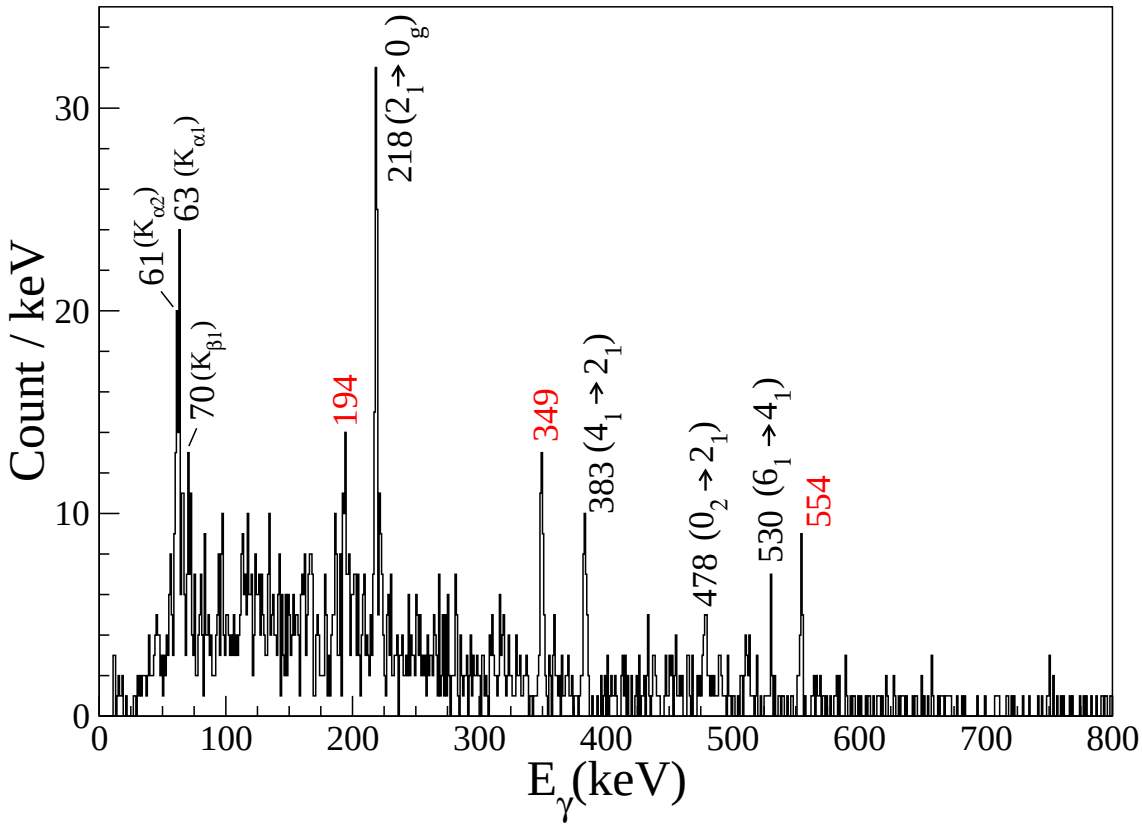

Figure 4.19: β-delayed γ-ray spectrum of ^{194}Os for correlation time Δt $(implant - \beta) = 0 - 50$ s for fully stripped ions from the summed data. Previously unreported peaks were labelled in red.

transitions in the ^{194}Os daughter, information could be inferred which leads to the conclusion of at least two and probably three individual β^--decaying states in ^{194}Re, each with a different decay half-life. The background level in the decay curve of ^{194}Re of approximately 10 counts, is notably higher than the background levels associated with decays from other nuclei, such as ^{190}Ta and ^{192}Re (see figures 4.17 and 4.18 respectively). Therefore, γ-ray gated β-decay time spectra associated with all the identified transitions in the β-delayed γ-ray spectrum of ^{194}Os were measured for different correlation times between Δt $(implant - \beta) = 0 \rightarrow 1000$ s in steps of 40 s, see figures 4.25 and 4.26.

For the 530 keV transition (see figure 4.25 *(d)*), there is intensity associated with the decay transition after 160 s while in case of 478 keV transition (see figure 4.25 *(c)*), no such intensity is apparent above the constant, random background level after 40 s. The ^{194}Re decay half-life associated with feeding to the 478 keV transition was

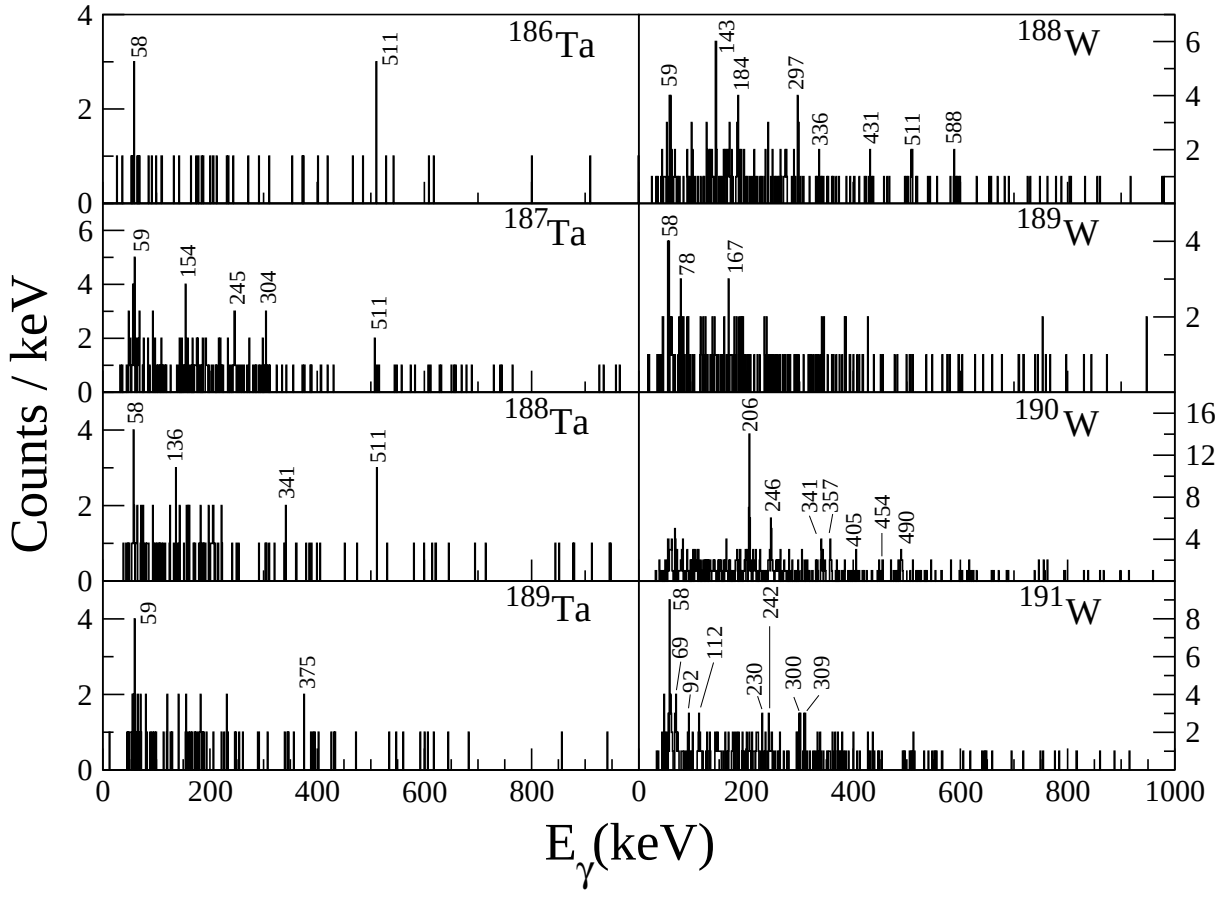

Figure 4.20: β^--delayed γ-ray spectra of the Tantalum and Tungsten daughter isotopes for short correlation times $\Delta t(implant - \beta) = 30$ s from the current work.

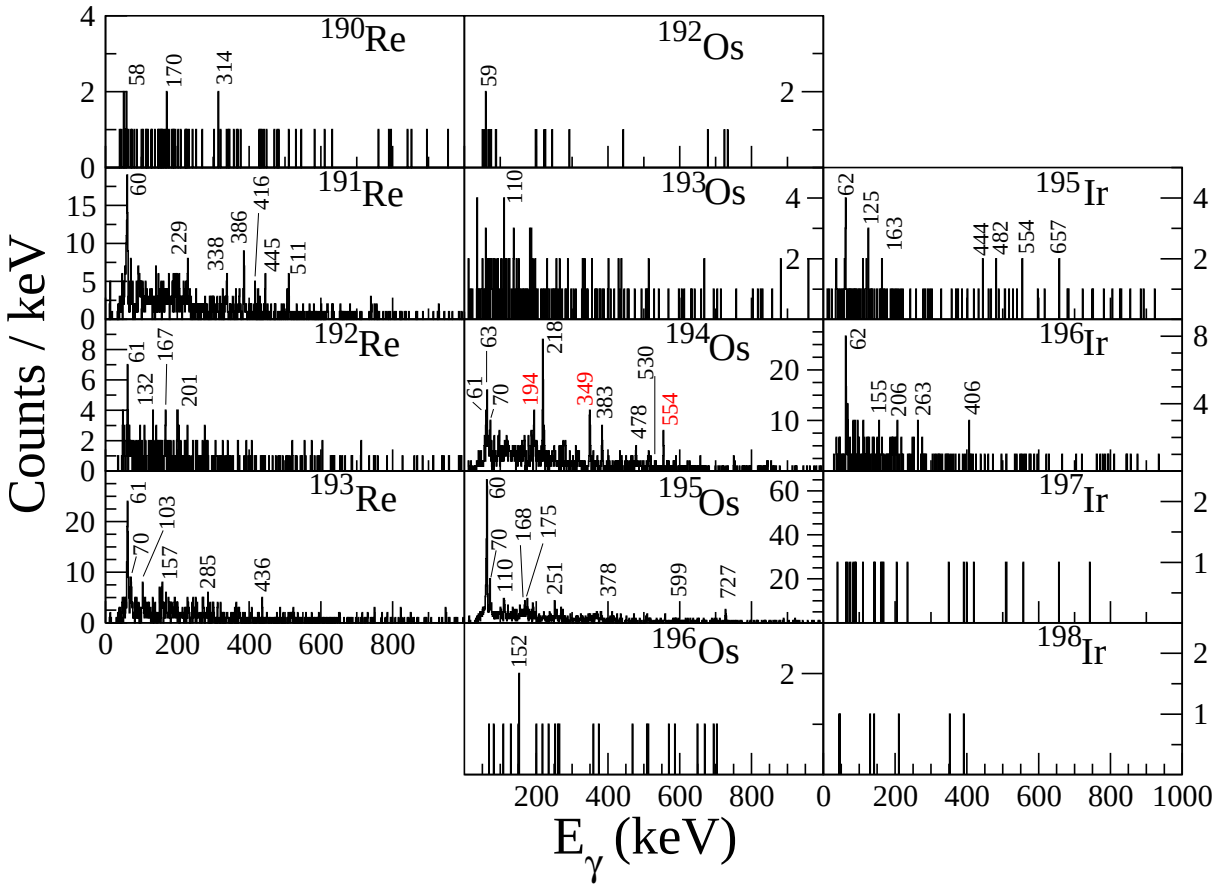

Figure 4.21: β-delayed γ-ray spectra of Rhenium, Osmium and Iridium daughter isotopes for correlation times of $\Delta t(implant - \beta) = 30$ s from the current work.

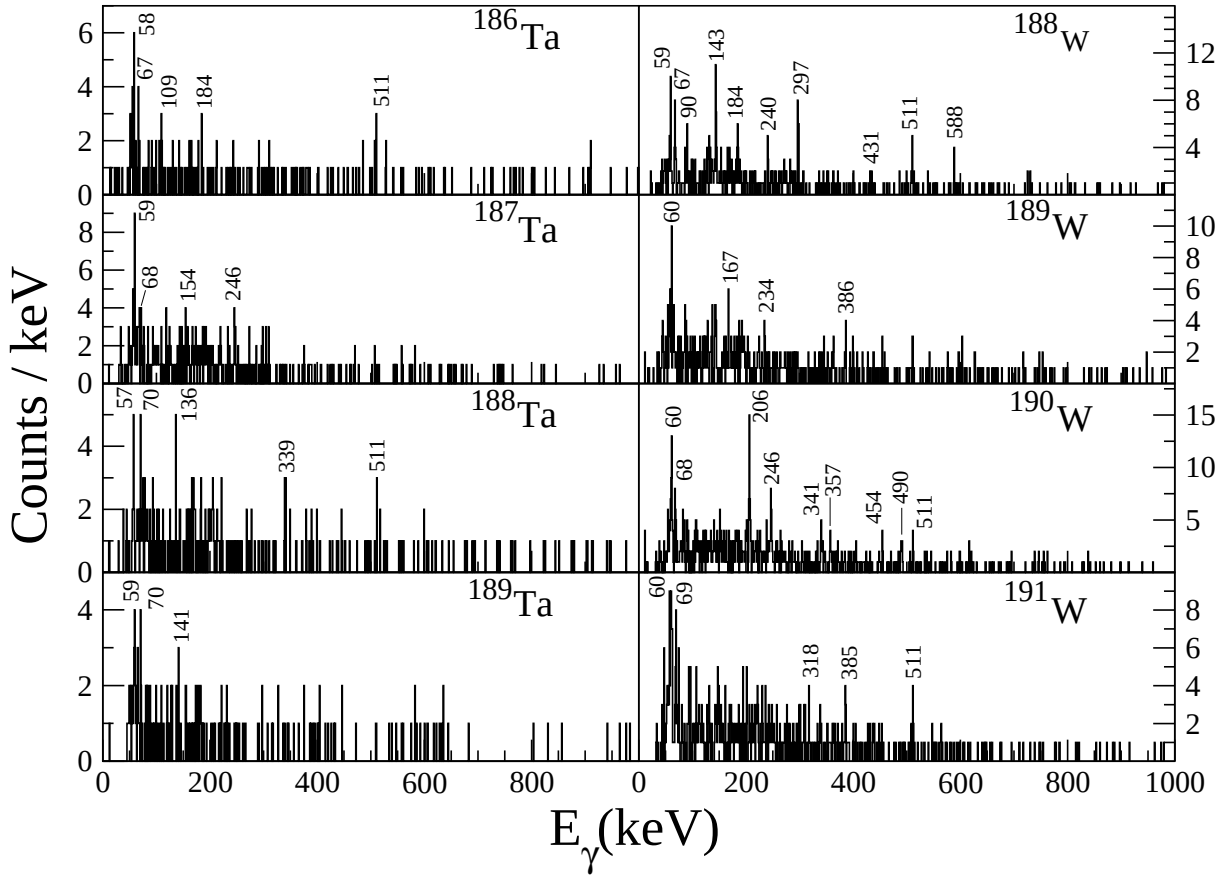

Figure 4.22: β-delayed γ-ray spectra of the Tantalum and Tungsten daughter isotopes for correlation times of $\Delta t(implant - \beta) = 120$ s from the current work.

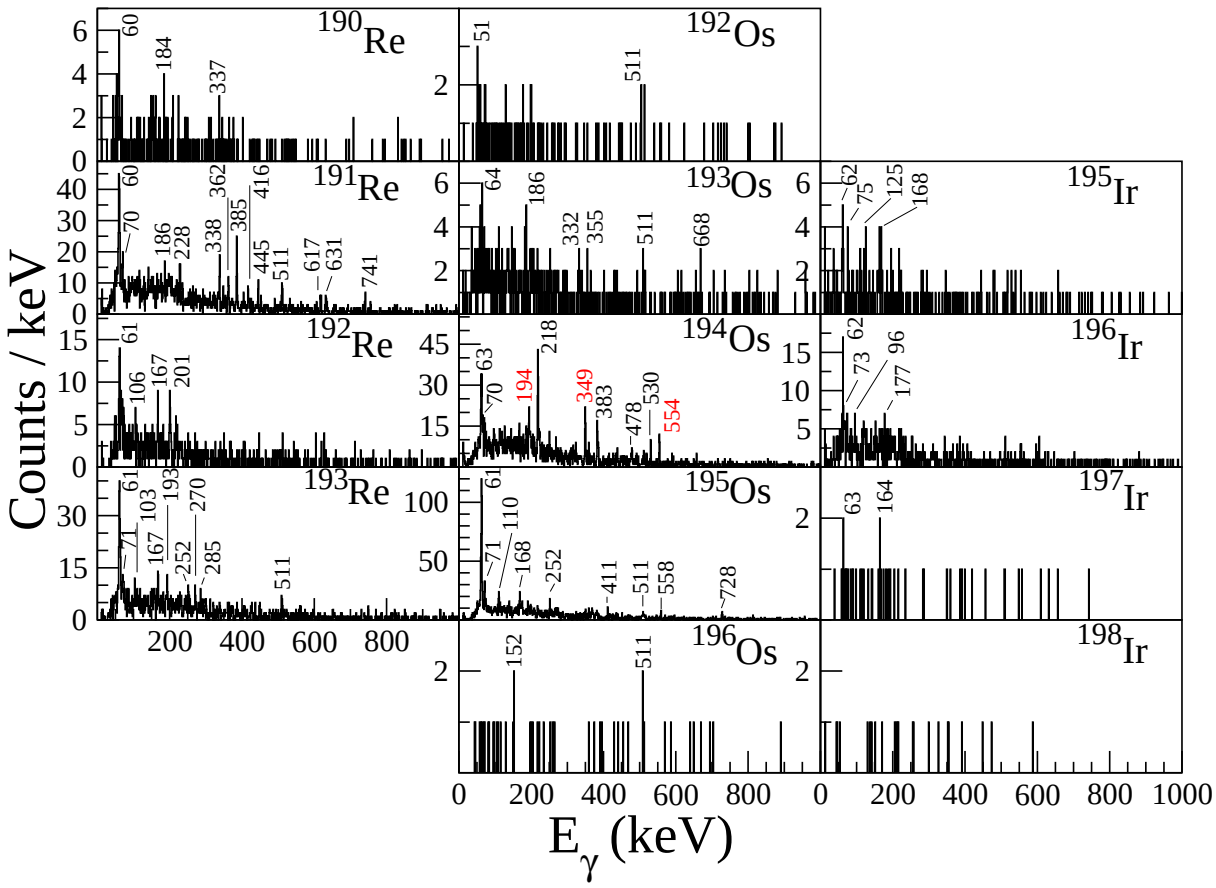

Figure 4.23: β-delayed γ-ray spectra of the Rhenium, Osmium and Iridium isotopes daughter for correlation times $\Delta t(implant - \beta) = 120$ s from the current work.

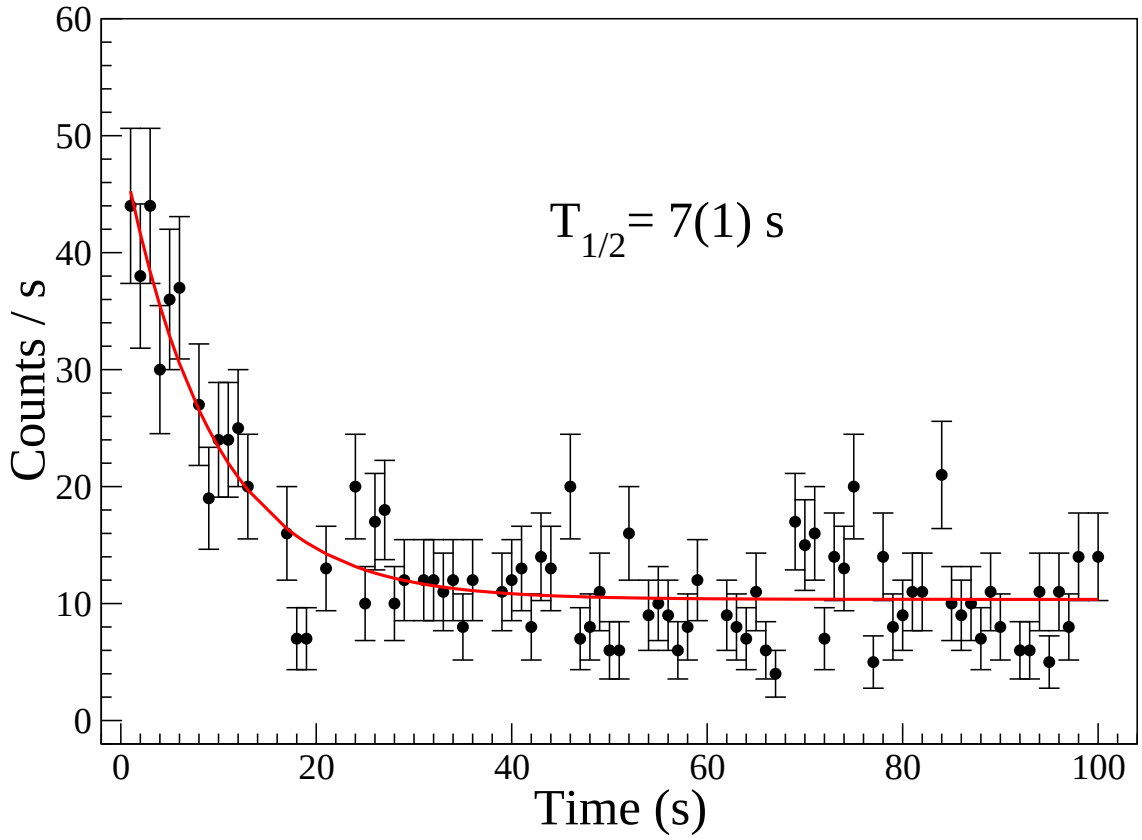

Figure 4.24: Decay time curve for ^{194}Re obtained from the time differences between the implanted ions in the active stopper and their subsequent correlated β particles in the same pixel for fully stripped ions from the summed data.

measured to be 9(2) s, consistent within the experimental uncertainties of the half-life value from the decay time from the pure ion-β correlation shown in figure 4.24. The half-life measurements indicate that there are at least two (and likely three) β decays associated of ^{194}Re $\rightarrow$ ^{194}Os with different half-lives. There is evidence for a decay with $T_{1/2}$=7(1) s (see figures 4.24 and 4.25 *(c)*) which feeds to the 0_2^+. Note that by the standard β decay selection rules, this also implies a significant degree of feeding in the β decay of ^{194}Re *direct to the* $I^\pi=0^+$ *ground state* of ^{194}Os, which not be associated with any co-incident, β-delayed γ-ray transition. This is consistent with the observation of a half-life of 7(1) s obtained in figure 4.24 for the correlations between ions and beta-particles only. A second decay with of approximately 21(6) s was measured from the β-delayed γ-ray projection gated by the 554 keV transition, see figure 4.26 *(c)*. There is also evidence for a third decaying state in ^{194}Re with a longer half life of

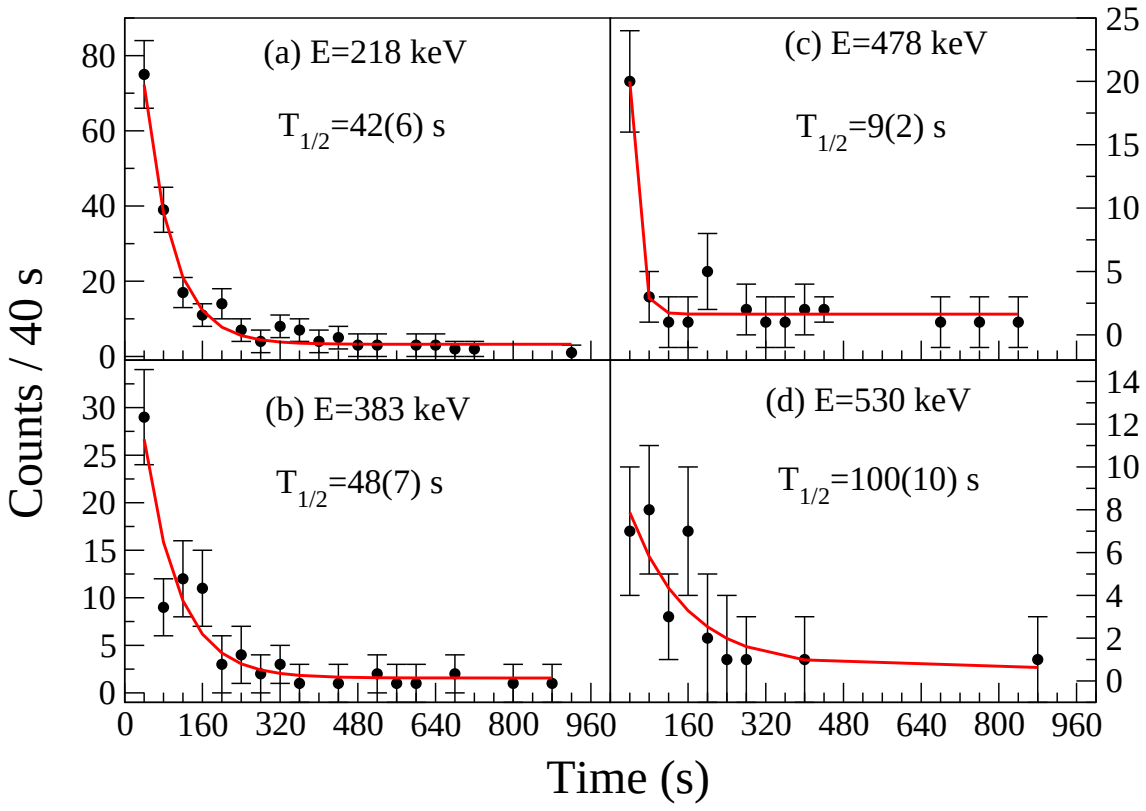

Figure 4.25: β-delayed γ-ray gated time spectrum for previously reported transitions 218, 383, 478 and 530 keV associated with ^{194}Os for different correlation times $\Delta t(implant - \beta) = 0 \rightarrow 1000$ s in steps of 40 s from the current work.

a approximately 100 s which feeds the 6_1^+ state in ^{194}Os. The long half-life explains the "non-observation"of the 530 keV transition for short correlation times in the β-delayed γ-ray spectrum of ^{194}Os, see figure 4.27. The three previously unreported γ-ray transitions with energies 194, 349 and 554 keV have been independently associated with transitions in ^{194}Os using deep inelastic reactions by Dracoulis *et al.,* [95]. Dracoulis *et al.,* placed these transitions in a level scheme of ^{194}Os as decays from states with spin / parites $I^\pi \sim 10^- - 11^-$ [95]. Table 4.4 shows the energies and observed intensities of ^{194}Os for fully stripped ion from the summed data. Figure 4.28 shows the experimental level scheme of ^{194}Os.

Table 4.4: Experimental energies and relative intensities of ^{194}Os nuclei for short correlation times $\Delta t(implant - \beta) = 0 - 10$ s, $\Delta t(implant - \beta) = 0 - 40$ s and long correlation time $\Delta t(implant - \beta) = 40 - 440$ s of fully stripped ions from the combination of ^{190}Ta, ^{192}Ta and ^{194}Re setting.

Correlation time (Δt *implant* $- \beta$) (s)	$I_i \rightarrow I_f$	γ-ray Energy (keV)	Counts	Absolute Photopeak Efficiency	N_γ
0-10		193.4(3)[a]	23(5)	0.27	83(20)
	$2^+ \rightarrow 0^+$	218.3(4)[b]	35(7)	0.26	132(30)
		348.6(3)[a]	16(4)	0.21	75(20)
	$4^+ \rightarrow 0^+$	383.8(5)[c]	8(3)	0.20	40(15)
	$0_2^+ \rightarrow 2^+$	477.6(4)[d]	12(4)	0.17	70(24)
	$6^+ \rightarrow 0^+$	530.1(6)[f]	3(3)	0.16	18(18)
		554.1(2)[a]	8(3)	0.15	50(20)
0-40		193.6(4)[a]	24(6)	0.27	87(23)
	$2^+ \rightarrow 0^+$	218.1(2)[b]	57(8)	0.26	214(37)
		349.0(3)[a]	33(6)	0.21	154(32)
	$4^+ \rightarrow 0^+$	383.3(4)[c]	20(5)	0.20	99(27)
	$0_2^+ \rightarrow 2^+$	477.8(5)[d]	14(4)	0.17	79(24)
	$6^+ \rightarrow 0^+$	530.1(6)[f]	3(3)	0.16	18(18)
		553.9(3)[a]	15(4)	0.15	94(27)
40-400		193.6(4)[a]	18(9)	0.27	65(33)
	$2^+ \rightarrow 0^+$	218.2(2)[b]	80(11)	0.26	301(51)
		348.9(2)[a]	40(7)	0.21	187(38)
	$4^+ \rightarrow 0^+$	383.2(3)[c]	33(8)	0.20	163(43)
	$0_2^+ \rightarrow 2^+$	477.9(6)[d]	12(7)	0.17	68(40)
	$6^+ \rightarrow 0^+$	530.4(3)[f]	16(9)	0.16	97(55)
		553.9(3)[a]	11(5)	0.15	69(32)

[a] Transitions associated with the decay of the ^{194}Os nucleus

[b] See Ref. [21, 93, 94], [c] See Ref. [21, 94]

[d] See Ref. [94][f] See Ref. [21, 93].

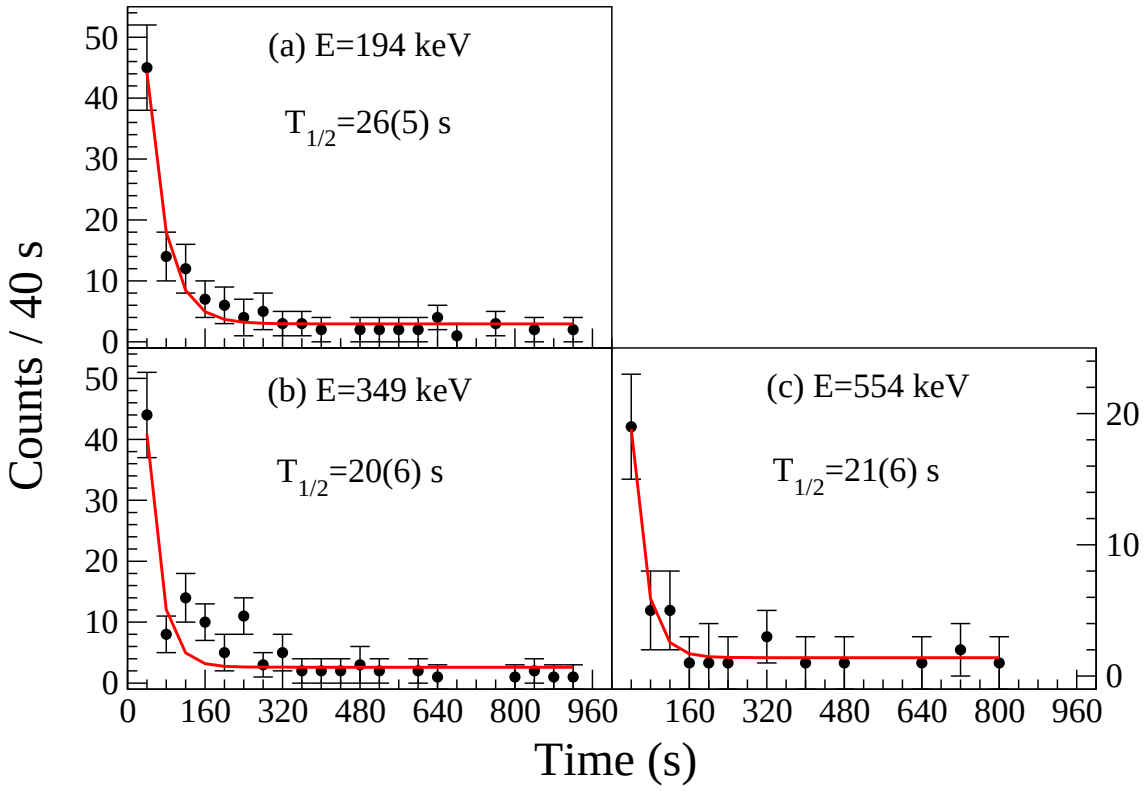

Figure 4.26: β-delayed γ-ray gated time spectra for the previously unreported transitions 194, 349 and 554 keV transitions associated with decay in ^{194}Os for different correlation times $\Delta t(implant - \beta) = 0 \rightarrow 1000$ s in steps of 40 s from the current work.

4.8 Discussion

4.8.1 Multi Quasi Particle (MQP) calculations for ^{194}Re

Multi Quasi Particle (MQP) calculations have been performed by Dracoulis [96] to predict the spin and parity of the low-lying states in the ^{194}Re mother nucleus. These have been performed for both the prolate and oblate deformations in this nucleus assuming axial symmetry, see Tables 4.5 and 4.6 respectively. The MQP calculations predict that in case of the ^{194}Re nucleus there is a low-lying competing prolate configurations with I^{π}=11^{-}, arising from the coupling of neutron orbital 13/2^{+}[606]$\uparrow$ to the proton orbital 9/2^{-}[514]$\uparrow$ respectively. For oblate deformation, the lowest predicted energy states from these calculations have I^{π}=0^{+}, 1^{-} and 1^{+} arising from the coupling of neutron 1/2^{+}[660]$\uparrow$ with the 1/2^{+}[411]$\downarrow$, 1/2^{-}[550]$\uparrow$ and 3/2^{+}[402]$\downarrow$ proton orbitals

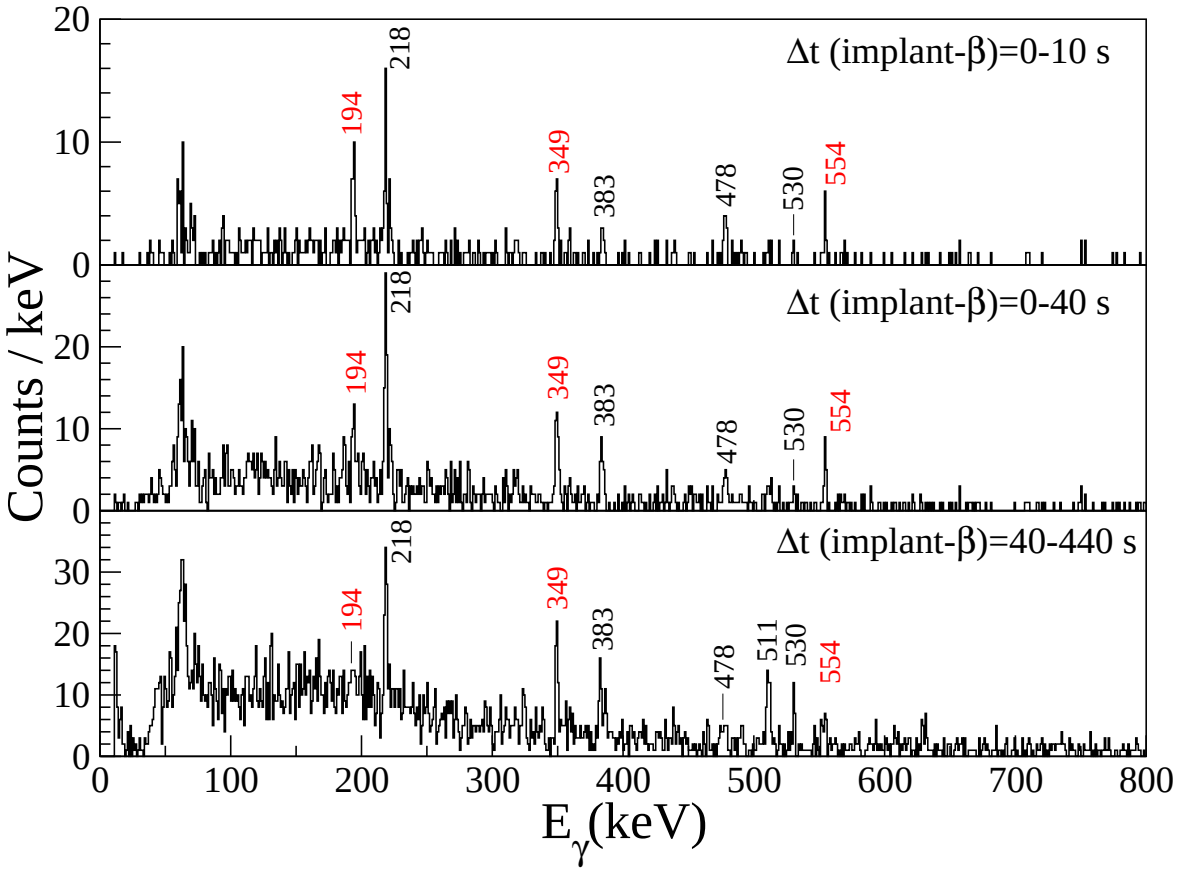

Figure 4.27: β-delayed γ-ray spectra showing transitions in ^{194}Os for different correlation time $\Delta t(implant - \beta) = 0 \rightarrow 10,\ 0 \rightarrow 40$ and $40 \rightarrow 440$ s, from the decay of ^{194}Re of fully stripped ions from the combination of ^{190}Ta, ^{192}Ta and ^{194}Re settings. Previously unreported transitions are labelled in red.

respectively.

Assuming that there are three beta decaying components with three different half lives from the ^{194}Re mother nucleus, from the half life measurements one possibility is that an oblate, low spin ($0^+,\ 1^-$ *or* 1^+) state decays to the 0_2^+ state with a 7(1) s half-life (see figure 4.25 *(c)*), while the predicted 11^- state prolate feeds to the higher-spin sequence associated with the 194, 349 and 554 keV transitions. Evidence for a third decay state comes from the longer apparent feeding time to the yrast 6^+ state in ^{194}Os. Note, the MQP calculations predict 28 separate two-quasi-particle intrinsic states in the ^{194}Re to lie below 400 keV, compared to just a single state in the even-even ^{194}Os daugher nucleus.

Table 4.5: Results of the Multi Quasi Particle (MQP) calculations for the ^{194}Re mother nucleus performed by Dracoulis [96] of the spin and the parity of low-lying states in this nucleus for axially symmetric prolate deformation. The quadrupole (ε_2) and the hexadecapole (ε_4) deformation parameters are taken from Ref. [97][a].

I^π	Neutron orbital (ν)	Proton orbital (π)	Energy (keV)	V_R^b (keV)	Net (keV)
6^+	$3/2^-[501]\uparrow$	$9/2^-[514]\uparrow$	22		(22)
3^+					
7^+	$13/2^+[606]\uparrow$	$1/2^+[411]\downarrow$	91	+70	161
6^+			91	-70	21
9^+	$13/2^+[606]\uparrow$	$5/2^+[402]\uparrow$	24	-84	-60
4^+			24	+84	108
10^+	$13/2^+[606]\uparrow$	$7/2^+[404]\downarrow$	337	+63	400
3^+			337	-63	274
2^-	$3/2^-[501]\uparrow$	$1/2^+[411]\downarrow$	67		(67)
1^-					
4^-	$3/2^-[501]\uparrow$	$5/2^+[402]\uparrow$	0		(0)
1^-					
5^-	$5/2^-[503]\downarrow$	$5/2^+[402]\uparrow$	264		(264)
0^-					
11^-	$13/2^+[606]\uparrow$	$9/2^-[514]\uparrow$	46	-71	-25
2^-			46	+71	117
12^-	$13/2^+[606]\uparrow$	$11/2^-[505]\uparrow$	304	-71	233
1^-			304	+71	375

[a] $\varepsilon_2 = 0.125$, $\varepsilon_4 = 0.067$ for the prolate deformation;

[b] Empirical Residual interactions.

Table 4.6: Results of the Multi Quasi Particle (MQP) calculations for the ^{194}Re mother nucleus performed by Dracoulis [96] of the spin and the parity of low-lying states in this nucleus for axially symmetric oblate deformation. The quadrupole (ε_2) and the hexadecapole (ε_4) deformation parameters are taken from Ref. [97][a].

I^π	Neutron orbital (ν)	Proton orbital (π)	Energy (keV)	V_R^b (keV)	Net (keV)
1^+	$1/2^+[660]\uparrow$	$1/2^+[411]\downarrow$	64	+70	134
0^+			64	-70	-6
2^+	$1/2^+[660]\uparrow$	$3/2^+[402]\downarrow$	2	+70	72
1^+			2	-70	-68
3^+	$3/2^+[651]\uparrow$	$3/2^+[402]\downarrow$	174	+70	244
0^+			174	-70	104
1^-	$1/2^+[660]\uparrow$	$1/2^-[550]\uparrow$	0	-70	-70
0^-			0	+70	+70
2^-	$3/2^+[651]\uparrow$	$1/2^-[550]\uparrow$	173	-71	102
1^-			173	+71	244

[a] $\varepsilon_2 = -0.158$, $\varepsilon_4 = 0.033$ for the oblate deformation.

[b] Empirical Residual interactions.

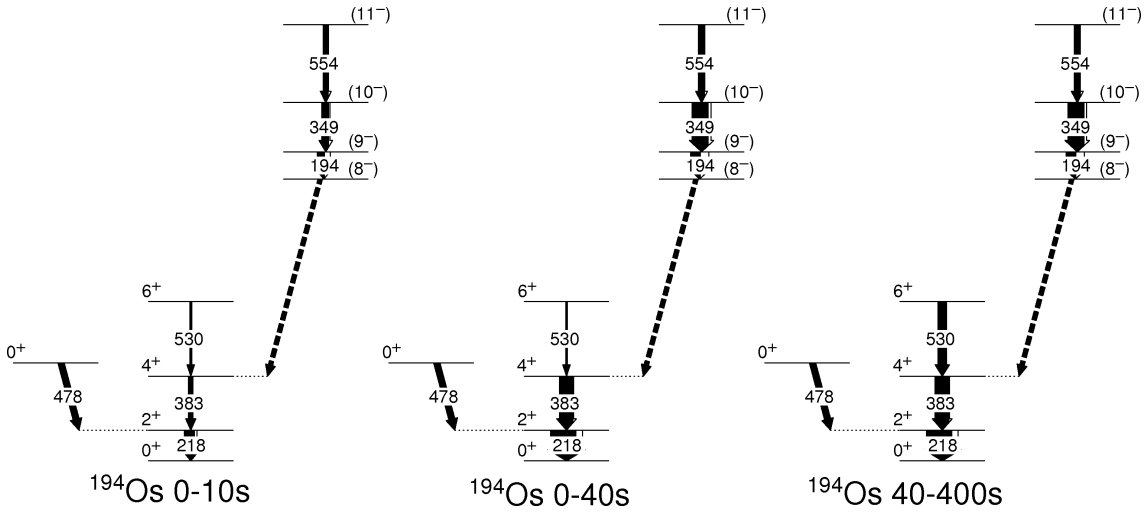

Figure 4.28: Experimental level scheme of ^{194}Os

4.8.2 Structure of ^{194}Os

Hartree-Fock calculations with a Woods-Saxon single-particle potential, performed by Nazarewicz *at al.* [98], predict a ground-state oblate deformation for ^{194}Os with $\beta = -0.14$. The possibility of ^{194}Os having an oblate deformed ground state has also been proposed by Casten *et al.*, [93]. The yrast states in ^{194}Os have been reported up to $I^{\pi} = (10^{+})$ by Wheldon *et al.*, using deep inelastic reactions [94]. The theoretical shape evolution with the number of nucleons for different chains of Yb, Hf, W, Os, and Pt isotopes for neutron number $N = 110 \rightarrow 122$ has also been studied by Sarriguren *at al.*, [12] using Skyrme Hartree-Fock plus BCS approach.

4.8.3 Low-lying collective excitations in ^{194}Os

A signature for a transition from prolate to oblate shapes was predicted as the number of neutrons increases from $N = 110 \rightarrow 122$ for Os isotopes [12]. The lighter Os isotopes exhibit a rotational behaviour which changes gradually toward γ-soft as the number of neutrons increases [12]. The results of this study are supported by recent theoretical calculation using the same approach performed by Robledo *et al.*, [22]. Their conclusion was the prolate to oblate transition takes place at $N = 116$ [22] and that there is a tendency toward triaxial shapes as the proton number is increased for fixed neutron numbers [22]. The current results on the excited states in ^{194}Os can

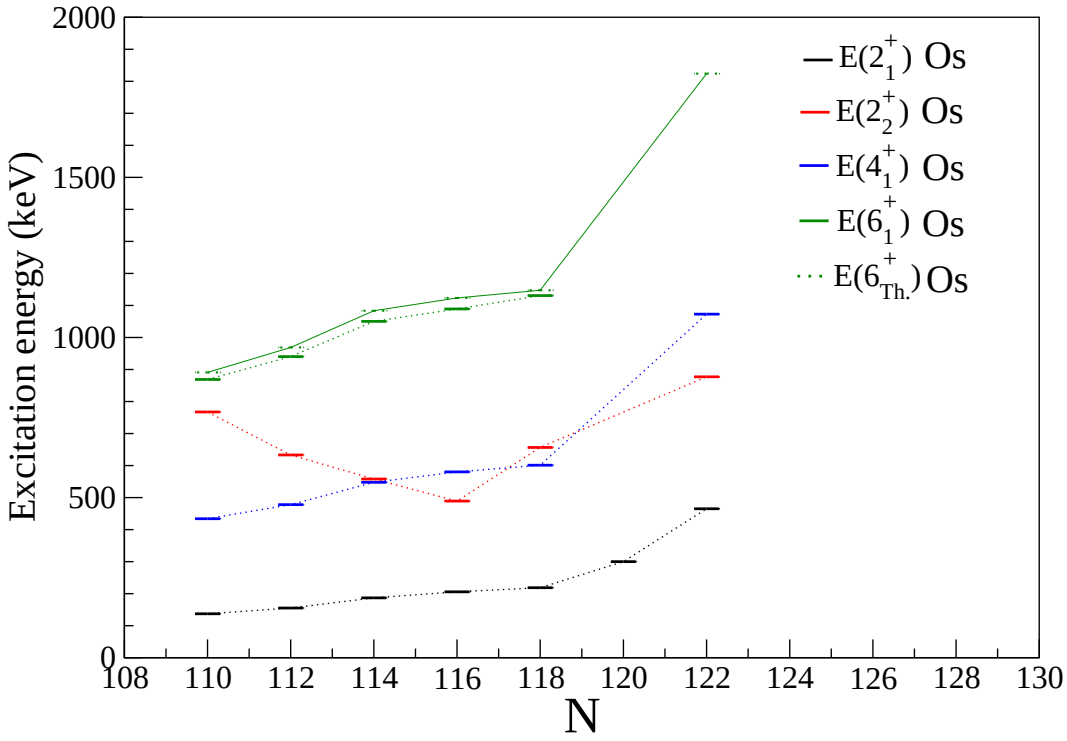

Figure 4.29: Systematics of the E(2_1^+), E(2_2^+), E(4_1^+), E(6_1^+)Exp and E(6_1^+)Th. energies for the neutron number N=110-122 for Osmium isotopes.

be compared with recent theoretical studies [11, 99] by using the Raman estimate [27], which relates the excitation energy of the first 2^+ state with the quadrupole deformation of the nucleus. The experimentally derived value of 218 keV for the first 2^+ state gives an estimate for the ground state deformation for ^{194}Os of $\beta_2 \sim 0.16$.

4.8.4 Systematics of ^{194}Os collective states

The energy of the lowest excited states can be used to infer information about the quadrupole character of the nuclei [25]. Systematics related to the yrast 2^+, 4^+, 6^+, the second 2^+ state (2_2^+) as well as the theoretically calculated 6^+ states ($6_{Th.}^+$) are presented in figure 4.29. The energy of $6_{Th.}^+$ state was calculated by using the following relation [100]:

$$6_{Th.}^+ = \left(3 \times E(2_1^+)\right) + (3 \times \varepsilon) \tag{4.6}$$

where ε is calculated assuming the Anharmonic Vibrator (AHV) Model using following expression [100].

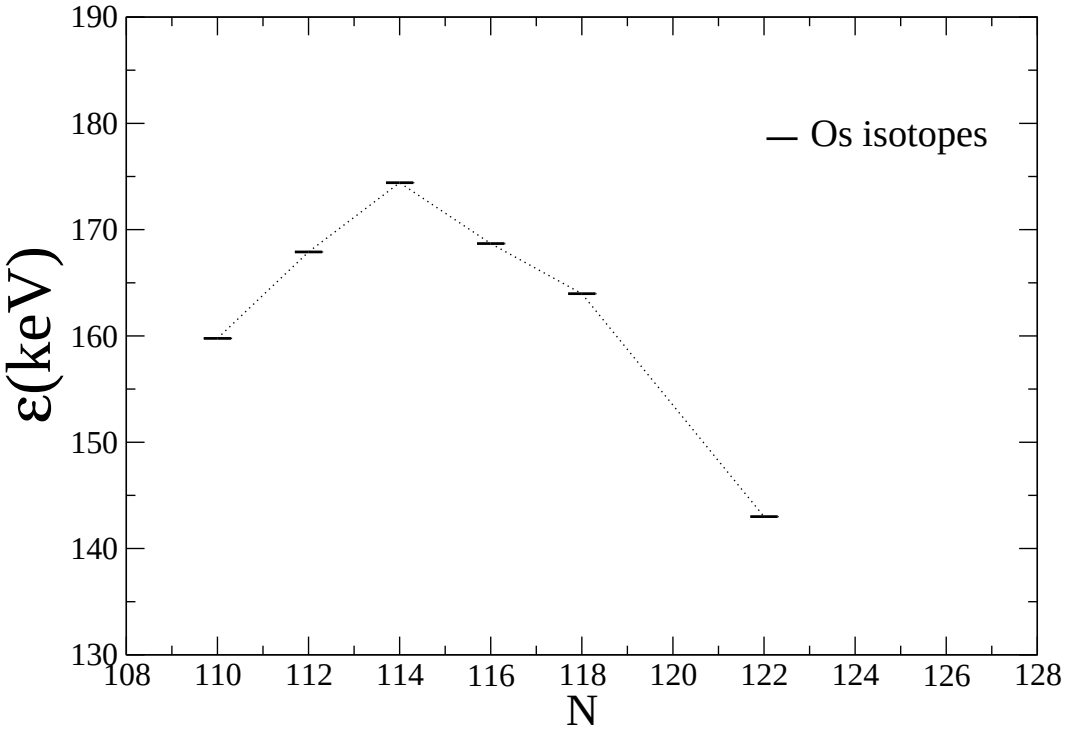

Figure 4.30: Calculated anharmonicity values ε for Osmium isotopes with $N = 110 - 122$.

$$\varepsilon = E(4_1^+) - \left(2 \times E(2_1^+)\right) \tag{4.7}$$

where $E(2_1^+)$ and $E(4_1^+)$ are the excitation energies of the first 2^+ and 4^+ excited states respectively. By using the $E(2_1^+)$ data, information about the collective character of the nuclei can be inferred. For the Osmium isotopes, the yrast 2^+, 4^+, 6^+ and $6^+_{Th.}$ energies increase with increasing neutron number, N, while the excitation energy of the $I^\pi = 2_2^+$ decreases up to $N = 116$ and increases for heavier N values, as shown in figure 4.29. Similarly, the anharmonicity parameter, ε, increases with N until $N = 114$ and decreases for heavier N values (see figure 4.30), while the ratio of $\varepsilon/E(2_1^+)$ decreases with N for both Tungsten and Osmium isotopes (see figure 4.31).

4.8.5 $E(4_1^+)/E(2_1^+)$ systematics

The $E(4_1^+)/E(2_1^+)$ energy ratio ($R_{4/2}$) of the excitation energies of the yrast $I^\pi = 4^+$ and $I^\pi = 2^+$ states is related to the collectivity of the nuclear system [25]. For even-even nuclei this ratio has a value of 2.00 for the perfect harmonic quadrupole vibrator

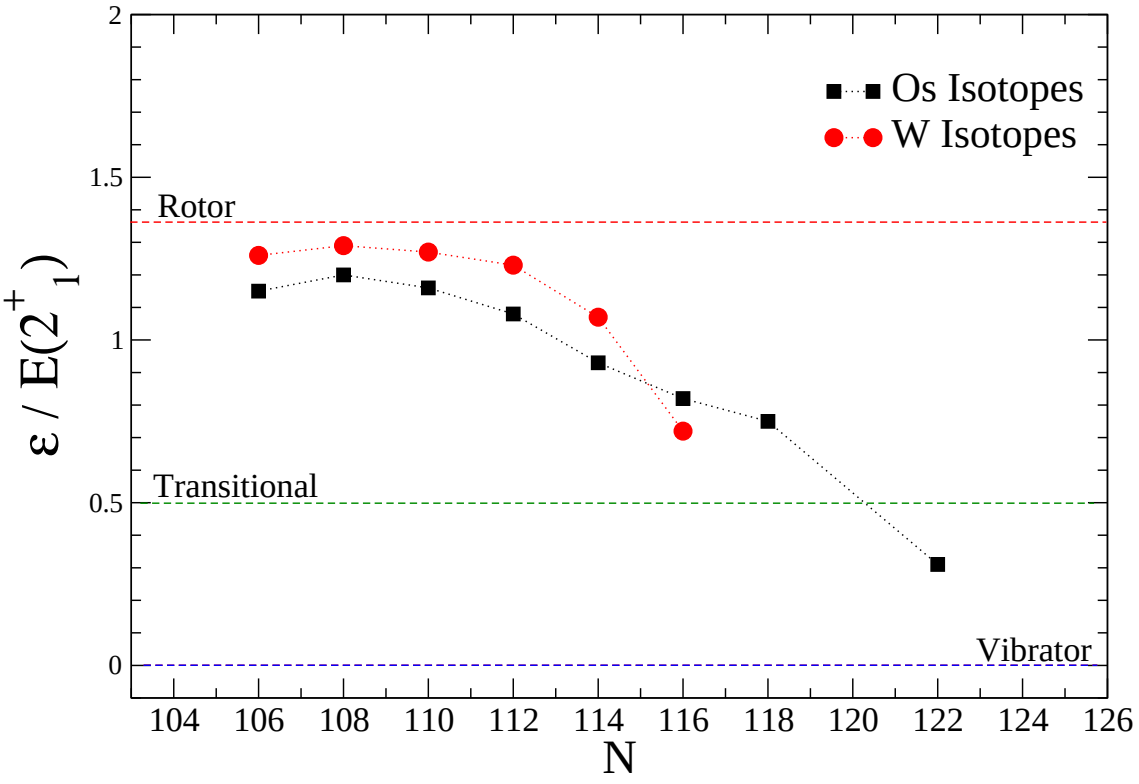

Figure 4.31: The ratio of the calculated anharmonicity ε values normalised to the excitation energy of the yrast state 2^+, $(\varepsilon/E(2_1^+))$ for Osmium isotopes with N=110-122. [23].

[12, 101] and idealized value of $R_{4/2}$=3.33 for a perfect symmetric rotor [12, 102]. Its has a value of $R_{4/2}$=2.5 for a γ-soft rotor [103]. Figure 4.32 shows the ratio $R_{4/2}$ versus N for even-even Hf-Hg ($Z = 72 \rightarrow 80$) nuclei between $N = 104$ and $N = 122$ [23]. For Os isotopes the ratio of $R_{4/2}$ smoothly decreases with N. The experimental ratio of $R_{4/2}$ for ^{194}Os is approximately 2.7, suggesting that ^{194}Os is a transitional, or γ-soft nucleus.

4.8.6 $1/E(2_1^+)$ systematics

For many new exotic nuclei often only the excitation energy of the first 2^+ state is measured. In general, the value of $E(2_1^+)$ decreases as the number of the valence nucleons increases [104], which is opposite to the magnitude of the $R_{4/2}$ ratio. Therefore, systematics of the inverse of the first 2^+ state $(1/E(2_1^+))$ should follow a similar behaviour to that of $R_{4/2}$ ratio. Cakirli and Casten [105] recently showed that by us-

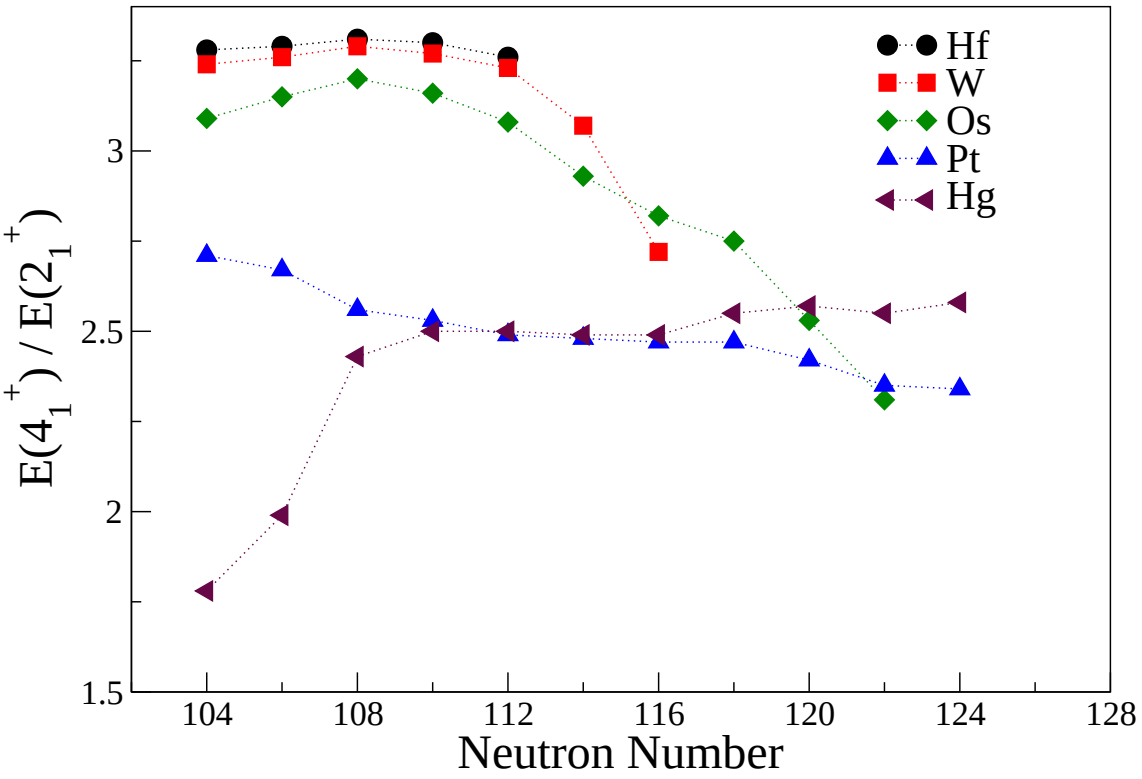

Figure 4.32: Experimental ratio of the excitation energies of the yrast $I^\pi = 4^+$ and $I^\pi = 2^+$ states ($R_{4/2}$) for even-even Hf-Hg ($Z = 72 \rightarrow 80$) nuclei between $N = 104$ and $N = 122$ [23].

ing the empirically derived observables of $R_{4/2}$ ratio and $1/E(2_1^+)$, subshell closures in different regions of the nuclear chart could be identified. Figure 4.33 shows the experimental values of $1/E(2_1^+)$ for even-even Hf-Hg ($Z = 72 \rightarrow 80$) nuclei between $N = 104$ and $N = 122$, these data taken from Ref. [23]. For Os isotopes the ratio of $1/E(2_1^+)$ smoothly decreases as N increases.

4.8.7 $E(2_2^+)/E(2_1^+)$ systematics

The $E(2_2^+)/E(2_1^+)$ energy ratio has been used to infer regions of prolate-oblate shape transitions [93]. Systematics of the $E(2_2^+)/E(2_1^+)$ energy ratios versus N for even-even Hf-Hg ($Z = 72 \rightarrow 80$) nuclei between $N = 104$ and $N = 122$ are shown in figure 4.34 [23]. The neutron number $N = 116$ appears to be a transitional point for Os isotopes, which indicate the maximum γ-softness in this isotopic chain.

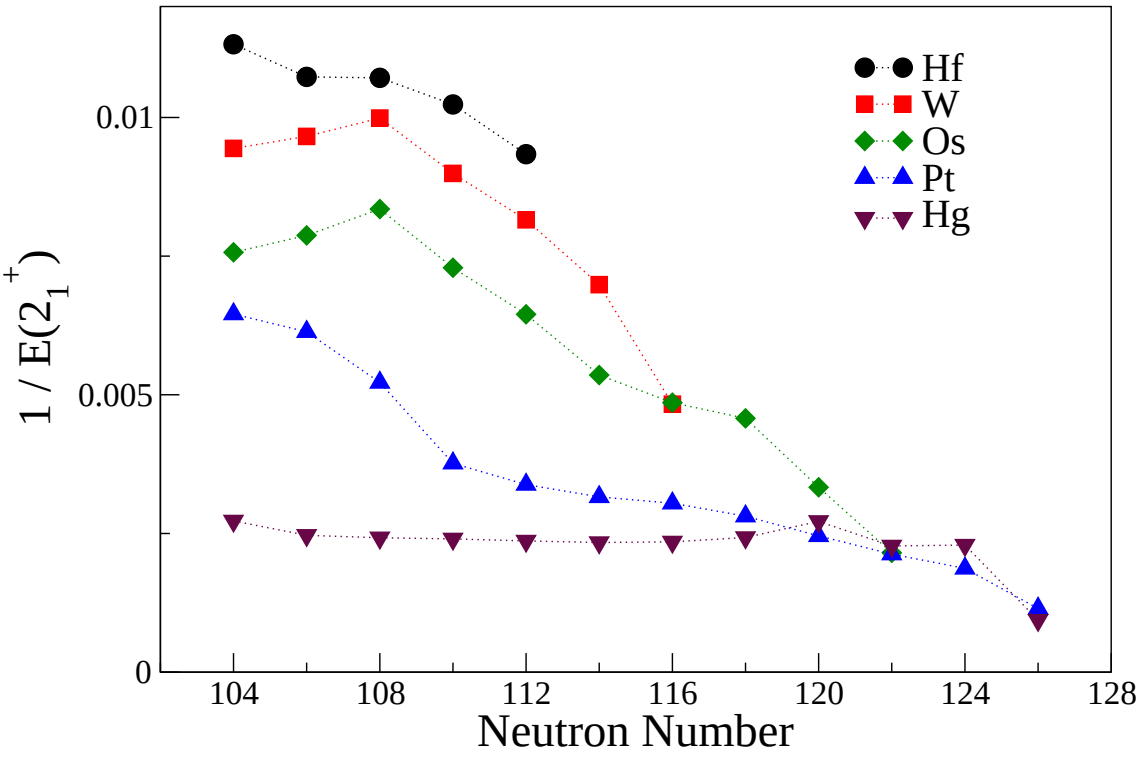

Figure 4.33: The experimental values of $1/E(2_1^+)$ for even-even Hf-Hg ($Z = 72 \rightarrow 80$) nuclei between $N = 104$ and $N = 122$ [23].

4.8.8 Deformation systematics

In $A \sim 190$ region, for even-even Hf-Pt ($Z = 72 \rightarrow 78$) nuclei, the lighter isotopes are prolate deformed and by adding more and more neutrons the shape becomes oblate [11, 12]. As the closed shell at $N = 126$ is approached, the shape of the nuclei is predicted to be become spherical [14, 13]. For the prolate-oblate transition region, the nuclei have a potential with similar energy minima corresponding to prolate and oblate shapes [8]. Figure 4.35 shows the potential energy plots as a function of β deformation (axial quadrupole moment Q_{20}) for the $_{70}$Yb, $_{72}$Hf, $_{74}$W, $_{76}$Os and $_{78}$Pt isotopes with neutron numbers $N = 110 \rightarrow 122$ [22]. The axially symmetric quadrupole moments is equivalent to $Q_{20} > 0$ for prolate and $Q_{20} < 0$ for oblate shapes respectively, while the γ deformations are equivalent to $\gamma = 0°$ for prolate and $\gamma = 60°$ for oblate shapes respectively. From these calculations, ^{194}Os has two competing minima which lie quite close in energy [22].

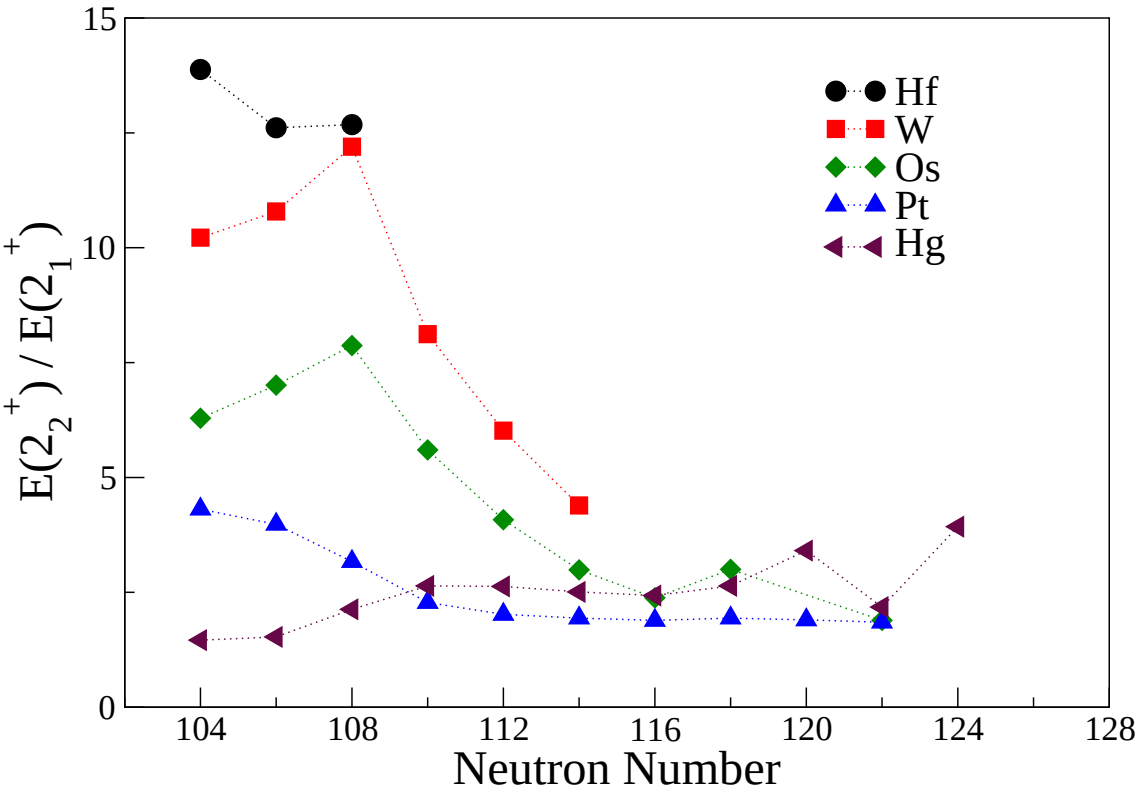

Figure 4.34: The experimental energy ratios of $E(2_2^+)/E(2_1^+)$ versus N for even-even Hf-Hg ($Z = 72 \rightarrow 80$) nuclei between $N = 104$ and $N = 122$ [23].

4.8.9 Total Routhian Surface (TRS) calculations

A further method used to predict the ground state configurations of Os isotopes are Total Routhian Surface calculations (TRS) using the prescription described in Refs. [106, 107, 108]. These have been performed for the ^{190,192,194,196}Os isotopes, corresponding to neutron numbers $N = 114 - 120$. The results of these calculations are shown in figure 4.36, which is taken from Ref. [94]. In these calculations the potential energy is shown as a function of β deformation and the γ degree of freedom. A value of $\gamma = 0°$ corresponds to axially symmetric prolate shapes and $\gamma = 60°$ corresponds to axially symmetric oblate shapes. These calculations predict an evolution from γ-soft prolate potential at ^{190}Os to a well defined oblate shape for ^{196}Os. In case of ^{194}Os, there are both oblate and prolate γ-soft minima [94] (i.e. competing prolate and oblate shapes), but the overall potential is rather shallow in the γ-plane.

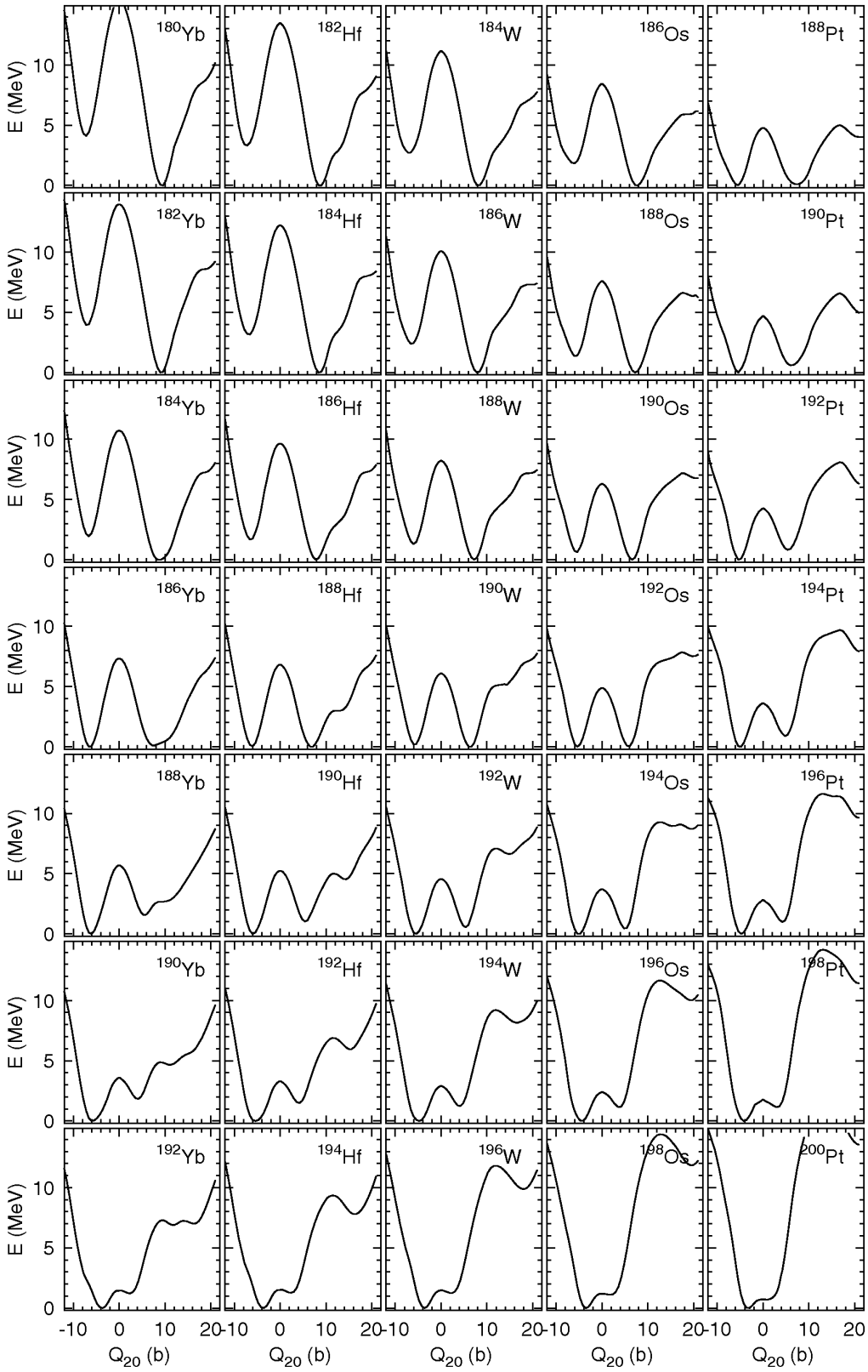

Figure 4.35: Potential energy plots as a function of β deformation (axial quadrupole moment Q_{20}) for $_{70}$Yb, $_{72}$Hf, $_{74}$W, $_{76}$Os and $_{78}$Pt isotopes with neutron numbers $N = 110 \rightarrow N = 122$. These calculation were taken from Ref. [22].

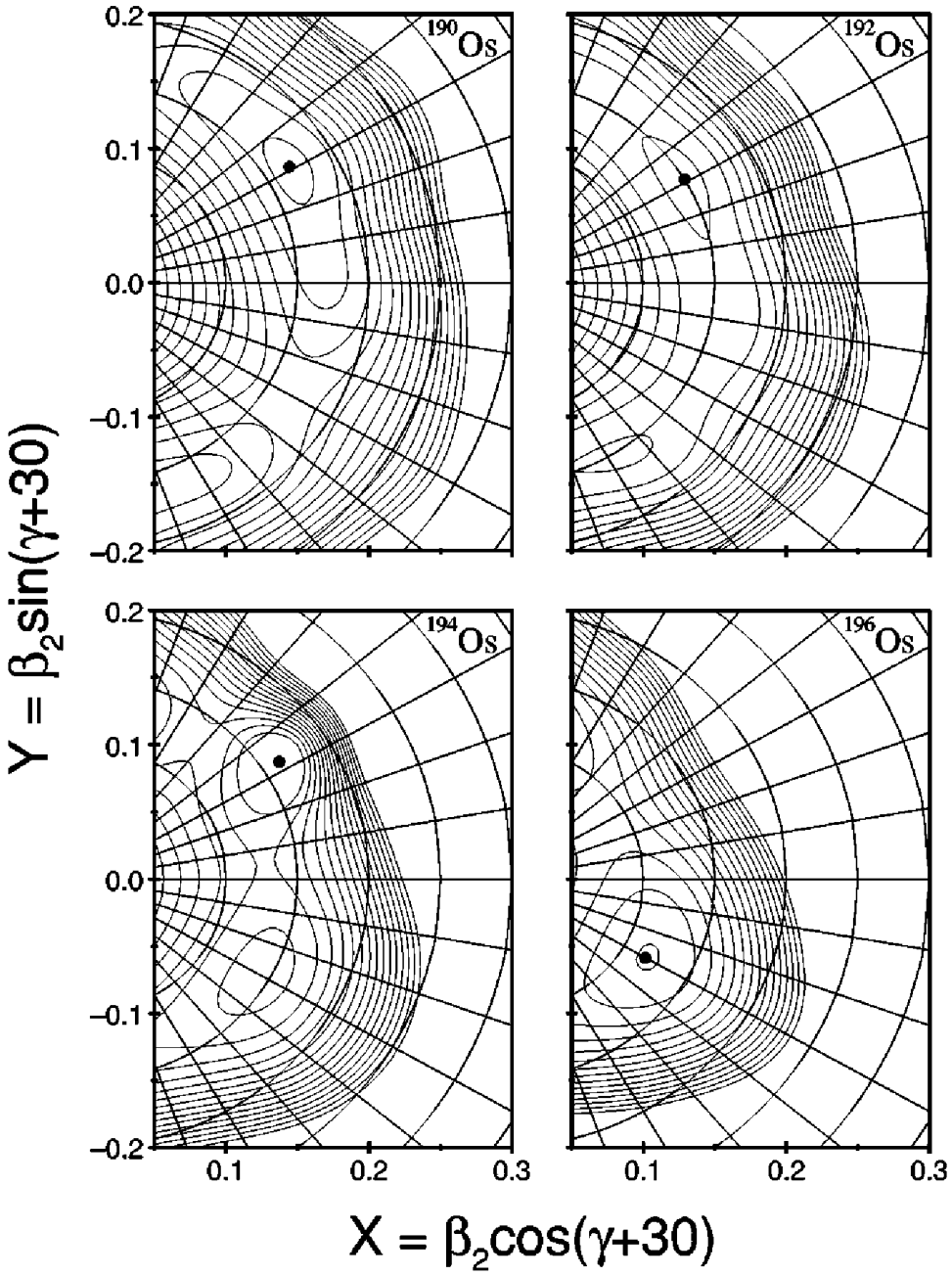

Figure 4.36: Total Routhian Surface calculations (TRS) for the ground state configurations of Osmium isotopes: $^{190}_{76}$Os with β_2=0.17; $^{192}_{76}$Os with β_2=0.15; $^{194}_{76}$Os with β_2=0.16 and $^{196}_{76}$Os with β_2=0.12. The energy contours in this figure are separated by 200 keV, this figure is taken from Ref. [94].

4.8.10 Mean field calculations

The evolution of the ground state shape of Yb, Hf, W, Os and Pt isotopes has been studied recently with neutron numbers ranging from $N = 110 \rightarrow N = 122$ using a Skyrme Hartree-Fock puls BCS pairing approach [22]. These calculations were performed including the γ degree of freedom, and the results are shown in figure 4.37. From these, general conclusions can be extracted obtained about the predicted shape evolution in this region of the chart. These are *(i)* increasing the proton number Z for fixed N drives the corresponding nuclei toward triaxiality [22]; and *(ii)* by increasing N for fixed Z, there is a transition from prolate to oblate shapes. At $N = 116$ and $Z = 70$ (^{186}Yb), there is a sharp transition from a prolate ($N < 116$) to an oblate ($N > 116$) ground state. In case of the Os isotopes (higher values of Z), the ground state is already triaxial or γ-soft and remains so up to $N = 122$. These conclusions are consistent with other theoretical calculations using different interactions [11, 19, 94, 98, 109].

4.9 Summary of ^{194}Re $\rightarrow$ ^{194}Os decay study

The results indicate that there is likely to be (at least) three β-decaying states from ^{194}Re with three different half-lives which feed the:
(1) 0_2^+ state and direct to the 0^+ ground state of ^{194}Os with $T_{1/2}$=7(1) s.
(2) (11^+) high spin state in ^{194}Os ($T_{1/2}$=21(6) s).
(3) (6^+) yrast state in ^{194}Os ($T_{1/2}$=100 s).

MQP calculations assuming axial symmetry give a number of possible prolate (high-spin) and oblate (low-spin) candidate configurations for these β^--decaying states based on Nilsson configurations. $E(4_1^+)/E(2_1^+)$, $1/E(2_1^+)$ and $E(2_2^+)/E(2_1^+)$ systematics for ^{194}Os are consistent with a rather γ-soft nucleus as predicted by TRS and HF calculations.

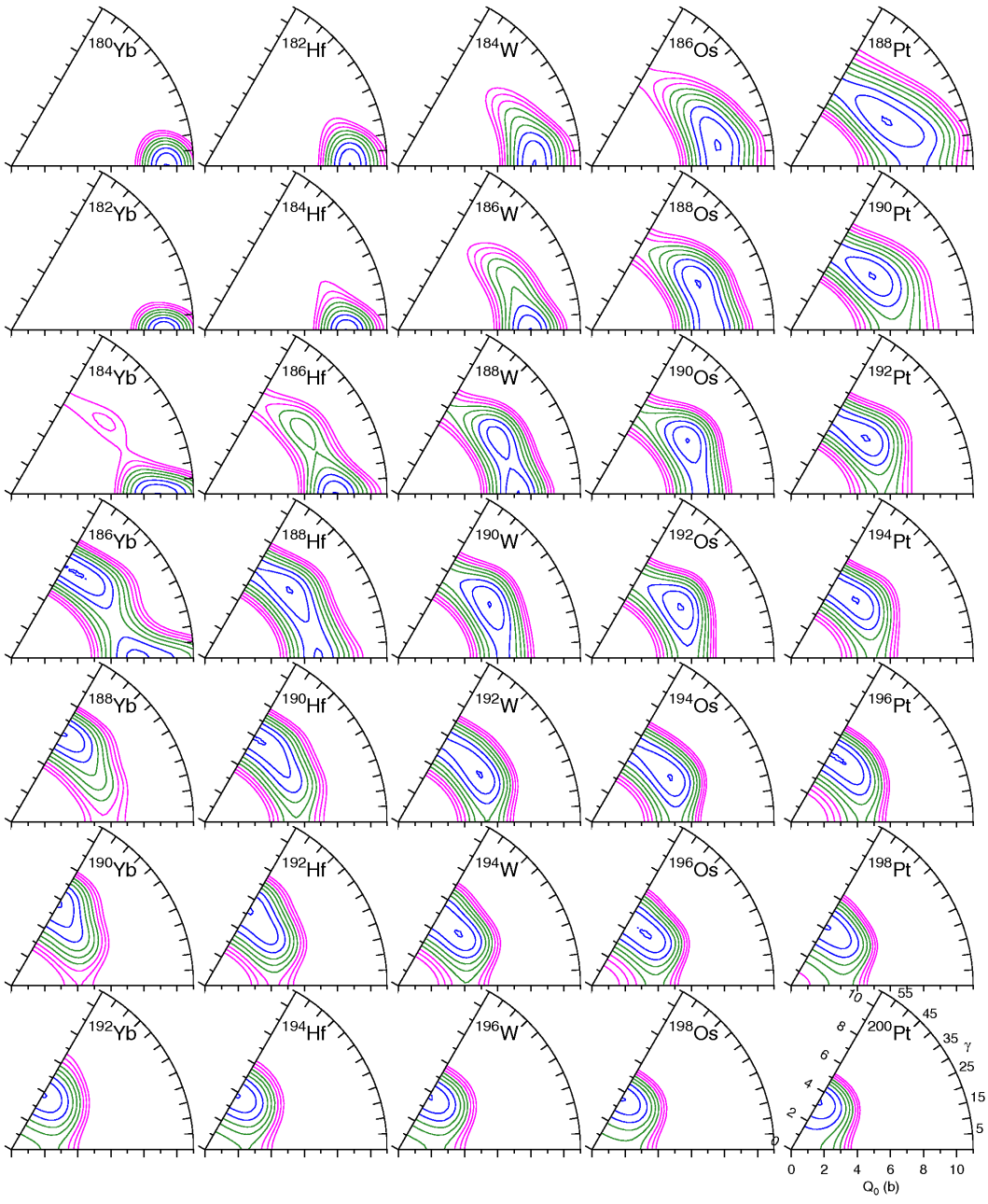

Figure 4.37: Potential energy surfaces as a function of β and γ deformations for the $_{70}$Yb, $_{72}$Hf, $_{74}$W, $_{76}$Os and $_{78}$Pt isotopes with neutron numbers $N = 110 \rightarrow N = 122$. This calculations were taken from Ref. [22].

Chapter 5

Isomeric states in $N = 128$ isotones

5.1 Introduction

In this chapter, the production and structural investigation of the heavy neutron-rich nuclei with $N > 126$ and $Z < 82$ are presented. Specifically, experimental details and results of the $N = 128$ isotones, ^{208}Hg and ^{209}Tl are reported.

5.2 Experimental details

Heavy neutron-rich nuclei were populated via a relativistic energy projectile fragmentation reaction. The primary ^{238}U beam at an energy of E/A =1 GeV was provided by the SIS-18 accelerator at GSI. The maximum primary beam intensity was $\sim 10^9$ ions/spill. The $\sim$ 2 s long spills were separated by $\simeq$ 2 s long periods without beam. The ^{238}U ions impinged on a target composed of 2.5 g/cm^2 ^{9}Be + 223 mg/cm^2 Nb. The Nb foil was used to increase the electron stripping efficiency for the reaction products. The nuclei of interest were selected and identified in flight on an event-by-event basis by the GSI FRagment Separator (FRS) [38]. Figure 5.1 shows a schematic of the detector configuration at the final focal plane of the GSI Fragment Separator used in the April 2008 experiment.

The FRS was optimised for the transmission of $^{205}_{78}$Pt$_{127}$ ions. Compared to previous experiments [14, 81] there were some improvements in the FRS detector setup, including: *(i)* Time Projection Chambers (TPC) were used to track the ions by measuring the X and Y position at both in the S2 and S4. The previous standard setup

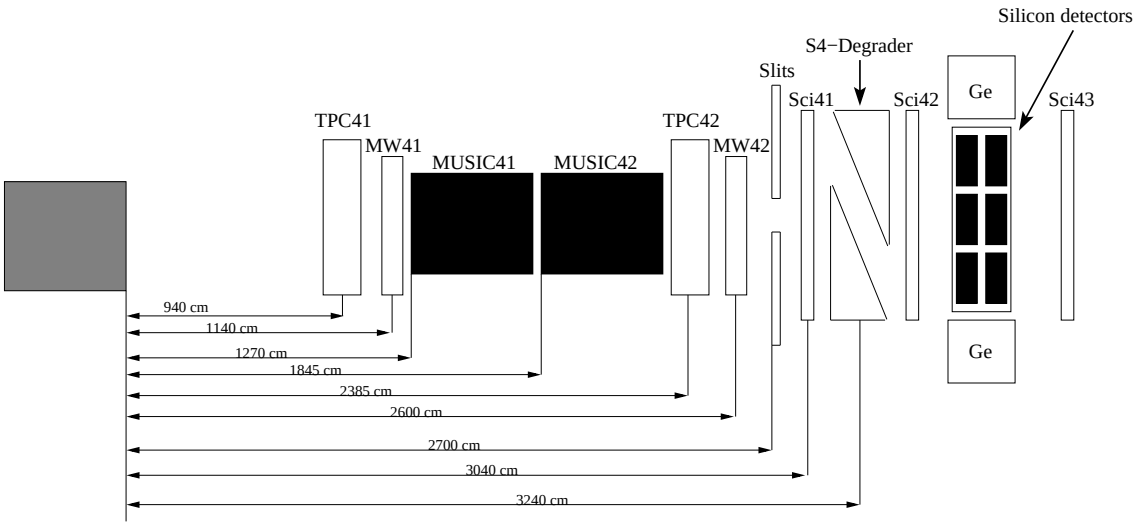

Figure 5.1: Schematic of the detector configuration at the final focal plane of the GSI Fragment Separator used in the April 2008 experiment. Six DSSSDs (black boxes) were used in this particular experiment. TPC=Time Proportional Chamber detectors; MW= MultiWire detectors; Sci= Scintillator detectors; MUSIC= MUlti Sampling Ionising Chamber detectors. The secondary ions were transmitted from left to right on this schematic. The label "4"indicates that the detectors are placed at the final focal plane.

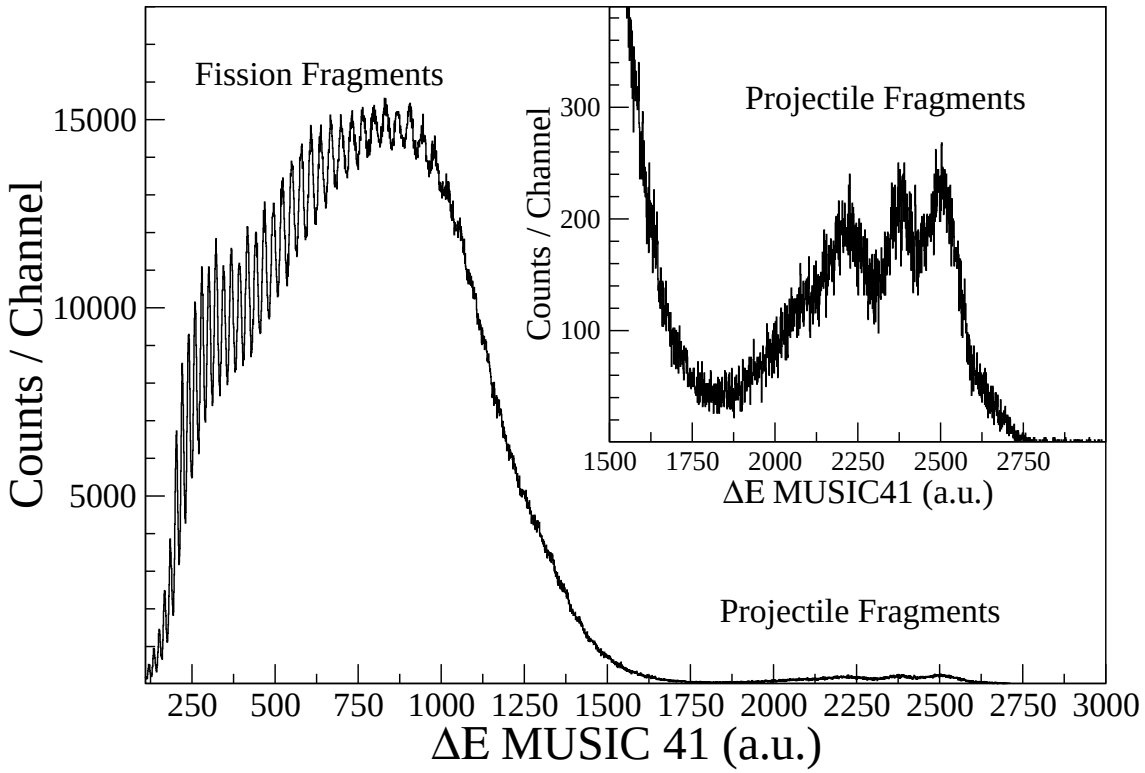

Figure 5.2: Energy loss measurements in the MUSIC41 detector which shows the transmitted fission projectile fragments for the ^{205}Pt setting.

used slower Multiwire (MW) proportional chambers for tracking at S4 and a single scintillator detector to obtain the ion position at S2. The high rate acceptance of TPCs also allowed tracking at S2, which was previously not standard in the FRS set up. *(ii)* An automatic correction for pressure change of the MUlti Sampling Ionization Chambers (MUSIC) was also incorporated.

5.3 Identification of ^{208}Hg and ^{209}Tl isomers

A cocktail of the secondary beams was created following the interaction of the ^{238}U primary beam with the ^{9}Be target at the entrance of the FRS. The same techniques of particle identification were used to identify the nuclei of interest as described previously in Chapter 4. The energy loss in the MUSIC41 and the scintillator Sci41 detectors for the ^{205}Pt centred setting are shown in figures 5.2 and 5.3 respectively. These were used to identify the projectile and fission fragments. Figures 5.4 and 5.5 show the spectra for the energy loss in MUSIC41 detector versus the energy loss in the Sci42L

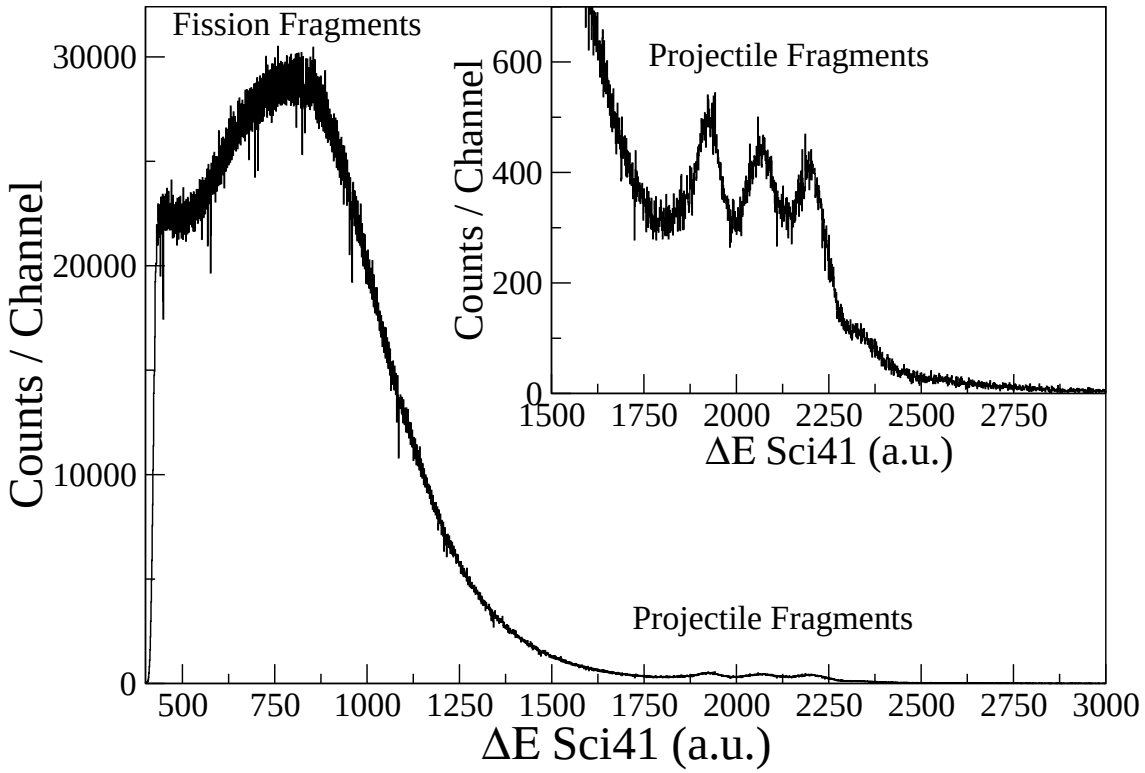

Figure 5.3: Energy loss measurements in the Sci41 detector showing the fission and projectile fragments for the ^{205}Pt setting.

detector and the energy loss in MUSIC41 detector versus the energy loss in the Sci42R detector respectively for ^{205}Pt setting. In these figures, the red line surrounds those events associated with no nuclear reactions before and after the interaction with the S4 degrader. The energy loss of the *veto* detector for the ^{205}Pt setting is shown in figure 5.6; those events after the red line were removed from the final off-line analysed data. The spike at the end of the spectrum arises from a pulser which is connected to detector.

After the production target the magnetic rigidity of the fully stripped nuclei of interest was close to those of the intense He-like primary ^{238}U beam. In order to prevent the high-intensity charge states of the primary beam from reaching and damaging the detectors at the intermediate focal plane (S2), a degrader of thickness 2176 mg/cm^2 Al equivalent was placed at the first, dispersive, focal plane (S1). The FRS was operated in achromatic mode with a wedge shaped degrader at the intermediate focal plane of the separator (S2). This degrader had a total thickness of 2.8 g/cm^2 Al equivalent

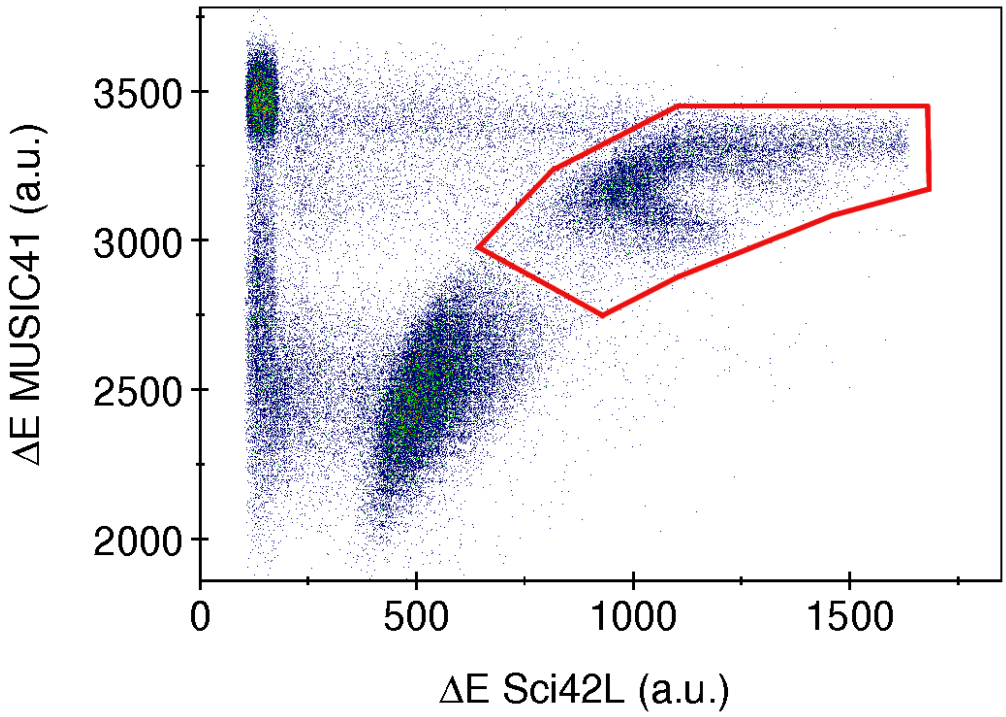

Figure 5.4: Energy loss in the MUSIC41 detector versus the energy loss in the Sci42L detector. The red line surrounds those ions with the same atomic number before and after the interaction with the S4 degrader.

and included a fast scintillator and a Nb stripper to maximise the number of fully stripped (q=Z) nuclei passing through the FRS. According to calculations performed with the GLOBAL code [84] 92.2%, 82.0% and 70.7% of the ^{208}Hg ions were fully stripped leaving the target, the S1 focal plane and S2 focal plane, respectively. The energy loss in MUSIC 42 versus the energy loss in the S2 degrader is shown in figure 5.7, which represents the charge state selection for the ^{205}Pt centred setting. The (red) gate is predominately fully stripped ions with $\triangle q = 0$ while the region defined by the black locus represents the H-like ions with $\triangle q = -1$. Figure 5.8 shows the particle identification plot of ^{205}Pt setting for fully stripped ($\triangle q = 0$) ions. The number of implanted nuclei from the ^{205}Pt centred setting, for fully stripped ($\triangle q = 0$) ions, is given in Table 5.1.

The particle identification for this experiment was confirmed by the observation of the γ-ray decay from previously reported isomeric decays in ^{204}Au [110], ^{205}Au [88, 111]

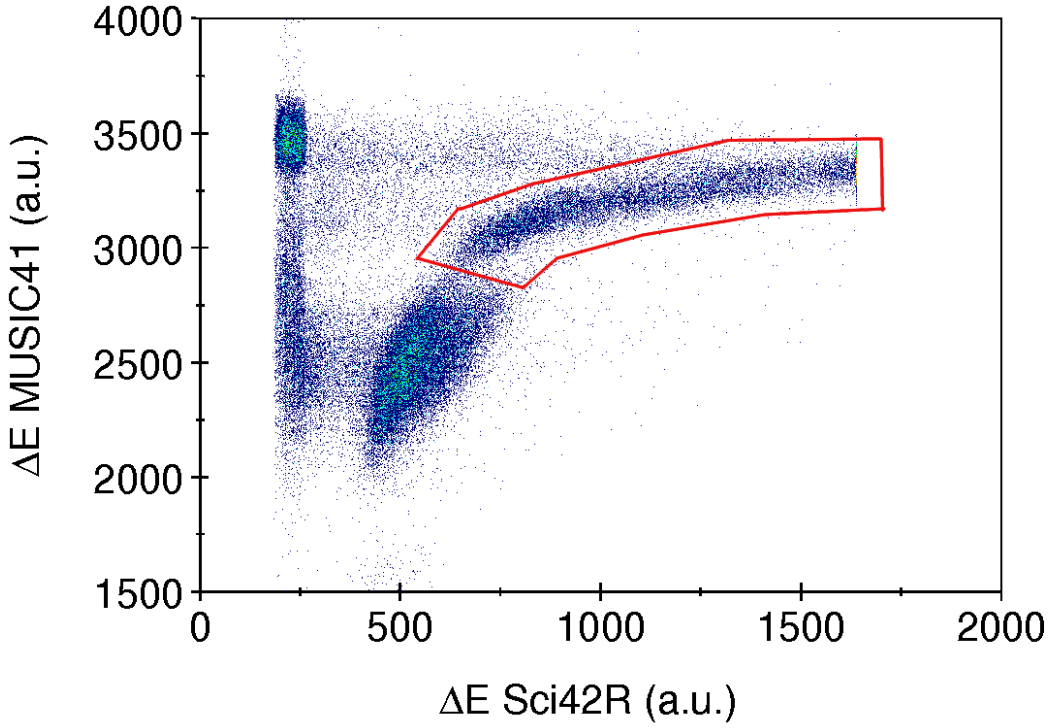

Figure 5.5: Energy loss in the MUSIC41 detector versus the energy loss in the Sci42L detector. The red line surrounds those events associated with "no nuclear reaction" before and after the S4 degrader.

and ^{206}Hg [112]. The γ-ray spectra for the isomeric decays associated with ^{204}Au, ^{205}Au and ^{206}Hg in the present work are shown in figure 5.9.

5.4 Isomeric states in $N = 128$ isotones

5.4.1 ^{208}Hg

Evidence of decays from isomeric states in the $N = 128$ isotones ^{208}Hg and ^{209}Tl is observed in the current work for the first time. Delayed γ rays associated with ^{208}Hg nuclei are shown in figure 5.10(b). Three γ ray transitions with energies 203, 425 and 669 keV, together with characteristic Hg K_α X ray are identified. The three γ-ray transitions are in mutual coincidence as shown in figure 5.11 and have similar apparent decay half-lives within experimental uncertainties. Figure 5.12 shows the time difference between these transitions. The time difference was approximately 50

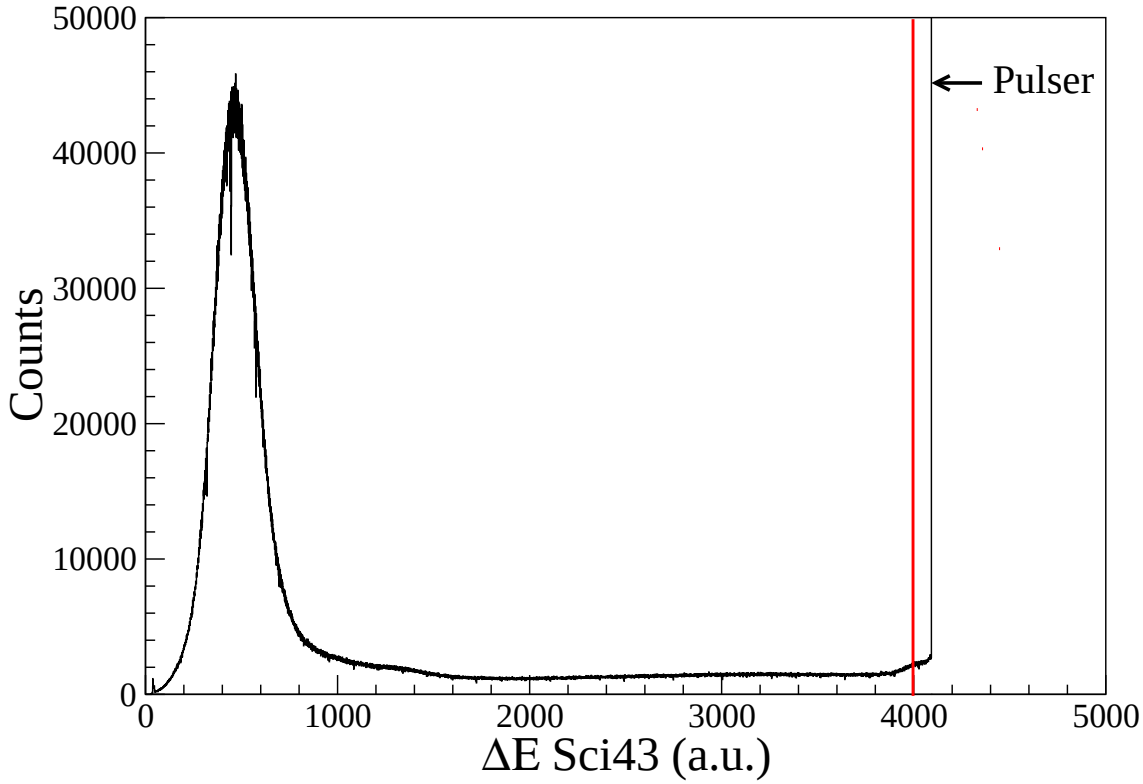

Figure 5.6: Energy loss in the *veto* Scintillator Sci43 for ^{205}Pt setting.

ns which corresponds to the prompt response between germanium detectors in the RISING array, suggesting these transition come from the decay of a single isomer followed by a prompt ($T_{1/2} < 1$ ns) cascade. The measured half-life is $T_{1/2}$=99(14) ns, see figure 5.10(b). The relative γ-ray intensities associated with the isomer in the present work are given in Table 5.2. Assuming that the three γ-ray transitions form a single cascade, the total transition intensities must be equal. Under this assumption, the internal conversion coefficient of the 203 keV transition can be inferred, assuming that it and both the 669 and 425 keV transitions are all of a pure, stretched E2 character. From these intensity balance arguments, the internal conversion coefficient for the 203 keV transition is thus inferred to be $\alpha_{Exp.}$=0.36(6). This compares to the theoretical value for a 203 keV E2 transition in ^{208}Hg of $\alpha_{The.}$=0.37(6), see Table 5.3 for details. The intensity of the measured K_α X-rays following the conversion electron emission is also in agreement with the fluorescence yield expected for a 203 keV E2 internal conversion branch in this decay [113].

Table 5.1: Number of implanted nuclei for different neutron-rich species populated in the ^{205}Pt setting for fully stripped. These values all assume fully stripped nuclei transmitted through the FRS only.

Number	Nucleus	Number of Nuclei	Ions/Hour
1	$^{208}_{81}$Tl	147	2.26
2	$^{209}_{81}$Tl	616	9.48
3	$^{210}_{81}$Tl	343	5.28
4	$^{211}_{81}$Tl	234	3.6
5	$^{206}_{80}$Hg	587	9.03
6	$^{207}_{80}$Hg	612	9.42
7	$^{208}_{80}$Hg	699	10.75
8	$^{209}_{80}$Hg	243	3.74
9	$^{204}_{79}$Au	877	13.49
10	$^{205}_{79}$Au	677	10.42
11	$^{206}_{79}$Au	276	4.25
12	$^{207}_{79}$Au	225	3.46
13	$^{208}_{79}$Au	302	4.65

5.4.2 ^{209}Tl

There is also evidence for a $\sim$ 100 ns isomeric decay in ^{209}Tl in the current work. Discrete γ rays with energies of 138, 323 and 661 keV, together with characteristic Tl K_α X rays have been identified, see figure 5.10(c). The 138, 323 and 661 keV transitions are in mutual coincidence, as shown in figure 5.13. They are also prompt ($\triangle$t $<$ 50 ns) with respect to each other, as shown by the time different spectra shown in figure 5.14.

The measured time difference was approximately 50 ns which corresponds to the $FWHM$ of the prompt instrument timing response of the RISING array. This suggests a single isomeric state in ^{209}Tl followed by a prompt ($T_{1/2} < 1$ ns) cascade. No parallel branches are observed in the current work. The measured, relative γ ray intensities for the three transitions observed in ^{209}Tl are given in Table 5.2. As in the ^{208}Hg

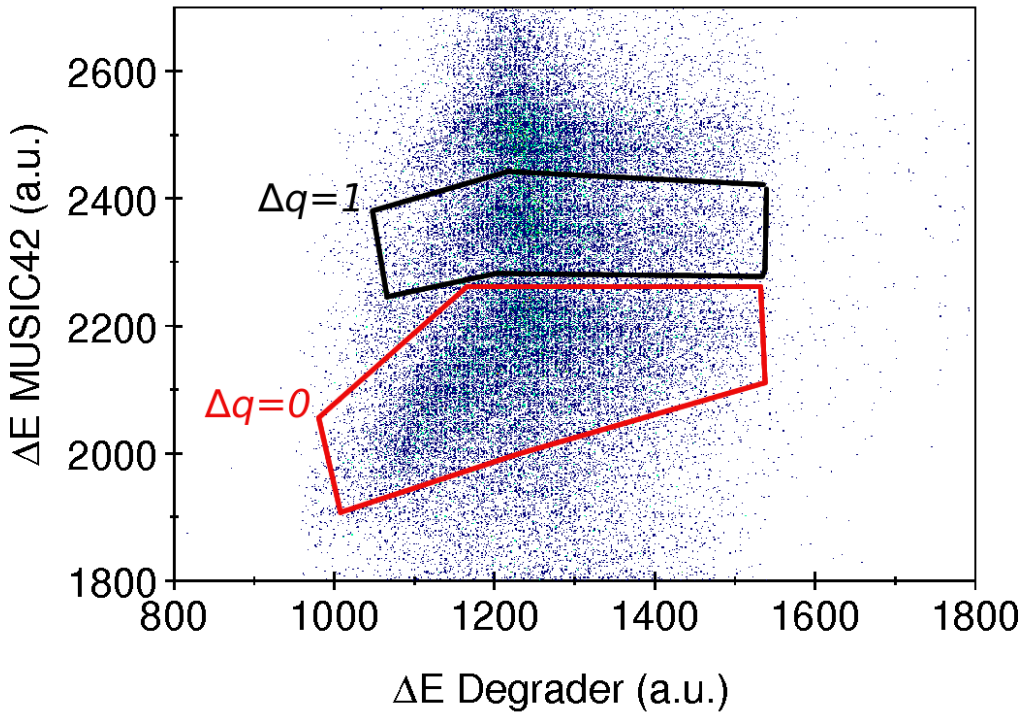

Figure 5.7: Energy loss in the MUSIC42 detector versus the energy loss in S2 degrader, the red gate surrounds the fully stripped ion events, and the black gate the H-like ones.

isomeric decay discussed in the previous section, under the assumption that the three γ-ray transitions form a single cascade with no parallel branches, the total transition intensities must be equal. Under this assumption, the internal conversion coefficient of the 137 keV transition can be inferred, assuming that the 661 and 323 keV decays are both of an E2 character. From these intensity balance arguments, the internal conversion coefficient for the 137 keV transition was deduced to be $\alpha_{Exp.}$=1.54(31). This compares with the theoretical value for a 137 keV stretched E2 transition in the ^{209}Tl of $\alpha_{The.}$=1.64(23), see Table 5.2. The intensity of the K_α X-rays following the conversion electron emission is also in agreement with expectation from the florescent yield following internal conversion. The measured half-life for the isomer decay in ^{209}Tl is $T_{1/2}$=99(11) ns, see figure 5.3(c).

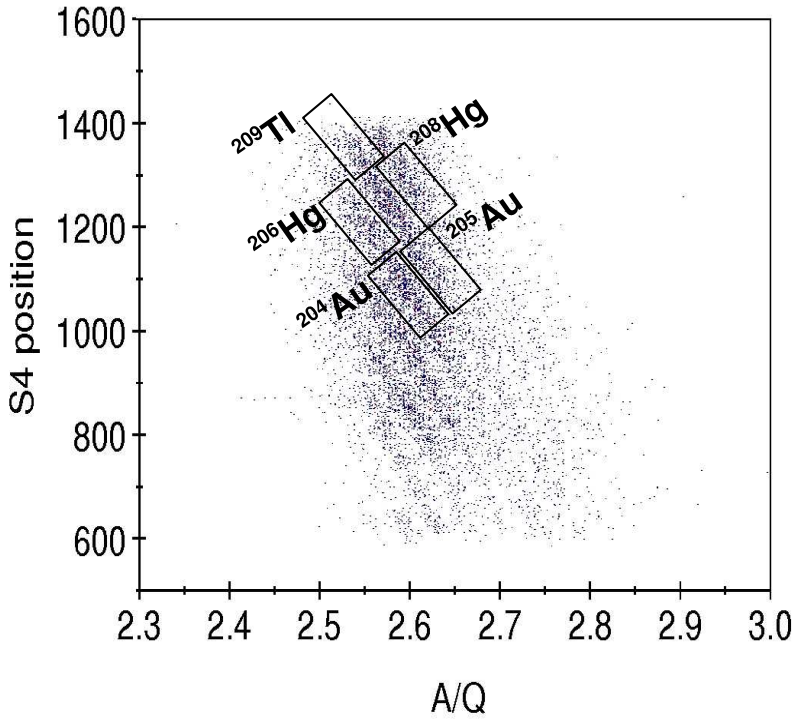

Figure 5.8: Particle identification plot from the ^{205}Pt setting for fully stripped ions ($\triangle q = 0$).

5.5 Discussion of $N = 128$ isotones for $Z \leq 82$

Prior to the current measurement no experimental information was available on the excited states of ^{208}Hg. Excited states of ^{209}Tl were previously studied via the alpha decay of ^{213}Bi and in the (t,α) reaction [34]. The alpha decay of ^{213}Bi populates both the first excited states as well as the ground state of ^{209}Tl [34]. The γ ray depopulating the first excited state was observed at 324 keV [34]. A recent evaluation [35], based on intensity balance measurements in α decay, concludes that this transition has an mixed E2 / M1 character, with a mixing ratio of δ=1.26(16). Six excited states were identified in the (t,α) reaction on a radioactive ^{210}Pb target [34], with an estimated energy uncertainty of 10 keV [37]. The results were described as an odd-proton hole coupled to the ^{210}Pb core [117].

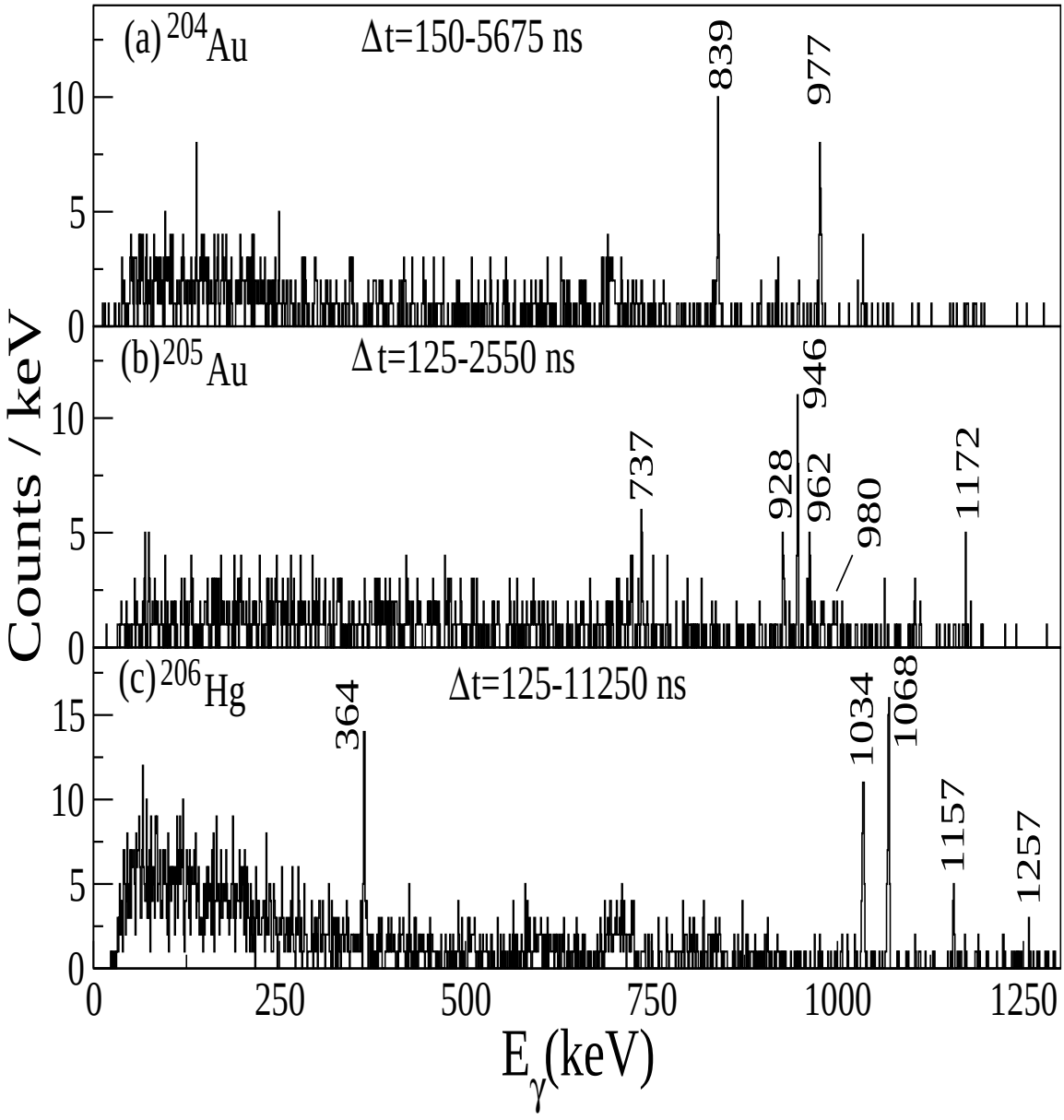

Figure 5.9: γ-ray spectra from isomeric decays identified following the ^{238}U + ^{9}Be fragmentation reaction in the current work. **(a)**: $^{204}_{79}$Au γ rays detected between 150 and 5675 ns after the ion implantation. **(b)**: $^{205}_{79}$Au γ rays observed between 125 and 2550 ns after the implantation. **(c)**: $^{206}_{80}$Hg γ ray detected between 125 and 11250 ns after the implantation.

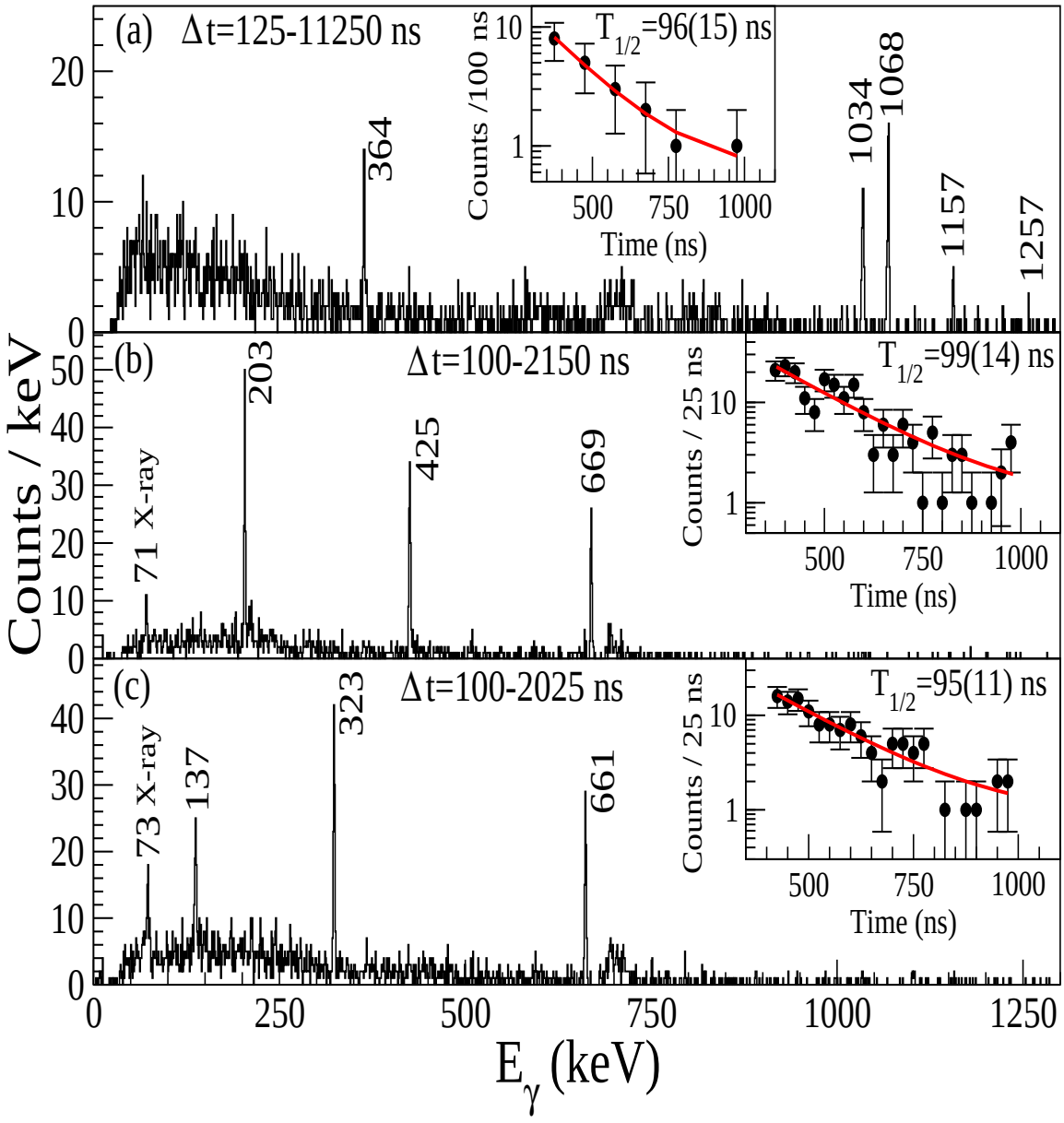

Figure 5.10: γ-ray spectra from isomeric decays in ^{206}Hg, ^{208}Hg and ^{209}Tl measured in the current work. **(a)**: $^{206}_{80}$Hg γ rays detected between 125 and 11250 ns after the implantation. **Inset**: Decay curve associated with the 364 keV γ ray from the current work. **(b)**: $^{208}_{80}$Hg γ rays observed between 100 and 2450 ns after the implantation. **Inset**: Decay curve of the 203, 425, 669 keV γ rays. **(c)**: $^{209}_{81}$Tl γ rays detected between 100 and 1625 ns after the implantation. **Inset**: Decay curve of the 137, 323, 661 keV γ rays. A γ ray with energy of 323 keV in ^{209}Tl was previously reported in References [34, 35].

Table 5.2: Experimental γ ray intensities for transitions in ^{208}Hg and ^{209}Tl from the current work.

Nucleus	γ-ray Energy (keV)	Counts	Absolute Photopeak Efficiency	Conversion Coefficient[a]	I_γ	Total Intensity
^{208}Hg	203	94(10)	0.27	0.3710	77(11)	104(15)
	425	91(10)	0.18	0.0405	107(16)	110(16)
	669	62(8)	0.13	0.0138	100(16)	100(16)
^{209}Tl	137	45(9)	0.30	1.5960	42(9)	110(25)
	323	79(9)	0.22	0.0877	100(15)	111(17)
	661	48(8)	0.14	0.01484	96(19)	100(19)

[a] Electron conversion coefficient for a pure E2 transitions, taken from Ref. [56].

5.5.1 Shell model calculations

In order to obtain a quantitative understanding of the underlying single-particle structure of the excited states in the $N = 128$ isotones ^{208}Hg and ^{209}Tl, shell-model calculations using the OXBASH code [118] have been performed. The shell model single-particle space consisted of the proton orbitals $2d_{5/2}$, $2d_{3/2}$, $3s_{1/2}$, $1h_{11/2}$ below the Z=82 closed shell, and the neutron orbitals $2g_{9/2}$, $1i_{11/2}$ $1j_{15/2}$ above the closed N=126 shell. Therefore, no core excitations across the ^{208}Pb double shell closure were allowed in these calculations. The single proton-hole and neutron-particle energies were taken from the experimental spectra of ^{207}Tl and ^{209}Pb, respectively. The Two-Body interaction Matrix Elements (TBME) were taken from Ref. [119]. These were based on the Kuo-Herling realistic interaction [120] for proton-proton and neutron-neutron TBME derived from a free nucleon-nucleon potential with core polarisation renormalisation due to the finite model space. The proton-neutron interaction is the bare H7B G-matrix [121] without core polarisation as justified in Ref. [119]. The only additional correction made in the present work is a shift of +40 keV to the $(\nu g_{9/2})^2_{8+}$ two-body matrix element to obtain the correct experimental ordering of the spin/parity 6^+ and 8^+ states sequence in ^{208}Hg. As a first step the excited states of the two-proton

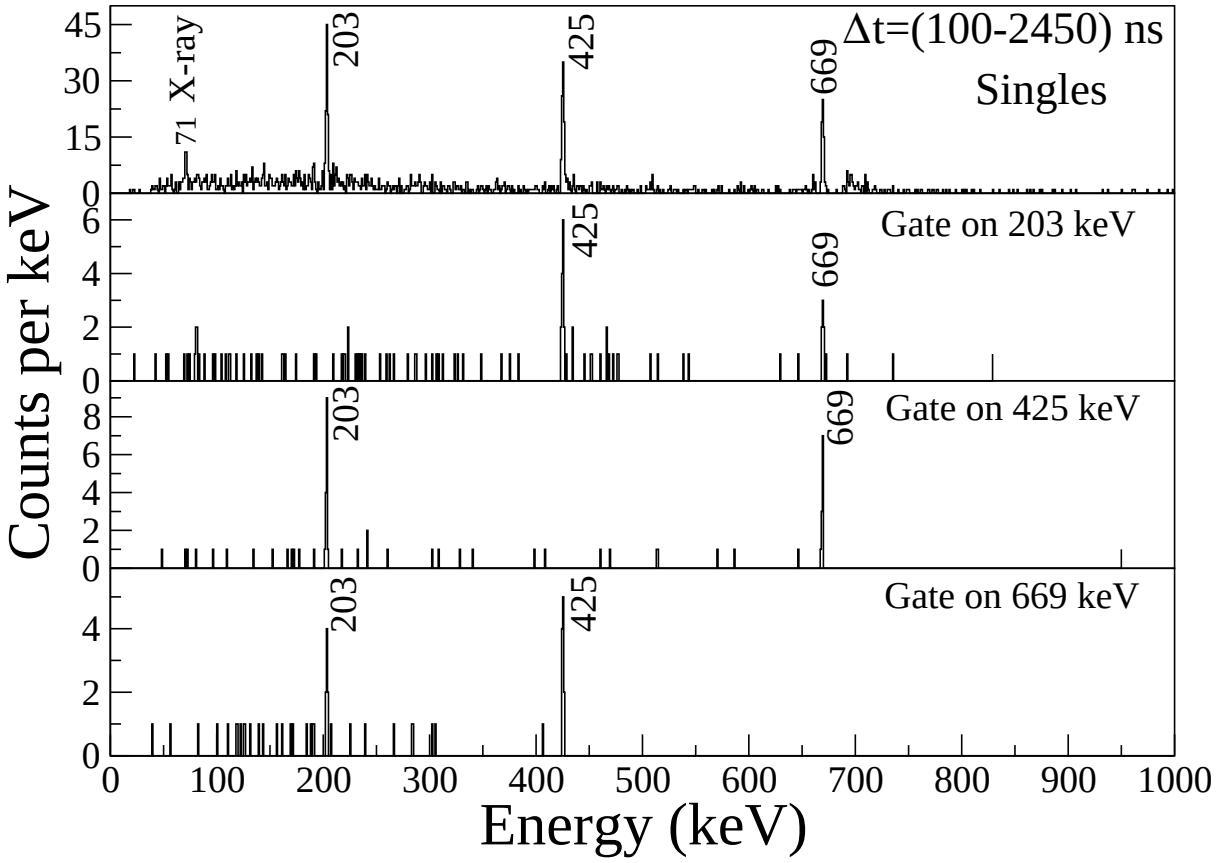

Figure 5.11: Singles and coincidence γ-ray spectra gated on ^{208}Hg. The ion-γ time condition is (100-2450) ns for each of these spectra. **(a)**: Gate on 204 keV. **(b)**: Gate on 425 keV. **(c)**: Gate on 669 keV.

hole ^{206}Hg and the two-neutron particle ^{210}Pb nuclei were calculated. The partial level schemes obtained in the current work together with the predominant single-particle configurations are shown in figure 5.15.

^{208}Hg calculations

The ^{208}Hg nucleus has two-proton holes and two-neutron particles outside the double magic $^{208}_{82}Pb_{126}$ core. The results of the shell model calculations are shown in figure 5.8. The comparison with the experimental information suggest an $I^{\pi}=8^{+}$ assignment for the observed isomer. The three observed transitions at 669, 425 and 203 keV are then assumed to correspond to the $6^{+} \rightarrow 4^{+} \rightarrow 2^{+} \rightarrow 0^{+}$ decay sequence. It is assumed here that the $8^{+} \rightarrow 6^{+}$ transition directly depopulating the isomer is not observed due to the high conversion coefficient (and low efficiency of the detector) at

Table 5.3: Theoretical and experimentally inferred conversion coefficient (E2) values for ^{208}Hg and ^{209}Tl, theoretical values are taken from BrIcc v2.2b website.

Nucleus	Energy keV	I_γ	$\alpha^a_{The.}$	$\alpha_{Exp.}$	$\langle x \rangle^b$
^{208}Hg	203	77(11)	0.371(6)	0.447(93)	$\alpha(203)=$ 0.36(6)
	425	107(16)	0.0405(6)		
	203	77(11)	0.371(6)	0.313(68)	
	669	100(16)	0.01381(20)		
^{209}Tl	137	42(9)	1.642(23)	1.84(50)	$\alpha(137)=$ 1.54(31)
	323	100(15)	0.178(1)^c		
	137	42(9)	1.642(23)	1.35(40)	
	661	96(19)	0.01484(21)		

[a] The conversions coefficient $\alpha_{The.}$ for E2 transitions, are taken from Ref. [56].

[b] $\langle x \rangle$ is the weighted value for the $\alpha_{Exp.}$

[c] This value is taken from Ref. [35] for a mixed M1 / E2 transition transition.

low energies ($E_\gamma < 80$ keV). Each these states are predicted to be of predominantly $\nu g^2_{9/2}$ shell model character. The rather low intensity of the observed K_α line indicates that the energy of this missing transition is below the binding energy of the Hg K electron, i.e. below 83.1 keV. The transition strength extracted from the experiment is slightly larger than the calculated value of $B(E2)$=1.22 W.u., (see Table 5.5). The experimental $B(E2)$ values were calculated by using expression [55, 122].

$$B(E2) = \frac{9523}{T_{1/2}.E^5_\gamma.A^{4/3}} \frac{B_R}{1+\alpha} \tag{5.1}$$

where $T_{1/2}$ is the EM decay half-life in ps, E_γ is transition energy in MeV, A is the mass number, α is the conversion coefficient and B_R is the branching ratio, $B(E2)$ values are in Weisskopf units.

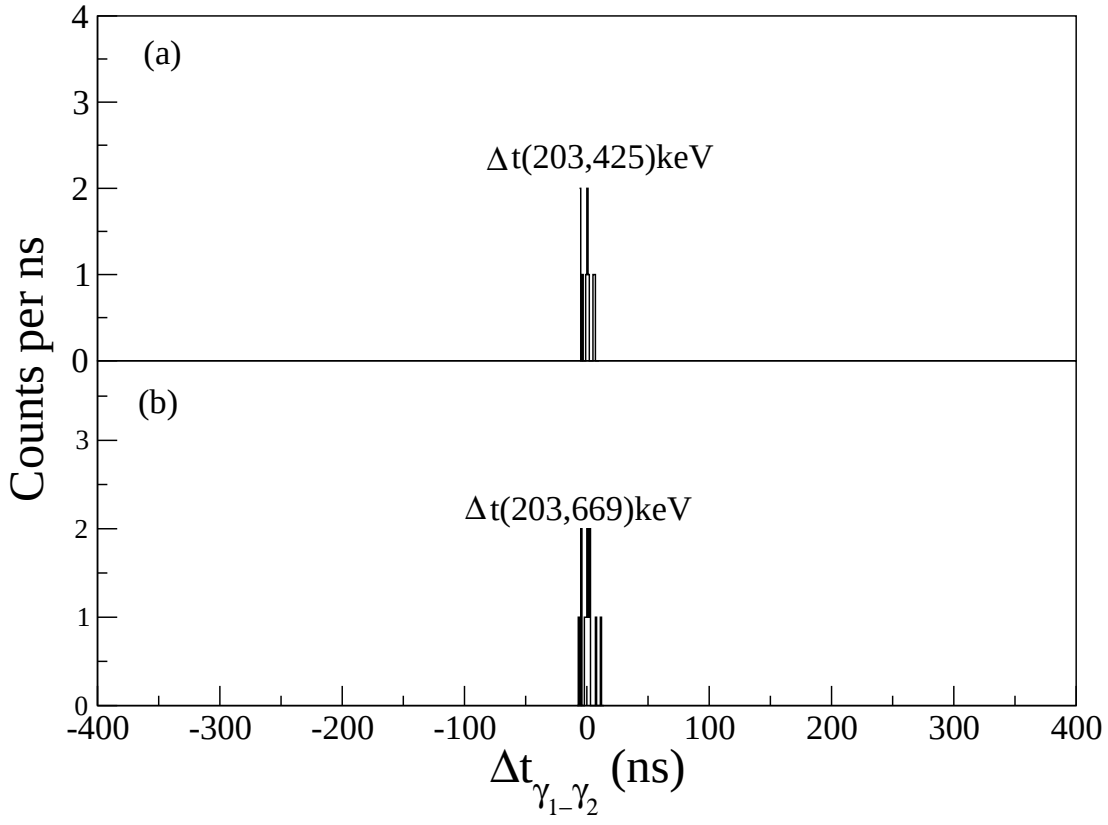

Figure 5.12: γ-ray time difference spectra on ^{208}Hg isomeric, γ-rays showing the prompt coincidence nature of the cascade observed in ^{208}Hg.

^{209}Tl calculations

The $^{209}_{81}\mathrm{Tl}_{128}$ nucleus has one-proton hole and two-neutron particles outside the double magic $^{208}_{82}\mathrm{Pb}_{126}$ core. The results of the shell model calculations performed for the current work are shown in figure 5.9. The calculation suggests a $17/2^+$ isomeric state which would decay via a $17/2^+ \rightarrow 13/2^+ \rightarrow 9/2^+ \rightarrow 7/2^+ \rightarrow 3/2^+ \rightarrow 1/2^+$ sequence. The isomer is predicted to have a predominantly $\nu(g_{9/2})^2_{8+} \otimes \pi s_{1/2}$ character and to decay via a low-energy, (unobserved), E2 transition into the mainly $\nu(g_{9/2})^2_{6+} \otimes \pi s_{1/2}$, I^π=$13/2^+$ state. The $17/2^+ \rightarrow 13/2^+$ decay transition is the analogue of the $8^+ \rightarrow 6^+$ decay in ^{208}Hg. The similar $B(E2)$ transition strengths in the two $N = 128$ nuclei are consistent with this interpretation. The 137 and 661 keV transitions are interpreted as connecting the $13/2^+ \rightarrow 9/2^+$ and $7/2^+ \rightarrow 3/2^+$ states respectively. The expected low energy $9/2^+ \rightarrow 7/2^+$ transition is also not observed in the current work. The low intensity of the observed K_α lines indicates that the energies of both

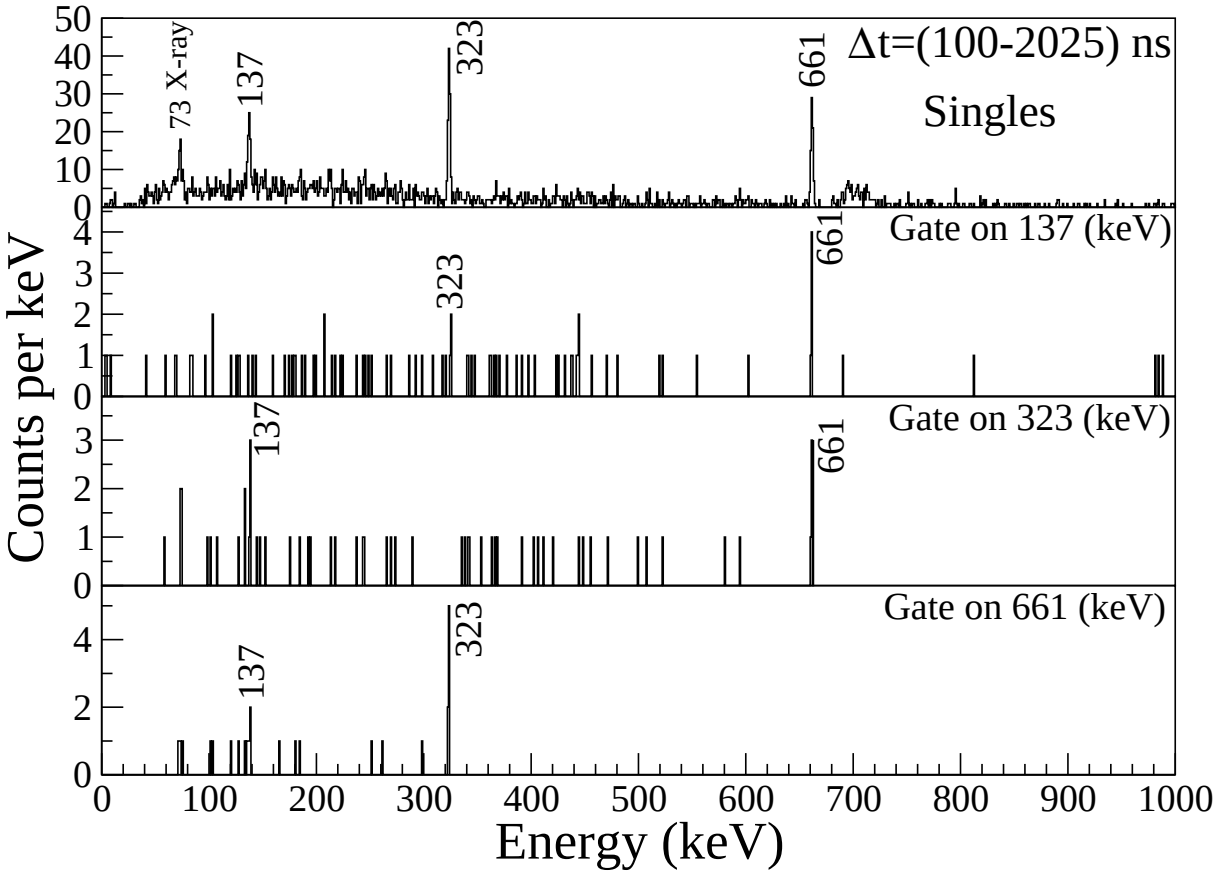

Figure 5.13: Singles and coincidence γ-ray spectra gated on ^{209}Tl and the time gate is (100-1625) ns. **(a)**: Gate on 137 keV. **(b)**: Gate on 323 keV. **(c)**: Gate on 661 keV.

unobserved transitions are below the binding energy of the Tl K electron, i.e. below 85.5 keV.

There is a clear similarity between the low-lying level structure of ^{210}Pb and ^{208}Hg. The excitation energies of the 4^+, 6^+ and 8^+ states are very similar, indicating that the proton admixture into these states in ^{208}Hg is small. However it is notable that the yrast 2^+ state in ^{208}Hg lies 130 keV lower than in ^{210}Pb. This lowering would be caused by mixing the $\pi s_{1/2}d_{3/2}$ configuration (which is the dominant component of the predicted yrast I^π=2^+ wave function in ^{206}Hg) with the $(\nu g_{9/2})^2_{2+}$ configuration. A closer look at the calculated wave functions reveals that the situation is even more complex. The occupation of the $(\nu g_{9/2})^2_{0+}(\pi s_{1/2})^{-2}$ configuration in the ground state is only about 50%. The rest of the strength is made out of different excitations, including neutrons in the $\nu i_{11/2}$ and protons in the $\pi h_{11/2}$ orbitals. The occupancy of

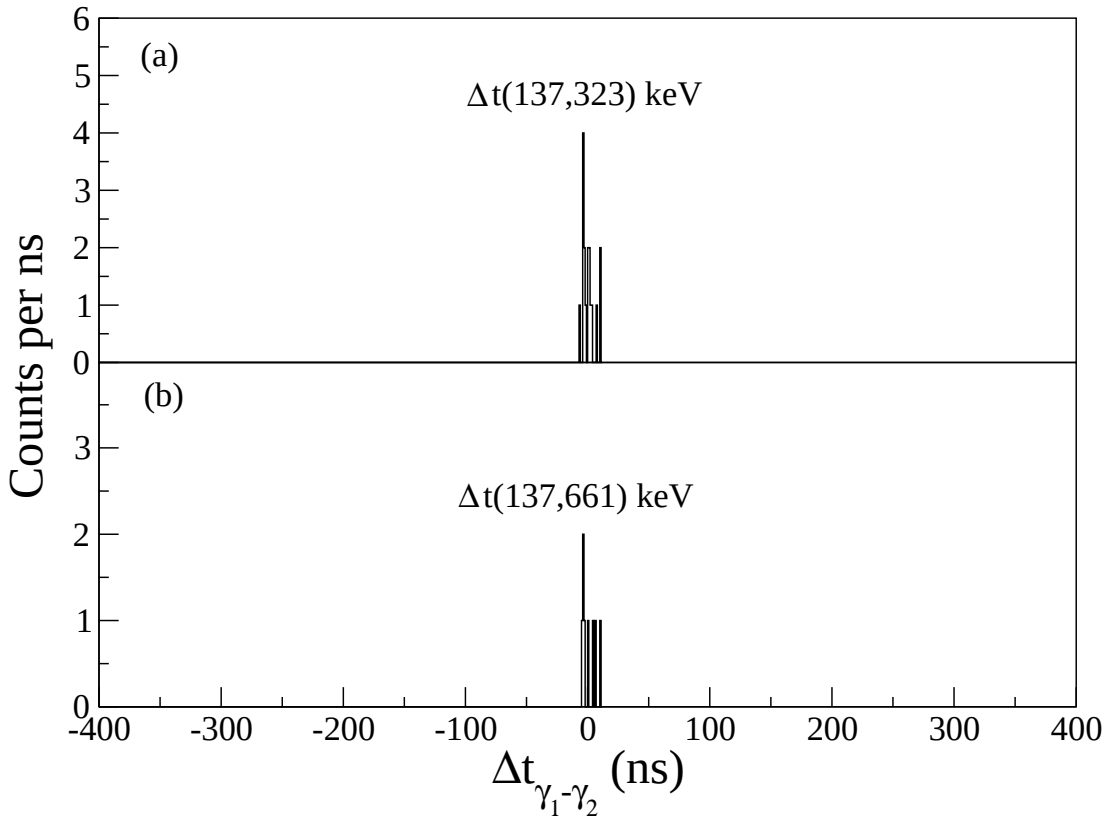

Figure 5.14: γ-ray time difference spectra for dated on ^{209}Tl. γ-rays showing the prompt coincidence nature of the cascade observed in ^{209}Tl.

these orbitals are of particular interest since the ground state decay half-life of ^{208}Hg, and indeed other nuclei in this region, are determined largely by the first forbidden (parity chaning) $\nu g_{9/2} \rightarrow \pi h_{11/2}$ and $\nu i_{11/2} \rightarrow \pi h_{11/2}$ β-decay transitions.

Table 5.4: $B(E2)$ and internal conversion coefficient (α) values ^{208}Hg and ^{209}Tl for different energies. $B(E2)$ values are given in Weisskopf units.

^{208}Hg			^{209}Tl		
Energy keV	α^a	$B(E2)$	Energy keV	α^a	$B(E2)$
10	97540	8.00(1.14)	10	106200	7.61(88)
20	12500	1.95(39)	20	13530	1.87(22)
30	1676	1.92(27)	30	1817	1.83(22)
40	405.9	1.87(27)	40	440.3	1.79(21)
50	136.2	1.82(26)	50	147.8	1.74(20)
60	56.17	1.76(25)	60	60.97	1.68(20)
70	26.72	1.68(24)	70	29.01	1.60(19)
80	14.12	1.58(22)	80	15.33	1.51(18)
90	8.692	1.36(19)	90	9.309	1.33(15)
100	5.545	1.19(17)	100	5.917	1.17(14)

[a] These values are taken from BrIcc v2.2b website.

Table 5.5: Comparison between experimental and shell-model B(E2) transition strengths. Values are given in Weisskopf units.

Nucleus	Transition	$B(E2)_{exp}$	$B(E2)_{calc}$
^{210}Pb	$8^+ \rightarrow 6^+$	0.64(7) [114, 115]	0.69
^{206}Hg	$10^+ \rightarrow 8^+$	0.99(18) [112, 116]	0.87
^{208}Hg	$8^+ \rightarrow 6^+$	1.95(39)–1.58(22)[a]	1.22
^{209}Tl	$17/2^+ \rightarrow 13/2^+$	1.87(22)–1.51(18)[a]	0.96

[a] Assuming a transition energy between 20–80 keV

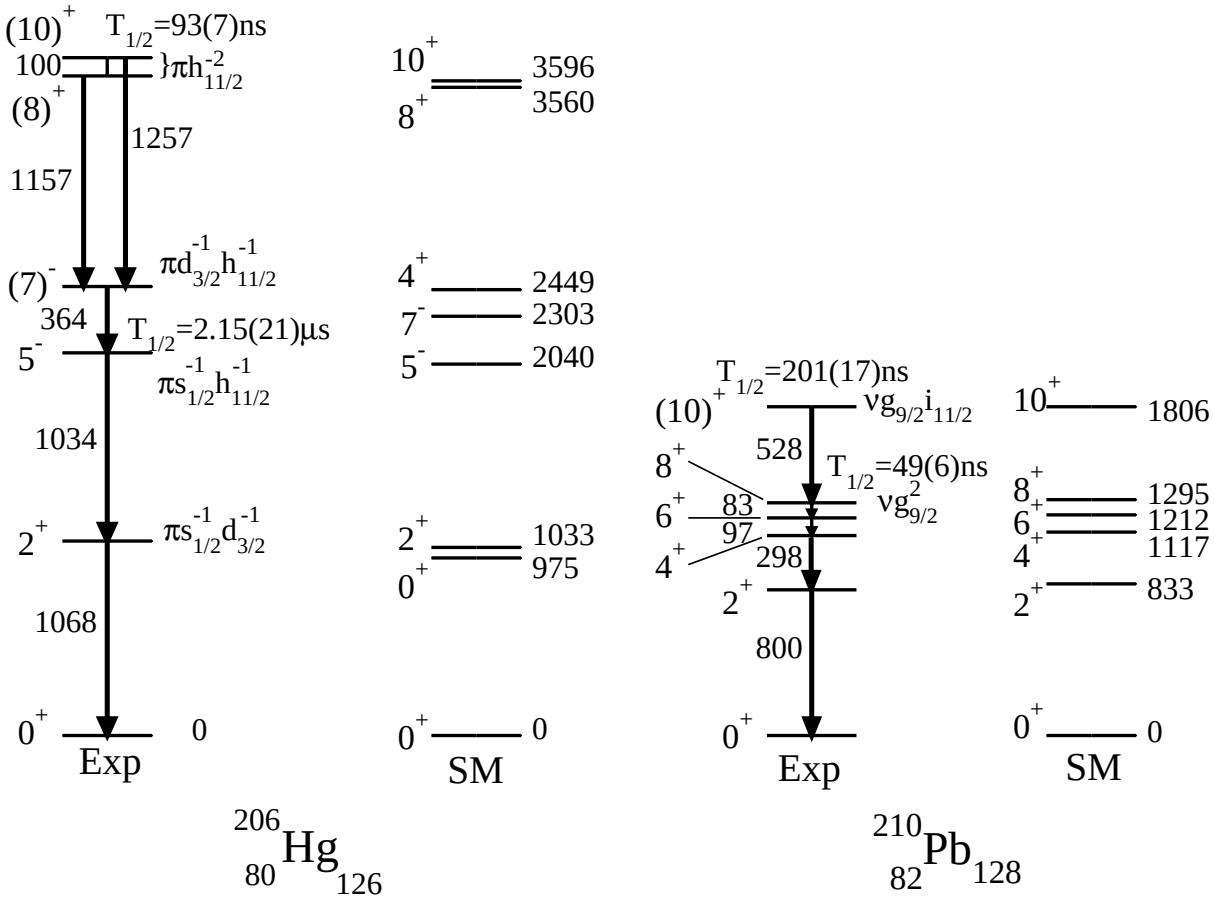

Figure 5.15: Experimental (Exp) and calculated (SM) partial level schemes of ^{206}Hg and ^{210}Pb. The decay schemes are from [112, 115].

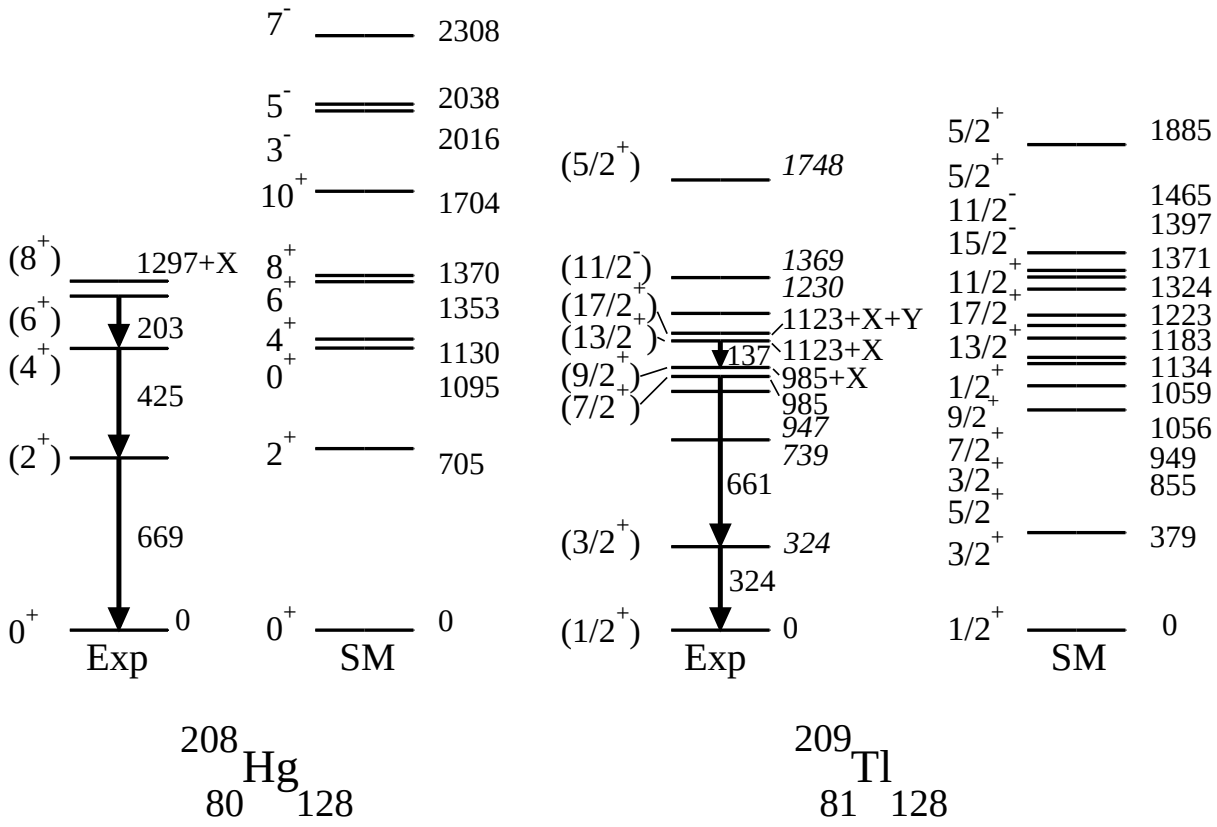

Figure 5.16: Experimental (Exp) and calculated (SM) partial level schemes of the $N = 128$, ^{208}Hg and ^{209}Tl nuclei, deduced from the current work Ref. [43].

Chapter 6

Summary and Future work

6.1 March 2007 experiment

A number of discrete, β-delayed γ-ray transitions associated with β decays from ^{194}Re to excited states in ^{194}Os have been observed, including previously reported decays from the yrast $I^{\pi} = (6^{+})$ state in this nucleus. Three previously unreported γ-ray transitions with energies 194, 349 and 554 keV are also identified. At least three separate β-decaying states, together with their decay half-lives have been established for ^{194}Re for the first time in this work. In addition, previously unreported isomeric states in ^{187}Hf, ^{189,190}Ta and ^{191}W are identified. Nilsson Multi Quasi Particle calculations for prolate and oblate (axially symmetric) deformations predict a variety of possible low-lying candidates states in ^{194}Re which would be expected to β decay to excited states in ^{194}Os. Specifically, both prolate (high-spin) and oblate (low-spin) configurations are predicted for ^{194}Re with spin/parities consistent with the expected decays which are observed to populate discrete levels in the ^{194}Os daughter nucleus.

6.2 April 2008 experiment

Metastable states in the N=128 isotones, ^{208}Hg and ^{209}Tl have been identified. The data provides the first comprehensive experimental test of shell-model calculations and residual interaction for the model space Z<82, N>126. The present results and those of reference [32] for the first measurement of the empirical p-n interaction strength in ^{208}Hg, represent the first beginnings of nuclear structure studies in this

entire, heretofore unknown, major shell quadrant to the southeast of ^{208}Pb.

6.3 Future work

Future directions for this work include the studies of more neutron-rich species of the isotopes studied here. To this end, there have been recent experiments at GSI using a ^{238}U beam to populate more neutron-rich Re and Os isotopes. The structure of these systems should be investigated to see if the predicted change from prolate to oblate shapes is completed for higher neutron numbers. Additional potential studies in this region also include the measurement of B(E2) values for the low-lying excited states in these nuclei to establish transition quadrupole values which would allow a comparison of the evolution of deformation as the N=126 shell closure is approached. Decays from seniority isomers for N>126 systems are also expected in Z<80 isotopes and would provide additional input to the question of proton-hole/neutron-particle residual interactions in nuclei about the ^{208}Pb double shell closure. Such studies are anticipated using the next generation of projectile fragmentation experimental facility at the Facility for Anti-proton and Ion Research (FAIR) in the coming decade.

Appendix A

The magnetic force on a particle with charge q moving with velocity v is given in equation below, where B is the field strength.

$$\overrightarrow{F} = q(\overrightarrow{v} \times \overrightarrow{B}) \tag{A.1}$$

The force on a particle in a circular motion is given by the following equation:

$$F = \frac{mv^2}{r} \tag{A.2}$$

where $r = \rho$ is the magnetic bending radius (which can be measured directly); v is the velocity, $v = c\beta$; p is the momentum (which can be written in terms of the fragment mass (m) and the velocity). By equal these equations A1 and A2

$$\frac{mv^2}{r} = qvB \tag{A.3}$$

Re-arranged eq. A.3 and substituting $r = \rho$

$$B\rho = \frac{1}{q}mv \tag{A.4}$$

For the relativistic mass and velocity, the relativistic parameter γ is includes, where $\gamma = \sqrt{1/(1-\beta^2)}$);

Then,

$$B\rho = \frac{1}{q}\gamma m v \tag{A.5}$$

where $v = c\beta$

$$B\rho = \frac{1}{q}\gamma m c \beta \tag{A.6}$$

where $q = Qe$

$$B\rho = \frac{1}{Q}\gamma c \beta m \frac{1}{e} \tag{A.7}$$

for the mass is rewritten in terms of the atomic number $m = Au$

$$B\rho = \frac{A}{Q}\beta\gamma\frac{uc}{e} \tag{A.8}$$

Appendix B

Calibration

B.1 Energy calibration of the RISING Germaniums array

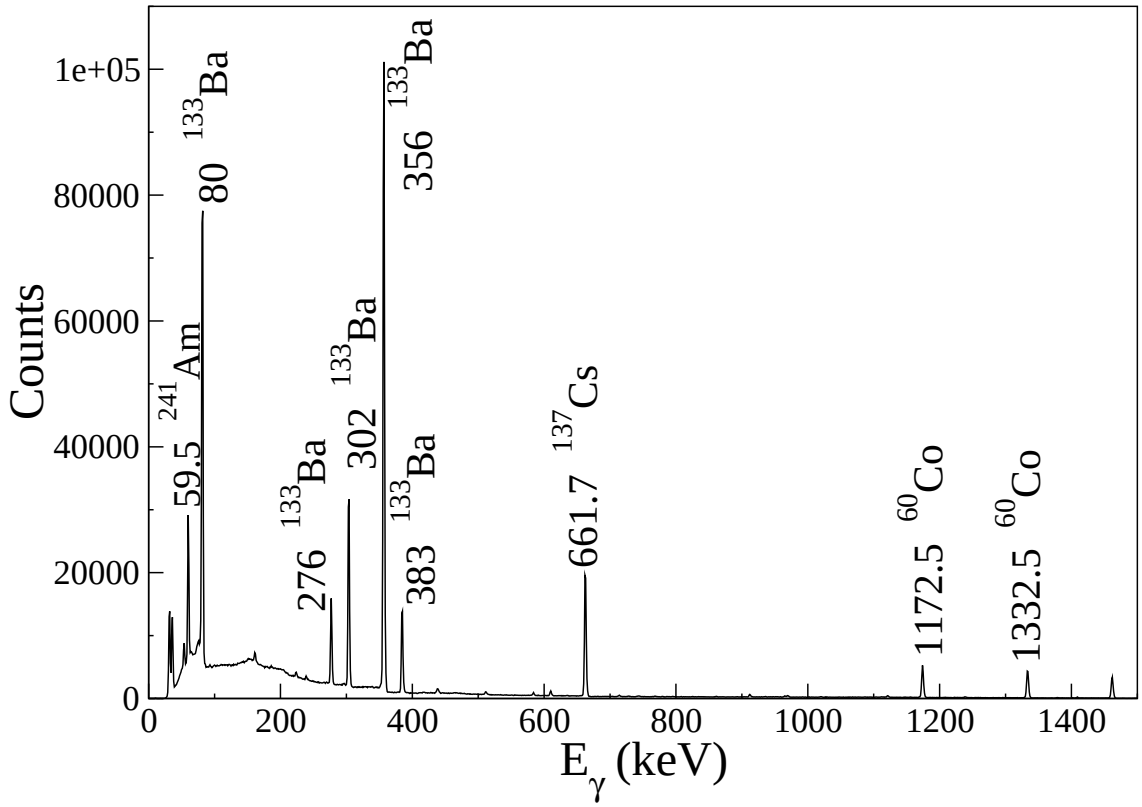

Figure B.1: Energy calibration spectrum of the RISING germanium crystals using two sources: (i) A mixed source of ^{241}Am, ^{137}Cs and ^{60}Co; and (ii) a ^{133}Ba source.

B.2 Energy calibration of the Silicon detectors

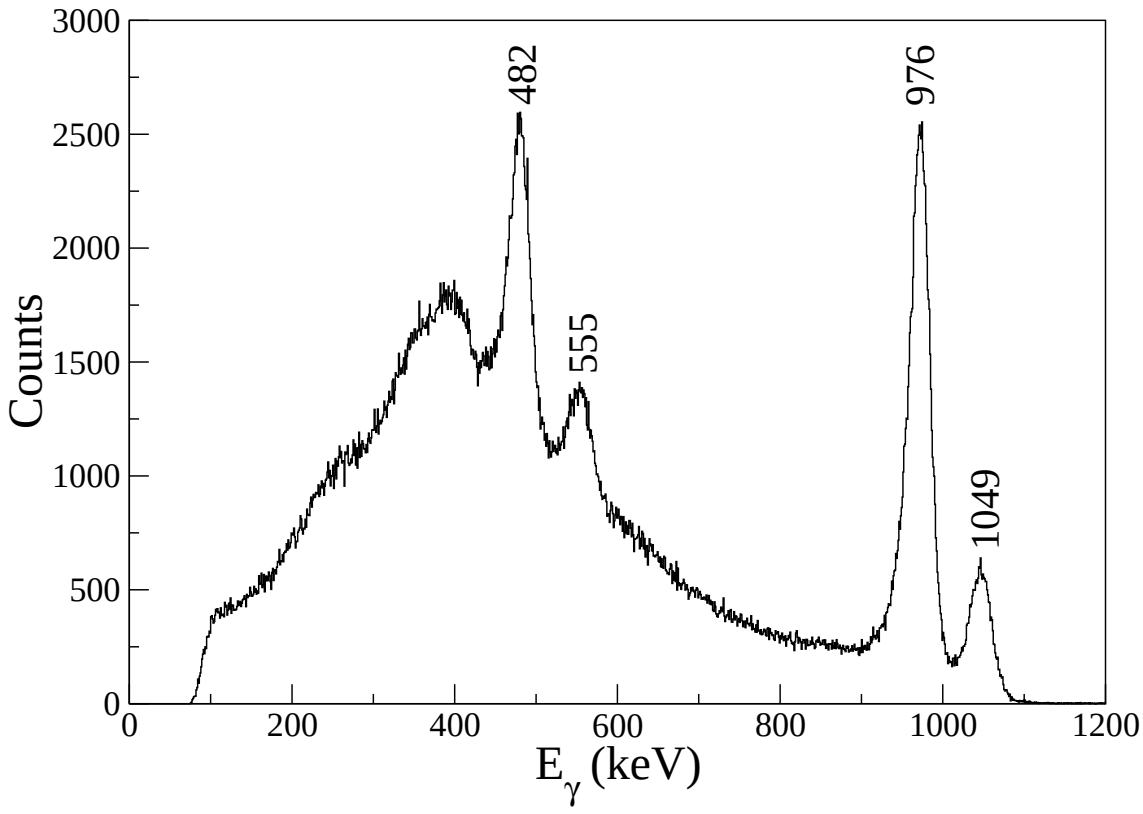

Figure B.2: Energy calibration spectrum of the of the Silicon detectors using the conversion electron of ^{207}Bi source which was used for energy calibration of the linear preamplier part of the silicon active stopper.

Appendix C

Publications

C.1 Peer-Reviewed Publications

N. Al-Dahan, Zs. Podolyák, P.H. Regan *et al.* [+53 others],
Nuclear structure "southeast"of ^{208}Pb: Isomeric states in ^{208}Hg and ^{209}Tl
Phys. Rev. C **80**, 061302(R) (2009).

N. Al-Dahan, Zs. Podolyák, P.H. Regan *et al.* [+51 others],
Isomeric States in ^{208}Hg and ^{209}Tl Populated in Fragmentation of ^{238}U
Acta Phys.Pol. B **40**, 871 (2009).

P.H. Regan, N. Alkhomashi, N. Al-Dahan *et al.* [+39 others],
First results with the rising active stopper
Int. J. Mod. Phys. E **17**, 8 (2008).

P.H. Regan, N. Alkhomashi, N. Al-Dahan *et al.* [+40 others],
New Insights into the Structure of Exotic Nuclei Using the RISING Active Stopper
AIP Conf. Proc. **1090**, 122 (2009).

A.M.D. Bacelar, A.M. Bruce, Zs. Podolyák, S. Lalkovski, S. Pietri, N. Al-Dahan *et al.* [+46 others],

Angular Momentum Population in Fragmentation Reactions

Acta Phys.Pol. B **40**, 889 (2009).

N. Al-Dahan, Zs. Podolyák, P.H. Regan *et al.* [+47 others],

Structure of N $\geqslant$ 126 nuclei produced in fragmentation of ^{238}U

AIP Conf. Proc. **1090**, 145 (2009).

A.Y. Deo, Zs. Podolyák, P.M. Walker, A. Algora, B. Rubio, J. Agramunt, L. M. Fraile, N. Al-Dahan *et al.* [+9 others],

Structures of ^{201}Po and ^{205}Rn from EC/β^+-decay studies

Phys. Rev. C **81**, 024322 (2010).

Appendix D

Oral and Poster Presentations

D.1 Poster Presentations

Institute Of Physics (IOP) Annual Nuclear Physics Conference 2008,

Beta-delayed spectroscopy of ^{194}Re $\rightarrow$ ^{194}Os

University of Liverpool, 1-3 of April 2008, Liverpool, UK

D.2 Oral Presentations

XIII. International Symposium on Capture Gamma-Ray Spectroscopy and Related Topics (CGS),

Structure of N$\geq$126 nuclei produced in fragmentation of ^{238}U

University of Cologne, 25-29 of August 2008, Cologne, Germany

XLIII. Zakopane Conference on Nuclear Physics,

Structure of N$\geq$126 nuclei produced in fragmentation of ^{238}U

1-7 of September 2008, Zakopane, Poland

Institute Of Physics (IOP) Annual Nuclear Physics Conference 2009,

New isomer in N=128 isotones produced in fragmentation of ^{238}U

University of Birmingham, 6-8 of April 2009, Birmingham, UK

XV UK STFC Nuclear Physics Summer School,

Isomeric states in ^{208}Hg and ^{209}Tl produced in fragmentation of ^{238}U

University of Leicester, 12-23 of September 2009, Leicester, UK

Institute Of Physics (IOP) Annual Nuclear Physics Conference 2010,

β-decay from ^{194}Re $\rightarrow$ ^{194}Os: Shape Evolution in Neutron-Rich Osmium Isotopes

University of Edinburgh, 19-21 of April 2010, Edinburgh, UK

Bibliography

[1] P. H. Regan and B. Blank, Physics World 29 (2000).

[2] G. Audi, A. H. Wapstrab, and C. Thibaulta, Nucl. Phys. A **729**, 337 (2003).

[3] `http://www.nndc.bnl.gov/ensdf/`
Evaluated Nuclear Structure Data File (ENSDF), online database,
National Nuclear Data Center,
(Site Visited: April, 2010).

[4] H. Geissel, G. Müzenberg, and K. Riisager, Annu. Rev. Nucl. Part. Sci. **45**, 163 (1995).

[5] J. Benlliure *et al.*, Nucl. Phys. A **87**, 660 (1999).

[6] K. Krumbholz *et al.*, Z. Phys. **11**, 350 (1995).

[7] M. Caamaňo *et al.*, Eur. Phys. J. A **23**, 201 (2005).

[8] Zs. Podolyák *et al.*, Phys. Rev. C **79**, 031305(R) (2009).

[9] M. Pfützner *et al.*, Phys. Lett. B **444**, 32 (1998).

[10] Zs. Podolyák *et al.*, Euro. Phys. J. Special Topics **150**, 165 (2007).

[11] P. D. Stevenson *et al.*, Phys. Rev. C **72**, 047303 (2005).

[12] P. Sarriguren, R. Rodriguez-Guzmán, and L. M. Robledo, Phys. Rev. C **77**, 064322 (2008).

[13] K. H. Maier *et al.*, Phys. Rev. C **30**, 1702 (1984).

[14] S. J. Steer *et al.*, Phys. Rev. C **78**, 061302(R) (2008).

[15] J. S. Lilley, *Nuclear Physics Principles and Applications* (John Wiley and Sons, New York, 2001).

[16] S. W. Yates *et al.*, Nucl. Phys. **A222**, 301 (1974).

[17] R. D. Bagnel *et al.*, Phys. Lett. **66B**, 129 (1977).

[18] F. T. Baker *et al.*, Nucl. Phys. **A258**, 43 (1976).

[19] C. Y. Wu *et al.*, Nucl. Phys. **A607**, 178 (1996).

[20] C. Wheldon *et al.*, Phys. Rev. C **59**, 2334(R) (1999).

[21] E. R. Flynn and D. G. Burke, Phys. Rev. C **17**, 501 (1978).

[22] L. M. Robledo, R. Rodríguez-Guzmán, and P. Sarriguren, J. Phys. G: Nucl. and Part. Phys. **36**, 115104 (2009).

[23] `http://www.nndc.bnl.gov/chart/`
Online database, National Nuclear Data Center,
(Site Visited: March, 2010).

[24] A. Bohr and B. R. Mottelson, Kgl. Danske Videnskab. Selskab. Mat.-fys. Medd. **27**, 16 (1953).

[25] R. F. Casten, *Nuclear Structure from a Simple Perspective* (Oxford Science Publications, Oxford New York, 2000).

[26] K. S. Krane, *Introductory Nuclear Physics* (John Wiley and Sons, New York, 1988).

[27] S. Raman, C. W. Nestor, JR., and P. Tikkanen, Atom. Data and Nucl. Data Tables **78**, 1 (2001).

[28] G. Sharff-Goldhaber and J. Weneser, Phys. Rev. **98**, 212 (1955).

[29] G. Sharff-Goldhaber and J. Weneser, Mat. Fys. Medd. K. Dan. Vidensk. Selsk. **26**, 14 (1952).

[30] D. S. Brenner, R. B. Cakirli, and R. F. Casten, Phys. Rev. C **73**, 034315 (2006).

[31] R. B. Cakirli and R. F. Casten, Phys. Rev. Lett. **96**, 132501 (2006).

[32] L. Chen *et al.*, Phys. Rev. Lett. **102**, 122503 (2009).

[33] M. J. Martin, Nucl. Data Sheets **108**, 1583 (2007).

[34] C. Ellegaard, P. D. Barnes, and E. R. Flynn, Nucl. Phys. **A259**, 435 (1976).

[35] H. Xiaolong and W. Baosong, Nucl. Sci Tech. **18**, 261 (2007).

[36] M. C. Kouassi *et al.*, Nucl. Instr. Meth. A **280**, 424 (1989).

[37] M. J. Martin, Nucl. Data Sheets **63**, 723 (1991).

[38] H. Geissel *et al.*, Nucl. Instr. Meth. B **70**, 286 (1992).

[39] R. Kumar *et al.*, Nucl. Inst. Meth. A **598**, 754 (2009).

[40] N. Al-Dahan *et al.*, Acta Physica Polonica B **40**, 871 (2009).

[41] N. Al-Dahan *et al.*, AIP conference proceedings **1090**, 145 (2009).

[42] P. H. Regan *et al.*, AIP conference proceedings **1090**, 122 (2009).

[43] N. Al-Dahan *et al.*, Phys. Rev. C **80**, 061302(R) (2009).

[44] J. J. Valiente-Dobón, Ph.D. thesis, University of Surrey, 2007.

[45] A. H. Wapstra and K. Bos, Atomic Data and Nuclear Data Tables **19**, 215 (1977).

[46] R. D. Woods and D. S. Saxon, Phys. Rev. **95**, 577 (1954).

[47] C. Wheldon, Ph.D. thesis, University of Surrey, 1999.

[48] B. A. Brown, *Lecture Notes in Nuclear Structure Physics* (Michigan State University, USA, 2005).

[49] J. M. Eisenberg and W. Greiner, *Nuclear Models Volume I* (North-Holland, Amsterdam, 1987).

[50] W. Greiner, *Nuclear Models* (Springer-Verlag Berlin Heidelberg, New York, 1996).

[51] G. Jones, Ph.D. thesis, University of Surrey, 2006.

[52] S. G. Nilsson, Dan. Mat. Fys. Medd. **29**, 3 (1955).

[53] A. Garnsworthy, Ph.D. thesis, University of Surrey, 2007.

[54] B. Singh *et al.*, Nucl. Data Sheets **97**, 241 (2002).

[55] J. M. Blatt and V. F. Wiesskopf, *Theoretical Nuclear Physics* (John Wiley and Sons, New York, 1952).

[56] `http://\-wwwrsphysse.anu.edu.au/nuclear/bricc/`.

[57] A. Messiah, *Quantum Mechanics* (North-Holland, Amsterdam, 1970).

[58] T. K. Nieto, Ph.D. thesis, Universidade De Santiago De Compostela, 2007.

[59] J. J. Gaimard and K. H. Schmidt, Nucl. Phys. A **531**, 709 (1991).

[60] J. Hüfner *et al.*, Phys. Rev. C **12**, 1888 (1975).

[61] M. De Jong *et al.*, Nucl. Phys. A **613**, 435 (1997).

[62] P. Walker and G. Dracoulis, Nature **399**, 35 (1999).

[63] D. Horn *et al.*, Phys. Rev. Lett. 7 (1977).

[64] Y. Yamazaki *et al.*, Phys. Lett. **44B**, 440 (1973).

[65] J. J. Ressler *et al.*, Phys. Rev. **69**, 034317 (2004).

[66] H. C. Britt, Atomic data and Nucl. Data Tables **12**, 407 (1973).

[67] `http://www-aix.gsi.de/~wolle/EB\_at\_GSI` /FRS-WORKING/ACCELERATOR/IMAGES/accel_overview.gif.

[68] B. Voss *et al.*, Nucl. Instr. Meth. A **364**, 150 (1995).

[69] M. Pfützner *et al.*, Nucl. Instr. Meth. B **86**, 213 (1994).

[70] H. Stelzer, Nucl. Instr. Meth. A **310**, 103 (1991).

[71] P. H. Regan *et al.*, Int. J. of Mod. Phys. E. **17**, 8 (2008).

[72] http://www-linux.gsi.de/weick/frs/mwpc.html.

[73] G. Münzenberg, Nucl. Instr. Meth. **B70**, 265 (1992).

[74] G. F. Knoll, *Radiation Detection and Measurement* (John Wiley and Sons, New York, 2000).

[75] M. Górska *et al.*, Acta Phys. Pol. B **38**, 1219 (2007).

[76] P. J. Nolan, F. A. Beck, and D. B. Fossan, Annu. Rev. Nucl. Part. Sci. **45**, 561 (1994).

[77] S. Pietri *et al.*, Acta Phys. Pol. B **38**, 1255 (2007).

[78] S. Pietri *et al.*, Nucl. Instr. Meth. B **261**, 1079 (2007).

[79] The RISING collaboration, Photographs of the detector array, http://www-linux.gsi.de/wolle/EB at GSI/GE DETECTOR/index.html.

[80] P. H. Regan *et al.*, Nucl. Phys. A **787**, 491 (2007).

[81] Zs. Podolyák *et al.*, Phys. Lett. B **672**, 116 (2009).

[82] S. J. Steer *et al.*, Acta Phys. Pol. B **38**, 1283 (2007).

[83] M. V. Ricciardi *et al.*, Phys. Rev. C **73**, 014607 (2006).

[84] C. Scheidenberger *et al.*, Nucl. Instr. Meth. B **142**, 441 (1998).

[85] S. Pietri *et al.*, Nucl. Inst. Meth. B **261**, 1079 (2007).

[86] N. Alkhomashi, Ph.D. thesis, University of Surrey, 2010.

[87] N. Alkhomashi *et al.*, Phys. Rev. C **80**, 064308 (2009).

[88] S. J. Steer *et al.*, Int. J. of Mod. Phys. E **18**, 1002 (2009).

[89] Zs. Podolyák *et al.*, Phys. Lett. B **491**, 225 (2000).

[90] Zs. Podolyák *et al.*, Nucl. Phys. A **722**, 273 (2003).

[91] G. F. Farrelly *et al.*, Acta Phys. Polo. B **40**, 885 (2009).

[92] C. M. Baglin, Nucl. Data Sheets **84**, 717 (1998).

[93] R. F. Casten *et al.*, Phys. Lett. B **76**, 280 (1978).

[94] C. Wheldon *et al.*, Phys. Rev. C **63**, 011304(R) (2000).

[95] G. D. Dracoulis *et al.*, Private Communication (2010).

[96] G. D. Dracoulis, Private Communication (2010).

[97] P. Möller *et al.*, Atomic data and Nucl. Data Tables **59**, 185 (1995).

[98] W. Nazarewicz, M. A. Riley, and J. D. Garrett, Nucl. Phys. A **512**, 61 (1990).

[99] E. B. Suckling and P. D. Stevenson, Private Communication (2009).

[100] N. V. Zamfir and R. F. Casten, Phys. Rev. Lett. **75**, 1280 (1995).

[101] G. Scharff-Goldhaber and J. Weneser, Phys. Rev. **98**, 212 (1955).

[102] R. F. Casten, Phys. Rev. Lett. **54**, 1991 (1985).

[103] R. F. Casten, Phys. Lett. B **152**, 145 (1985).

[104] R. F. Casten and N. V. Zamfir, Phys. Rev. Lett. **70**, 402 (1993).

[105] R. B. Cakirli and R. F. Casten, Phys. Rev. C **78**, 041301(R) (2008).

[106] W. Nazarewicz, G. A. Leander, and J. Dudek, Nucl. Phys. **A467**, 437 (1985).

[107] R. Wyss *et al.*, Phys. Lett. B **215**, 211 (1988).

[108] W. Nazarewicz, R. Wyss, and A. Johnson, Nucl. Phys. **A503**, 285 (1989).

[109] R. Fossion, D. Bonatsos, and G. D. Lalazissis, Phys. Rev. C **73**, 044310 (2006).

[110] Zs. Podolyák *et al.*, Eur. Phys. J. A **42**, 489 (2009).

[111] S. J. Steer, Ph.D. thesis, University of Surrey, 2008.

[112] B. Fornal *et al.*, Phys. Rev. Lett. **87**, 212501 (2001).

[113] A. Langenberg and J van Eck, J. Phys. B: Atom. Molec. Phys. **12**, 1331 (1979).

[114] E. Browne, Nucl. Data Sheets **99**, 649 (2003).

[115] D. J. Decman *et al.*, Phys. Rev. C **28**, 1060 (1983).

[116] F. G. Kondev, Nucl. Data Sheets **109**, 1527 (2008).

[117] W. Baldridge, N. Freed, and J. Gibbons, Phys. Lett. B **36**, 179 (1971).

[118] B. A. Brown *et al.*, MSU-NSCL report 1289 (2004).

[119] E. K. Warburton, Phys. Rev. C **44**, 233 (1991).

[120] T. T. S. Kuo and G.H. Herling, U.S. Naval Research Laboratory Report No. 2258 **unpublished**, (1971).

[121] A. Hosaka, K.-I. Kubo, and H. Toki, Nucl. Phys. A **244**, 7 (1985).

[122] R. B. Firestone and V. S. Shirley, *Table of Isotopes, Eighth edition, Volume II* (John Wiley and Sons, New York, 1996).